

Thesis Proposal

Robust and Natural Gait via Neuromuscular Control for Transfemoral Prostheses

Nitish Thatte

December 17, 2016

The Robotics Institute
Carnegie Mellon University
Pittsburgh, PA 15213

Thesis Committee:
Hartmut Geyer (Chair)
Steven Collins
Chris Atkson
Elliot Rouse, Northwestern University

*Submitted in partial fulfillment of the requirements
for the degree of Doctor of Philosophy*

Copyright ©2016 Nitish Thatte.

Abstract

the abstract

Contents

1	<i>Introduction</i>	17
1.1	<i>Motivation</i>	17
1.1.1	<i>Challenges in Transfemoral Prosthesis Control</i>	19
1.1.2	<i>Approach</i>	21
1.2	<i>Expected Contributions</i>	23
2	<i>Background</i>	25
2.1	<i>Fundamental Walking Dynamics and Control</i>	25
2.1.1	<i>Centralized Control</i>	26
2.1.2	<i>Decentralized Controllers</i>	29
2.1.3	<i>Dynamic Prosthesis Control</i>	31
2.1.4	<i>Walking Control Summary</i>	33
2.2	<i>Bioinspired Control</i>	33
2.2.1	<i>Central Pattern Generators</i>	34
2.2.2	<i>Neuromuscular Reflexes</i>	36
2.2.3	<i>Conclusion</i>	40
2.3	<i>Prosthesis Design</i>	40
2.3.1	<i>Rigid Transmission Transfemoral Prostheses</i>	41
2.3.2	<i>Design of Dynamic Prostheses</i>	44
2.4	<i>Stumble Recovery for Prostheses</i>	46
2.4.1	<i>Responses to Trips</i>	47
2.4.2	<i>Trip Detection and Classification</i>	48
2.5	<i>Background Summary</i>	49

3	<i>Neuromuscular Model</i>	51
3.1	<i>Mechanical Model</i>	51
3.2	<i>Hill Muscle Models</i>	53
3.3	<i>Stance Reflexes</i>	55
3.4	<i>Swing Leg Control</i>	57
3.4.1	<i>Idealized Swing Leg Control</i>	57
3.4.2	<i>Neuromuscular Reflex Swing Leg Control</i>	59
4	<i>Completed Work</i>	61
4.1	<i>Transfemoral Prosthesis Design</i>	61
4.1.1	<i>Knee Joint</i>	62
4.1.2	<i>Ankle Joint</i>	64
4.1.3	<i>Experiments on Powered Knee/Passive Ankle Prosthesis</i>	66
4.1.4	<i>Slow Walking Behavior</i>	67
4.1.5	<i>Response to Swing Leg Tripping</i>	69
4.2	<i>Comparison of Robustness Achieved by Reflex and Impedance Controls in Simulation</i>	70
4.2.1	<i>Simulation Environment</i>	70
4.2.2	<i>Controller Optimization for Natural and Robust Walking</i>	71
4.2.3	<i>Results</i>	72
4.2.4	<i>Discussion</i>	74
4.3	<i>Optimization of Systems Using Preferences</i>	76
4.3.1	<i>Introduction</i>	76
4.3.2	<i>Preliminaries</i>	78
4.3.3	<i>Methods</i>	80
4.3.4	<i>Results</i>	83
4.3.5	<i>Discussion and Conclusion</i>	87
5	<i>Proposed Work</i>	91
5.1	<i>Evaluation of Neuromuscular Transfemoral Prosthesis Control</i>	91
5.2	<i>Optimizing Prosthesis Control using Preferences</i>	91
5.3	<i>Learning Trip Recovery Policies</i>	91
5.4	<i>Proposed Work Summary and Timeline</i>	91

Bibliography 93

List of Figures

- 1.1 Examples of microprocessor-controlled mechanically-passive knee prostheses (a,b) and a energy storage and return ankle-foot prosthesis (c). 17
- 1.2 Vanderbilt University's Robotic Transfemoral Prostheses. 18
- 1.3 Biom Robotic Ankle Prosthesis 19
- 1.4 A passive dynamic walker walks down hill with no internal actuation highlighting the role of natural dynamics in walking. 19
- 1.5 Honda's Asimo Robot uses position control and statically stable gaits. 20
- 1.6 Eilenberg et al. [2010] simulate virtual muscles in order to control an ankle prosthesis. 21
- 1.7 Push Bot robot for training and evaluating trip recovery policies 22
- 1.8 Proposed SEA prosthesis design 23

- 2.1 The bipedal spring mass model captures many fundamental features of human walking such as the M-shaped vertical ground reaction profile, S-shaped horizontal ground reaction profile and sinusoidal center of mass trajectory. Figure adapted from Geyer et al. [2006]. 26
- 2.2 Finite state machine used for the quasi-stiffness control proposed by Sup et al. [2007]. In each state the control employs impedance functions that determine the behavior of the ankle and knee joints of an active transfemoral prosthesis. 31
- 2.3 Central Pattern Generator for bipedal locomotion as described in Taga et al. [1991]. Six neural oscillators receive feedback from and command joint torques for the hips, knees, and ankles of a planar biped model. A one dimensional high-level control signal enables control of speed and elicits gait transitions. 34
- 2.4 Neuromuscular models with reflex feedbacks. The model developed by Ogihara and Yamazaki [2001] activates individual muscles according to the activity of a CPG and proprioceptive reflexes that can involve the muscle itself, other muscles, and ground contact sensing. Geyer and Herr [2010] does away with the CPG and achieves locomotion with only reflex feedbacks. 37

- 2.5 Neuromuscular model used by Eilenberg et al. [2010] to control an active ankle prosthesis. During stance, a virtual muscle driven by positive force feedback, generates plantarflexion torque. During swing, a virtual spring damper provides dorsiflexion torque to prevent toe scuffing. 38
- 2.6 Vanderbilt University's Robotic Transfemoral Prostheses. 41
- 2.7 Torque vs angle relationship for the ankle during level ground walking. A linear spring relationship captures a significant portion of ankle function during stance. Data from Winter [2009] scaled to 85 kg subject. 42
- 2.8 Series elastic actuation inserts a spring between the gear output and the load (here drawn as linear actuator for simplicity). Torque is measured via the spring deflection, $\tau = k(\theta_l - \theta_m - \theta_0)$ where τ is the output joint torque, k is the spring constant, and θ_l and θ_m are the load and motor positions and θ_0 is the spring's rest length. 44
- 2.9 Torque vs angle relationship for the knee during level ground walking. Knee displays more complicated functionality than the ankle (see fig. 2.7), with two distinct springs need to explain early stance and pre-swing/swing behavior. Data from Winter [2009] scaled to 85 kg subject. 46
- 3.1 The skeletal model we use to simulate neuromuscular reflex control. The model consists of seven segments: left and right feet, shanks, and thighs, as well as a lumped head-arms-trunk (HAT) segment. Flexion joint angles are positive, extension joint angles are negative, and the zero angle configuration represents standing. 51
- 3.2 Hill-type muscle tendon unit with contractile element (CE), parallel elasticity (PE), and series elasticity (SE). 53
- 3.3 Force-length relationship of the CE. 53
- 3.4 Force-velocity relationship of the CE. 53
- 3.5 PE and SE force length relationship. For the PE, $l_{\text{ref}} = l_{\text{opt}}$ and $\epsilon_{\text{ref}} = \epsilon_{\text{PE}}$. Likewise, for the SE, $l_{\text{ref}} = l_{\text{slack}}$ and $\epsilon_{\text{ref}} = \epsilon_{\text{SE}}$. 54
- 3.6 Biped walking model with labeled muscles. 54
- 3.7 The swing leg control guides the leg towards a desired landing leg angle α_{tgt} through three phases: (i) Flex the knee until it achieves a clearance leg length l_{clr} . (ii) Hold the leg length via knee damping. (iii) Stop and Extend the leg towards the ground when the leg reaches α_{tgt} . Figure reproduced from Desai and Geyer [2012]. 58
- 3.8 Neuromuscular Swing leg control employs the seven muscles used in the stance control as well as a monoarticular knee flexor, the biceps femoris short head, and a biarticular hip flexor/knee extensor, the rectus femoris 59

- 4.1 Render of proposed powered knee and ankle prosthesis design. The prosthesis includes series elastic actuators to enable accurate torque control and a unidirectional parallel ankle spring to offset the required angle torque. 61
- 4.2 Knee motor torque required for running 62
- 4.3 Internal and external design of the knee joint. 63
- 4.4 Impact simulation we used to determine appropriate series spring stiffness. 63
- 4.5 Ankle torque vs angle curve during steady, level-ground walking (blue) (Winter [2009] scaled to 80 kg person). A unidirectional parallel spring can provide a portion of this torque (green) and reduces the required actuator torque (purple) to lie under repeated torque limit of the Harmonic Drive Gear set (orange). 64
- 4.6 Ankle motor torque required to take the trip recovery action observed by Pijnappels et al. [2005] (blue, trajectory obtained by scaling walking data from Winter [2009] to a peak torque of 202 N · m, 75% gear efficiency assumed). Using a parallel spring allows the motor to produce the required torque (green) while remaining within its torque limit (purple). 64
- 4.7 Ankle motor torque required to reproduce the running trajectory recorded by Novacheck [1998] assuming a parallel spring stiffness of 267 N·m/rad and a gear efficiency of 75%. 65
- 4.8 Internal and external design of the ankle joint. 65
- 4.9 Impact simulation we used to determine appropriate series spring stiffness. 66
- 4.10 A non-amputee experimenter tests the prosthesis using an iWalk Crutch as a knee adaptor. The experimenter wears a lift shoe on the contralateral leg to compensate for the added thigh length of the prosthesis and knee adaptor. 66
- 4.11 Prosthesis behavior at walking speed of 0.5 m/s. Shown are the hip and knee trajectories, the knee controller torque, and the activations of the vastus, hamstring, and gastrocnemius muscles generated by the prosthesis control in the testbed. Solid black lines show averaged data of ten trials with the individual trials depicted in gray. Dashed lines show corresponding data from human walking at preferred speed (joint angles and knee torque: Winter [2009], muscle surface electromyograms: Perry and Burnfield [2010]). Solid and dashed vertical lines indicate median toe off times for the prosthesis and human data respectively. 68

- 4.12 Response to simulated tripping disturbance. (A) Undisturbed ankle trajectory calculated from hip and knee angles assuming constant hip height. (B-D) Ankle trajectories with disturbance applied in early, mid and late swing (arrows). The vertical dashed line shows the target landing position of the foot, which corresponds to a 75 degree landing angle. 69
- 4.13 Control performance of simulated prosthesis on rough terrain. The distances walked over terrains with different ground roughness are compared between the amputee model using a powered knee-ankle prosthesis with impedance control (green) and hybrid neuromuscular control (blue) as well as with the unimpaired human model (red). Shown are the median and range (25th and 75th percentiles) of the covered distances for 50 terrains sampled at each roughness level. 73
- 4.14 Tripping response of the amputee model with neuromuscular (A) and impedance control (B) of the prosthesis. Shown are the prosthetic toe trajectories during undisturbed gait (dashed line) and when disturbed by a 15 N · s impulse (solid line). The neuromuscular controller effectively responds to the disturbance and maintains a qualitatively similar toe trajectory. The impedance controller leads to foot scuffing and an eventual fall. 74
- 4.15 Learning from preferences. (a) Mean and standard deviation of $P(f_t|D_n)$ (blue) after two preferences queries (orange) from the true objective function (purple). (b) Mean of $P(f_t|D_n)$ (blue) and means of $P(f_t|D_n, x_m^*)$ (green) for two samples of x_m^* . PES-P queries a new comparison (orange) for which the preference is currently uncertain, but on average is certain after conditioning on all x_m^* . 80
- 4.16 Performance of predictive entropy search with preferences (PES-P), expected improvement (EI), and Latin hypercube random sampling (LH) for optimizing random objective functions sampled from a GP (a-d), and tuning feedback control parameters of random linear systems (e-f) and a biped walking model (g-h). Shown are the median and interquartile range over 20 trials of the immediate regret (IR) against the number of preference queries. Black stars indicate iterations for which PES-P achieves statistically significant stochastic reductions in IR compared to both EI and LH according to one-sided Mann-Whitney U tests ($p < 0.05$). 83

4.17 Optimization of prosthesis control with user preferences. (a) Median and interquartile range of user scores achieved by PES-P, EI and LH after 50 iterations (total of 42 scores per algorithm: seven users times six scorings). (b) Median and interquartile range of convergence achieved by the three algorithms as measured by the Euclidean distance between the current and final estimates of the optimum. PES-P and LH achieve the same median score of 4 across all users but PES-P converges faster and more consistently. EI converges fastest but to a lower median score of 3. 85

List of Tables

- 2.1 Required knee and ankle torque, velocity, and power for walking (1.40 m/s average speed, scaled to 85 kg subject, data from Winter [2009]) 40
- 2.2 Estimated reflected inertia at knee and ankle joints of Generation 3 Vanderbilt Prosthesis [Lawson et al., 2014]. Motor data taken from Maxon Motors Catalog[Motor, 2016b,a] Knee reflected inertia compared to inertia of human shank and foot about knee. Ankle inertia compared to human foot about its center of mass. Human inertias estimated from Winter [2009] for an 85 kg, 1.7 m tall person. 43
- 3.1 Segment lengths (l_s), center of mass (d_{COM}) and joint (d_{Joint}) locations measured from the distal end, masses (m), and inertias (J) approximated from Günther and Ruder [2003]. 51
- 3.2 Joint limits for the hip, knee, and ankle joints listed in degrees. Positive joint angles represent flexion and negative joint angles represent extension (see fig. 3.1). 52
- 3.3 Neuromuscular parameters for shared entities (left) and the hamstring muscle (right) 54
- 4.1 Designed and achieved design specifications. (*Maximum total ankle torque is 290 N · m achieved at 10 degrees of dorsiflexion.) 62

1

Introduction

1.1 Motivation

SIX HUNDRED THOUSAND lower-limb amputees currently live in the United States according to recent estimates [Ziegler-Graham et al., 2008]. People undergo amputations due to a variety of reasons including traumatic injuries from workplace accidents, traffic collisions, and as casualties of war. In addition, a large percentage (54%) suffer from the loss of a limb due to complications arising from dysvascular disease associated with diabetes. Consequently, largely due to the expected increase in diabetes in the coming years, Ziegler-Graham et al. [2008] estimate that by 2050 the number of amputees living in the United States will likely double.

Currently, prosthetists often prescribe transfemoral amputees (those with amputations between the hip and knee joints) an energy storage and return composite foot such as the Sierra Foot (Freedom Innovations; Irvine, CA; fig. 1.1c) along with a microprocessor-controlled, mechanically-passive knee prosthesis. These knee prostheses feature control algorithms that measure kinematic and force data via sensors embedded in the device and adjust the knee's resistance accordingly. Examples of microprocessor-controlled prosthetic knees include the C-Leg (Otto Bock; Duderstadt, Germany; fig. 1.1a), which has an adjustable hydraulic damping system, and the Rheo Knee (Össur; Reykjavik, Iceland; fig. 1.1b), which achieves variable damping via a magnetorheological fluid. While Johansson et al. [2005] show these microprocessor-controlled knees can improve amputee gait characteristics by decreasing metabolic energy consumption and peak hip torque and increasing gait smoothness over that provided by fully-passive knee prosthesis, these prostheses still cannot fully replicate healthy leg behavior as they are incapable of providing positive power during the gait cycle.

Positive power at the knee is evident in a number of locomotion



(a) C-Leg™ Knee ©Ottobock



(b) Rheo™ Knee ©Össur



(c) Thrive™ Foot ©Freedom Innovations

Figure 1.1: Examples of microprocessor-controlled mechanically-passive knee prostheses (a,b) and a energy storage and return ankle-foot prosthesis (c).

tasks including level walking [Perry and Burnfield, 2010], walking up stairs [Nadeau et al., 2003], running [Buczek and Cavanagh, 1990], and jumping [Hubley and Wells, 1983]. In addition, active knee flexion and extension muscle activations have been noted during stumble recovery [Eng et al., 1994]. At the ankle joint, passive spring-like prostheses cannot replicate the positive net work seen in the ankle joint during level ground walking, which is essential for push-off and forward propulsion [Perry and Burnfield, 2010].

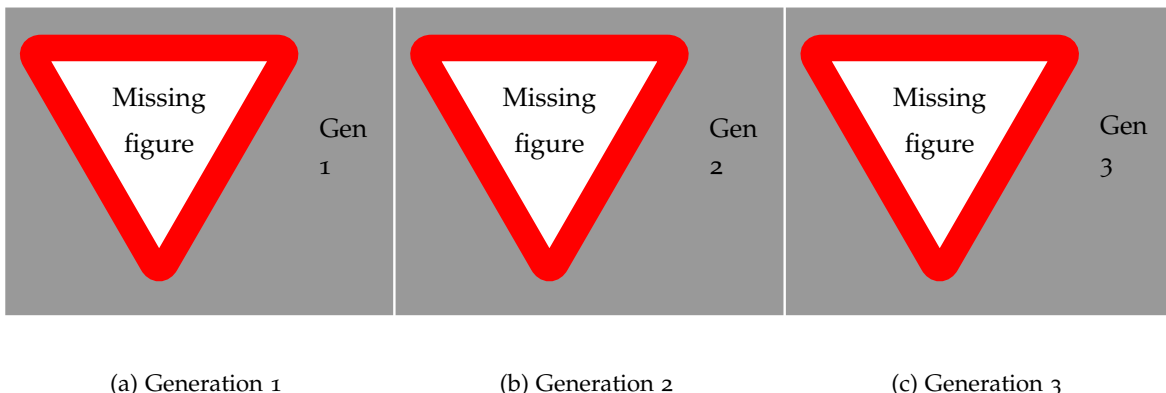
Consequently, lower-limb amputees, and especially transfemoral amputees¹ equipped with mechanically-passive prostheses suffer from a number of issues including markedly increased energy consumption [Waters et al., 1976], abnormal gait kinematics [Jaegers et al., 1995], and an increased likelihood of falling [Miller et al., 2001]. Specifically, large percentages of transfemoral amputees report they are unable to complete tasks such as walking outside in inclement weather (47.4%), walking while carrying a load (42.7%), walking up or down stairs without a handrail (38.5%, 37.9%), walking outside on uneven terrain (29.5%), picking up an object from the ground (28.1%) or getting up from the floor after a fall (22.8%) [Gauthier-Gagnon et al., 1999].

Importantly, these gait pathologies can lead to an avoidance of walking [Gauthier-Gagnon et al., 1999]. This is especially true in the case of falls. Miller et al. [2001] find 49.2% of lower limb amputees feared falling and that of those afraid of falls 76% avoided physical activity as a result. Avoidance of physical activity is eminently concerning as it may lead to reduced strength, endurance, and balance, feeding a positive feedback loop that causes further debilitation.

To help remedy this situation, in the past decade academic research groups and companies have developed robotic powered knee and ankle prostheses for lower-limb amputees. These prostheses feature actuators at the knee and/or ankle that, if controlled correctly,

¹ those with above the knee amputations

Figure 1.2: Vanderbilt University's Robotic Transfemoral Prostheses.



could potentially restore the kinetics, kinematics, and reactions of the healthy human leg. Notable examples include three generations of transfemoral prostheses developed by Vanderbilt University (fig. 1.2) [Sup et al., 2009, Lawson et al., 2013, 2014] and the Biom powered ankle (fig. 1.3) [Herr and Grabowski, 2011]. These powered prostheses have helped amputees walk on level ground more naturally and efficiently, as well as walk up stairs and slopes [Sup et al., 2011, Lawson et al., 2013], run [Huff et al., 2012, Shultz et al., 2015], perform sit-to-stand [Varol et al., 2009], and dance [Rouse et al., 2015]. These results illustrate the benefits of powered prostheses as many of these tasks require positive joint power and thus would be difficult to perform with mechanically-passive prostheses.

1.1.1 Challenges in Transfemoral Prosthesis Control

It still remains an open research question how best to control these prostheses to achieve natural and robust gaits. In the most established control method for powered prostheses, the prosthesis uses simple functions to approximate the joint torque versus angle relationship, termed the *quasi-stiffness* observed during walking [Sup et al., 2007, Lenzi et al., 2014b]. However, since the torque functions only approximate steady, level walking, this method requires further tuning to handle other situations such as walking on slopes [Sup et al., 2011] or rough ground [Thatte and Geyer, 2016] and changing foot placement targets [Schepelmann, 2016].

As mentioned earlier, walking on slopes and rough ground present major hurdles for transfemoral amputees. Moreover, previously developed prosthesis controls have not specifically addressed the risk of falling that is so detrimental to amputee quality of life. Therefore, it is clear that we should formulate a prosthesis controller with more power to generalize to a larger variety of environments, which will improve amputee gait robustness. Formulating a robotic prosthesis controller to accomplish this goal requires we address three main challenges:

Challenge 1: Human locomotion is a dynamic task During stance, the leg acts in a compliant, spring-like manner [Geyer et al., 2006] and significant time is spent in statically-unstable contact on the heel or toe, suggesting the importance of mechanical stability achieved via foot placement [Perry and Burnfield, 2010]. During swing, ballistic motion explains much of the leg trajectory [Mochon and McMahon, 1980]. Indeed, much of the entire gait cycle can be explained via passive dynamics as evidenced by passive-dynamic walkers (fig. 1.4) that can stably walk down slight inclines with no onboard power source [McGeer, 1990, Collins et al., 2005].

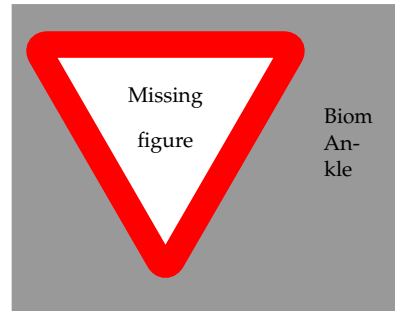


Figure 1.3: Biom Robotic Ankle Prosthesis

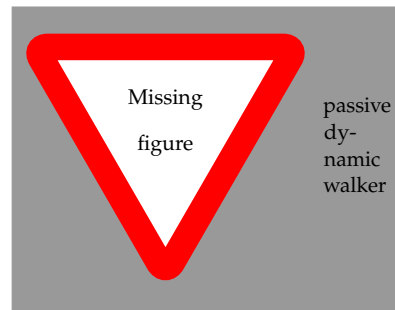


Figure 1.4: A passive dynamic walker walks down hill with no internal actuation highlighting the role of natural dynamics in walking.

Consequently, in order to ensure that amputee gaits are natural and efficient, but still robust, it is essential that robotic prosthesis controllers not only admit, but leverage the inherent dynamics of walking. Therefore, the required control paradigm cannot follow strategies often used for humanoid locomotion (for example on Honda's Asimo Robot fig. 1.5) that employ position control in order to track preplanned, statically-stable gaits. Rather, the control strategy should interact dynamically with the amputee by governing interaction forces instead of mandating kinematic objectives.

Challenge 2: We have incomplete state information An additional difference between robotic prosthesis control and controls often used on humanoid walking robots stems from the lack of full state information. Humanoid walking controllers such as those used in the DARPA robotics challenge (DRC), use the full state of the robot (*i.e.* the positions and velocities of every joint and the robot's center of mass), to plan and track a trajectories, thereby ensuring stability of the full system [Feng et al., 2015, Kuindersma et al., 2014, Englsberger et al., 2014].

While these recent approaches used in the DRC are dynamic and therefore address challenge 1, for prosthesis control we typically only know the state of the prosthesis itself. It is unreasonable to expect that amputees will don full body sensing suits in order to provide a complete picture of the state of the amputee-prosthesis system. Therefore, prosthesis controllers must be decentralized, meaning prosthesis joint torque commands are computed using only a subset of the full state, while the human controls their own joints with a different subset of state. A side effect of decentralization is a loss of formal stability guarantees of the combined amputee and prosthesis system. However, we can still evaluate amputee stability empirically.

Challenge 3: Amputees are unique Finally, we should be able to adapt robotic prosthesis controllers to each amputee's individual needs. The variation in amputee needs arise from a number of factors including, but not limited to, the amputee's height, weight, strength, endurance, reason for amputation, time since amputation, experience, and personal preferences. Consequently, prostheses and controllers should be optimized to suit individual users.

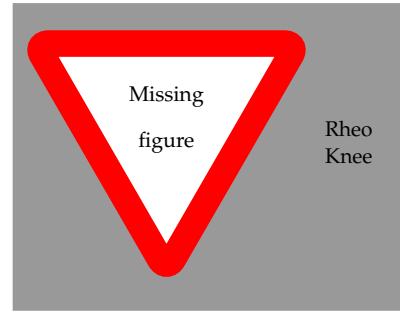


Figure 1.5: Honda's Asimo Robot uses position control and statically stable gaits.

This thesis proposes dynamic decentralized control methods for transfemoral prostheses, along with methods to optimize them for individual amputees, in order to improve gait robustness and naturalness.

1.1.2 Approach

In this thesis, we seek to improve amputee gait robustness and naturalness by employing an alternative approach to joint control in prostheses that seeks to mimic the underlying dynamics and control of the human neuromuscular system. In this approach, instead of replicating recorded torque profiles with quasi-stiffness functions, we model the dynamical system, consisting of virtual muscles and local reflex feedback pathways, that generate joint torques during locomotion. Crucially, the resulting prosthesis control addresses challenges 1 and 2: the control is decentralized, as the reflex feedback are designed to rely only on the state of other muscles in the same leg, and dynamic, as the virtual muscles integrate the sensed kinematic state of the prosthesis in order to generate desired torques, not positions, at the joints. These torques, along with the reaction forces in the amputee's socket and on the ground shape the motion of the amputee-prosthesis system.

Prior work on neuromuscular models shows that when applied to simulated biped models they can produce robust gaits with natural appearances. For example, using a neuromuscular model, an optimized simulated biped model walked on unseen, uneven terrain with sudden drops and steps up to 14 centimeters [Song and Geyer, 2015]. In addition, Eilenberg et al. [2010] successfully applied the neuromuscular control approach to a powered ankle prosthesis (fig. 1.6), which mimics the kinematics and kinetics of the ankle joint in human walking including its adaptation to sloped environments. It remains unclear, however, whether we can extend the approach to transfemoral prostheses with both knee and ankle joints.

Therefore, to motivate our specific choice of neuromuscular control for improving amputee gait stability, in completed work, we construct a simulation of the amputee-prosthesis system and compare the gait robustness achieved by neuromuscular control versus the established impedance control method. We find that neuromuscular control enabled the simulated amputee to walk further over rougher terrain than the established impedance control method allows.

Next, to test the feasibility of the control approach to control a real system, we design and build a partial powered transfemoral prosthesis prototype with an active knee actuator and a passive, spring-loaded ankle. The prosthesis prototype uses series elastic actuation [Pratt and Williamson, 1995] that allows it to accurately achieve the torques commanded by the neuromuscular model. Initial tests with an intact user wearing the prosthesis through an amputee simulator adaptor show that the proposed neuromuscular control, when applied to the knee of an active prosthesis, produce reasonable

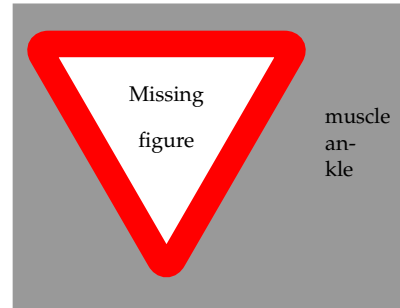


Figure 1.6: Eilenberg et al. [2010] simulate virtual muscles in order to control an ankle prosthesis.

kinematics and joint torques. This positive result motivates continued development of the prosthesis into a full active knee and ankle transfemoral prosthesis and implementation of testing of the full neuromuscular prosthesis control.

To address the challenge 3, we propose to optimize prosthesis controls for specific subjects. To this end, in completed work, we develop an algorithm that uses preference feedback from users to optimize control system parameters. We test the method on problems of increasing relevance: first by optimizing synthetic reward functions, then optimizing the parameters of simulated dynamical systems, and finally by optimizing neuromuscular control parameters for intact users wearing the prosthesis through an amputee emulator brace. The results suggest the proposed optimization method outperforms baseline methods for optimizing from user preferences. However, it remains to be seen if the proposed method improves gait characteristics when applied to the full neuromuscular controlled prosthesis for an amputee subject. We intend to investigate this question via additional tests on an amputee subject.

Last, we seek to improve the capability of the transfemoral prosthesis to respond to trips, which pose a significant and impactful threat to amputee quality of life. To accomplish this goal, we propose to use imitation learning techniques [Argall et al., 2009] to learn policies that allow the prosthesis to appropriately respond to disturbances during swing. The proposed method to learn these policies will address challenges 1-3 in that it will be a decentralized control that only uses information from the prosthesis and be dynamic and personalized by working with each amputee' innate trip response reflexes.

Previous work in this area has trained classifiers on data obtained by tripping healthy human subjects [Lawson et al., 2010, Shirota et al., 2014]. The authors then evaluate these classifiers via cross validation, in which a subset of the training data is set aside and used for testing, and report low error-rates. However, to date no one has applied a trip classifier to prosthesis hardware in order to initiate a trip recovery controller. Trivial application of classifiers trained on healthy human subject data likely will yield poor results, as the distribution of data at test time generated by a prosthesis that is controlled by a learned policy will differ from the data used to train that policy. The training and test time distribution mismatch violates the i.i.d.² assumption that underpins classification performance. To remedy this problem, we intend to employ the DAGGER training method [Ross et al., 2011] that aligns the train and test time distributions through an iterative procedure. We will collect training and testing data to learn and evaluate the trip recovery policies using the Push Bot robot (fig. 1.7) which can apply tripping forces to subjects via actuated tethers.

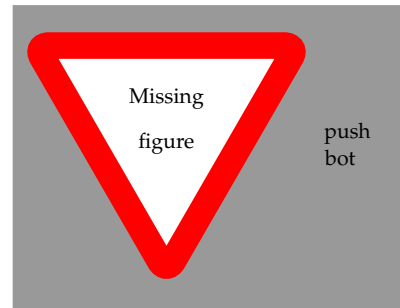


Figure 1.7: Push Bot robot for training and evaluating trip recovery policies

² independent and identically drawn

1.2 Expected Contributions

Work presented in this thesis will advance the state of the art for robotic transfemoral prosthesis control and optimization. There are four main expected contributions:

Contribution 1: A series elastic prosthesis design We present the design of a transfemoral prosthesis featuring series elastic actuators (SEAs) capable of accurately producing the torques commanded by the neuromuscular model, generating enough torque and speed to enable trip recovery experiments, and handling the impact loads expected during trip recovery experiments. We have made significant progress towards this contribution already by completing the design, manufacturing, assembly, and initial testing of the prosthesis' knee joint as well as the design and fabrication of its ankle joint. Figure 1.8 shows the current stage of the prosthesis prototype with the completed SEA knee and a passive spring-loaded ankle well as a CAD render of the expected completed prosthesis design.

Contribution 2: A method for optimizing systems via preferences We present a new algorithm for optimizing systems, such as prostheses, using user preferences. The algorithm uses preferences between pairs of control parameters to circumvent having to define or learn an explicit reward function for each user. Additionally, the algorithm employs Bayesian optimization techniques in order to query users for preferences that are expected to maximally reduce the uncertainty of the location of the optimum parameters.

Contribution 3: Evaluation of neuromuscular transfemoral prosthesis control We will implement the proposed neuromuscular prosthesis control on the SEA transfemoral prosthesis, optimize its parameters according to the amputee subject's preferences, and evaluate the prosthesis' ability to produce a natural and robust gait. We will measure gait characteristics in terms of joint kinematics and kinetics and the amputee's metabolic energy consumption. We will present results relative to typical non-amputee gait, the amputee's gait using his or her prescribed prosthesis, and the gait achieved by an unoptimized prosthesis control. We will also evaluate the ability the control to adapt to novel circumstances such as changes in gait speed and ground slope.

Contribution 4: Learning and evaluation of trip recovery policies The last contribution is a method to learn and evaluation of trip response policies for recovering from disturbances during swing. The learned policies will advance the state-of-the-art as they will be the first trip recovery policies implemented on real prosthesis

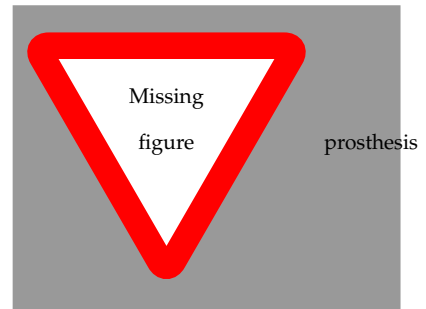


Figure 1.8: Proposed SEA prosthesis design

hardware, whereas previous policies were trained and tested offline using data collected from non-amputee subjects.

2

Background

THE MAIN GOAL OF THIS THESIS is to improve transfemoral amputee gait robustness and naturalness by applying neuromuscular models of human locomotion to control prosthesis hardware capable of dynamic locomotion. Existing approaches to walking control in humanoid robots and prostheses have largely failed to reach the levels of stability and dynamism required to match that of an amputee's lost limb. In this chapter, we will review these existing approaches, examine their strengths and weaknesses, and motivate our specific control and design choices.

Section 2.1 categorizes approaches to walking control into four major groups based on their ability to produce dynamic interactions with the environment (dynamic vs kinematic) and whether they can produce control commands using only a subset of state (decentralized vs centralized). As mentioned earlier, only dynamic, decentralized controls address challenges 1 and 2 of amputee locomotion (section 1.1.1) and are thus suitable for prosthesis control. Section 2.2 dives deeper into a subset of dynamic decentralized control: bioinspired approaches that seek to model the function of the lost limb and are thus particularly well suited for prosthesis control. Section 2.3 reviews existing mechanical designs of active prostheses and examines their ability to enable dynamic locomotion. Finally, section 2.4 will discuss previous work towards empowering prostheses with active trip recovery modes via explicit detection and classification of stumbles.

2.1 Fundamental Walking Dynamics and Control

Simple point-mass models of walking can help us understand the fundamental dynamics that control must shape in order to achieve stable locomotion gaits. The simplest model that reproduces the center of mass trajectory and ground reaction forces seen during

human walking is the bipedal spring mass model [Geyer et al., 2006]. This model, illustrated in fig. 2.1, simplifies locomotion to a pair of compliant unidirectional springs connected to a point mass. When initialized with human-like mass and leg length, the model can generate characteristic features of human locomotion such as sinusoidal center of mass trajectories, M-shaped vertical ground reaction forces, S-shaped horizontal ground reaction forces, and the proper sequence of double and single support.

We will look at two paradigms for walking control: centralized approaches that use full state information and decentralized approaches that use a subset of state information. Centralized approaches typically utilize a model of the full system in order to compute control commands that project the full system's dynamics onto those of the simplified model. Usually, centralized approaches also place additional constraints on the center of mass (COM) dynamics in order to facilitate planning and ensure stability. In contrast, decentralized approaches typically do not explicitly model either the full system or the fundamental dynamics. Rather, these approaches use heuristics to generate motions and forces similar to those of the fundamental model.

2.1.1 Centralized Control

Kinematic centralized control is one of the oldest forms of locomotion control. The predominant approach in this category is based on the linear inverted pendulum model (LIPM) [Kajita and Tani, 1991, Kajita et al., 2001]. This simplified locomotion model applies additional reductions to the bipedal spring-mass model, replacing spring legs with ideal prismatic force sources and constraining the center of mass to move on a plane. The resulting simplified model features linear COM dynamics with respect to the zero moment point (ZMP). The ZMP is the point on the ground about which the horizontal moments needed to counteract the total reaction forces on the system is zero. When the ZMP lies within the support polygon¹ (SP), it is coincident with the center of pressure (COP). On the other hand, if the ZMP moves beyond the SP, the system will begin to tip over the edge of the SP. In one dimension, the location of the ZMP is given by,

$$x_{ZMP} = x_{COM} - \frac{z_{COM}\ddot{x}_{COM}}{g}. \quad (2.1)$$

This equation relates the horizontal COM, x_{COM} , dynamics to the location of the ZMP, x_{ZMP} , given the height of the COM, z_{COM} , and gravitational acceleration g .

Based on this insight, researchers have developed numerous ZMP-trajectory methods that follow 5 basic steps:

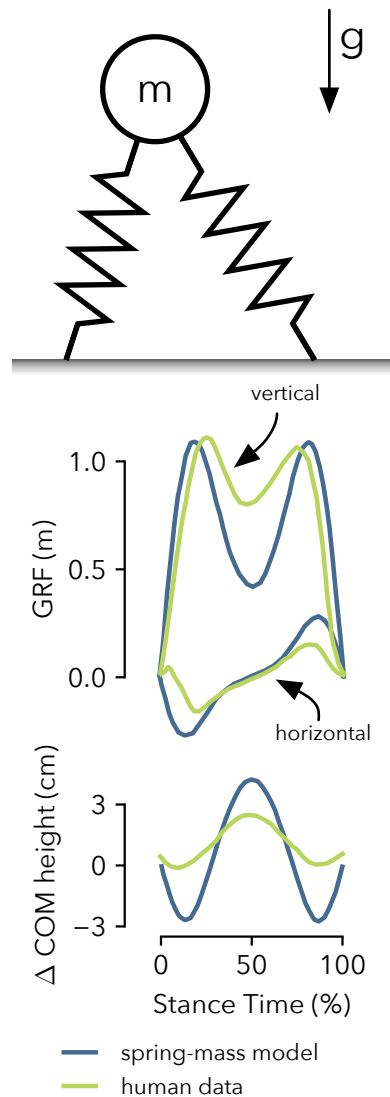


Figure 2.1: The bipedal spring mass model captures many fundamental features of human walking such as the M-shaped vertical ground reaction profile, S-shaped horizontal ground reaction profile and sinusoidal center of mass trajectory. Figure adapted from Geyer et al. [2006].

¹ The convex hull of contact points on the ground

1. Plan a series of foot steps given the terrain and task such that the induced sequence of support polygons contains no gaps.
2. Generate a ZMP trajectory that lies within the support polygons. Typically, it is desirable that the trajectory maintains its distance from the edges of the support polygons in order to provide a margin of stability.
3. Solve for the COM trajectory given the desired ZMP trajectory. This step requires inverting the solution to a differential equation, eq. (2.1), to solve for x_{COM} . Researchers have proposed numerous solutions to this problem including preview control [Kajita et al., 2003], and differential dynamic programming [Feng et al., 2015], the latter of which can solve for the ZMP and COM trajectories simultaneously.
4. Use inverse kinematics to calculate joint velocities that track the COM trajectory.
5. Track the desired joint velocities with servo controls.

A large number of robots have successfully employed this general framework to walk [Hirai et al., 1998], traverse uneven ground [Shimmyo et al., 2010], and run [Kajita et al., 2007]. Moreover, the method guarantees that for the nominal gait, the COP will remain in the SP, and thus the system will maintain its stability.

However, there are several key issues to this approach. One issue stems from steps 4 and 5 listed above. These steps generate and precisely follow via servo control a kinematic trajectory of joint angles. When perturbed by unforeseen external forces, stiff position control in this manner may generate large reaction forces and thus may move the COP outside of the SP, resulting in a fall. We can understand the interactions between the leg and the environment and the leg and robot body through the concepts of impedance and admittance. The environment and robot body are admittances, objects that take forces as inputs and move (or not move) in response. As discussed in Hogan [1985], it is therefore necessary that the leg acts like an impedance, an object that produces an interaction force in response to the position imposed on it by the environment and robot body.

Dynamic centralized control seeks to control these interaction forces by directly computing joint torques, instead of using high-gain position control. Commonly, in this approach the dynamics model of the full system²,

$$M(q)\ddot{q} + C(q, \dot{q})\dot{q} + N(q) = S\tau + J^T(q)\lambda, \quad (2.2)$$

² Where q , \dot{q} , and \ddot{q} describe the generalized coordinates, velocities, and accelerations of the system configuration, $M(q)$ is the mass matrix, $C(q, \dot{q})$ is a matrix of centripetal and Coriolis force coefficients, $N(q)$ represents the gravitational forces, S is a selection matrix that assigns joint torques τ to coordinates q , $J(q)$ is the Jacobian between joint angles and contact points, and λ is a vector of external forces

is used as an equality constraint in a *quadratic program* (QP) that minimizes torques, reaction forces, and deviation from the desired trajectory. Additionally, the QP can include inequality constraints representing torque saturations and friction limits [Hutter et al., 2013, Herzog et al., 2014, Saab et al., 2013, Wensing and Orin, 2013]. Recently, at the DARPA Robotics Challenge (DRC) several robots used QP-based dynamic centralized approaches to control humanoid robots through a disaster relief scenario [Feng et al., 2015, Kuindersma et al., 2014, Englsberger et al., 2014].

While replacing steps 4 and 5 with a QP-based torque control can help improve dynamism and compliance, the resulting biped gaits of these strategies do not resemble human gaits for two reasons: First, the linear inverted pendulum model does not produce center of mass trajectories or ground reaction force profiles similar to those seen during human locomotion. Second, human gaits do not constrain the ZMP to the support polygon as we spend significant time on the heel and balls of our feet during stance [Perry and Burnfield, 2010].

To overcome these issues and produce more human like gaits, recently researchers have investigated applying dynamic centralized control approaches to enforce spring-mass model dynamics instead of LIPM dynamics. With this approach, researchers have developed robust controllers for both walking [Liu et al., 2016] and running [Martin et al., 2015] for humanoid robots. Alternatively, Sreenath et al. [2011] replaced the LIPM model with a one-degree-of-freedom walking mechanical linkage. In this control, all joint angles are parameterized with respect to a single phase variable, usually the leg angle. As the phase variable progresses via its passive dynamics a control Lyapunov function impose virtual constraints that force joints to follow a walking gait trajectory. The control expresses a degree of dynamism, as the phase variable is free to evolve naturally, and demonstrates human-like reflexes as it is automatically maintains its balance in response to external perturbations by stepping forward or backwards.

While centralized control approaches have helped close the gap in dynamism and reactivity displayed by humans and robotic systems, these methods can also suffer from their reliance on an accurate model of the system dynamics (eq. (2.2)). It may be difficult to identify the parameters of this model, such as friction and damping coefficients and inertias, especially for prosthesis systems. Consequently, researchers have explored decentralized control methods that use only a subset of the state and generally rely on heuristic control strategies instead of deriving control actions from a detailed system model.

2.1.2 Decentralized Controllers

In contrast to the centralized control methods discussed in the previous section, decentralized methods generate walking gaits without requiring measurement of the full system state. Consequently, decentralized walking strategies typically do not involve planning³ and do not enjoy stability guarantees. Rather, gait emerges naturally from the coupled dynamics of several closed-loop systems. In the case of prosthesis control, one system is the human neuromuscular system and the other is the closed-loop dynamics of the robotic prosthesis.

For example, the earliest robotic prosthesis control strategy, termed *echo control*, records the kinematics of the healthy leg and then executes an identical trajectory on the prosthesis on the following step [Grimes et al., 1977, Grimes, 1979]. This strategy, as with all robotic prosthesis controls we will review, does not require measurement of the torso, head, or arm movement. Also, during execution of the trajectory, the position servo controls only require measurement of the prosthesis joint angles, making it more practical for implementation on a prosthesis device. However, this control is an example of a *kinematic decentralized control*. Consequently, it suffers from many of the same problems identified in centralized kinematic control. Namely, it does not comply to the environment, which can result in large and unnatural reaction forces. For example, if a prosthesis under this control strategy encountered an obstacle during swing, the knee would not flex in response, thereby inducing a large moment on the amputee. Moreover, echo control suffers from the problem of not allowing the amputee to start or stop gait with their prosthesis leg.

As was the case for centralized control, commanding torques instead of joint angles helps alleviate this issue by allowing for compliant interaction with the environment. *Dynamic decentralized control* typically features a finite state machine with states representing different phases of gait such as stance and swing. Within each phase, a heuristic control law specifies the torque command. For example, the first robotic system to achieve stable, dynamic locomotion employed simple heuristics to regulate the height, velocity, and attitude of 2 dimensional one legged hopping robot [Raibert et al., 1983]. Specifically, to control the height of the robot, the control adjusts the duration of thrust generated by the prismatic leg actuator during stance. Researchers empirically determined the relationship mapping thrust duration to hopping apex height. To control horizontal velocity, first it is assumed that placing the foot in the center of the locus of points comprised of the center of gravity projected onto the floor will result in zero change in horizontal velocity. Then, a linear feedback gain on velocity error determines the offset from this point.

³ steps 1 to 3 of the centralized control framework

A servo control on the leg angle during swing realizes the desired foot placement. Finally, the control regulates the torso attitude during stance via PD feedback.

Unlike a centralized control scheme, Raibert et al.'s scheme does not consider the interaction between these control modules, preferring instead to treat stabilization of each degree of freedom as an independent task. Regardless, the system demonstrated remarkable dynamism and robustness, allowing the hopping robot to jump 0.25 m, run 1.2 m/s, and recover from horizontal disturbance forces applied by an experimenter. Moreover, the control strategy easily extended to 3D locomotion as well without an exponential increase in computation complexity. This seminal work demonstrates that LIPM-based, centralized control that carries stability guarantees is not necessary to ensure stability of robotic systems and suggests the constraints and model reductions enforced by centralized control may hold systems back. Rather, intelligent design of heuristic control to shape the natural dynamics of a system can in fact provide high levels of performance in practice.

Virtual model control, proposed by Pratt et al. [2001], provides a convenient method for designing heuristic control strategies. While the authors originally used the method as a centralized control, later work such as Ajallooeian et al. [2013] apply the method to design controls that feature decentralized elements as well. In contrast to the control proposed in Raibert et al. [1983], which commands forces aligned with the robot's actuators, virtual model control does not require such correspondence. Rather, designers can use their intuition to place virtual mechanical elements, such as springs, dampers, masses, and linkages on or between reference coordinate frames located anywhere in space. The virtual mechanisms apply generalized forces F to the coordinate frames, which are translated to joint torques τ via the Jacobian J according to

$$\tau = J^T F. \quad (2.3)$$

Joint-level controls realize these desired torques, thereby simulating the virtual components.

This control approach has many advantages: First, it provides an intuitive framework to design controllers for many tasks and many different robot architectures. Second, one can easily design decentralized controllers with this method by using virtual mechanisms that span only a subset of joints. This creates a sparse Jacobian matrix, J , resulting in a decentralized control approach that can be applied to prostheses. Last, impedance mechanisms such as springs and dampers ensure dynamic interaction with the environment with reasonable reaction forces.

2.1.3 Dynamic Prosthesis Control

With the goal of dynamic interaction with the environment in mind, Sup et al. [2007] formulated *impedance control* for active prostheses. The strategy is essentially a form of simple virtual model control, where linear and nonlinear springs along with linear dampers span individual joints. A finite state machine, such as the one in fig. 2.2, switches impedance functions as the amputee progresses through phases of gait: early and late stance and early and late swing. The impedance functions in this strategy actually describe the *quasi-stiffness* of the joint [Rouse et al., 2013], which is the torque vs angle curve seen during walking. Therefore, we will henceforth, refer to this strategy as quasi-stiffness control for prostheses.

To describe the quasi-stiffness curve, Sup et al. [2008] uses a piecewise model with linear and cubic stiffness terms, and a linear damping term.

$$\tau = -k_1(\theta - \theta_0) - k_2(\theta - \theta_0)^3 - b\dot{\theta}. \quad (2.4)$$

Regression analysis of the torque versus angle and velocity data of intact subjects performing level-ground walking returns the quasi-stiffness parameters for each joint in each state. An experimenter can further tune these parameters to better suit the amputee's gait.

This strategy has been implemented on both transtibial [Shultz et al., 2014] and transfemoral [Lawson et al., 2014] active prostheses and has improved amputee gait characteristics over those provided by passive prostheses. Moreover, by tuning impedance parameters for specific tasks and augmenting the finite state machine, researchers have extended impedance control to help amputees to walk up and down slopes [Sup et al., 2011] and stairs [Lawson et al., 2013], run [Huff et al., 2012, Shultz et al., 2015], and execute sit-to-stand motions [Varol et al., 2009]. Lenzi et al. [2014b] present a similar method, in which a look-up-table directly stores the quasi-stiffness curve with respect to angle and velocity. With this method, Lenzi et al. obtain speed adaptation by linearly interpolating between two look up tables representing slow and fast walking.

In contrast to the kinematic echo control strategy discussed earlier, quasi-stiffness control should produce more reasonable interaction forces. This is especially true when the prosthesis encounters an unexpected disturbance, as the control does not try to follow a specific trajectory with high precision and thus high feedback gains. However, whereas impedance control as originally proposed by Hogan [1985] advocated independent specification of the disturbance response torque and the torque required to achieve the desired motion, the quasi-stiffness control strategies we have discussed use the same behavior for both.

add figure with torque vs angle curves

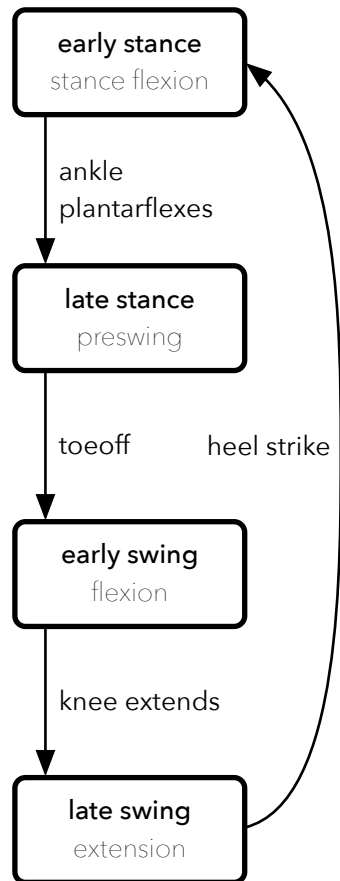


Figure 2.2: Finite state machine used for the quasi-stiffness control proposed by Sup et al. [2007]. In each state the control employs impedance functions that determine the behavior of the ankle and knee joints of an active transfemoral prosthesis.

Recently, several research efforts have investigated dynamic control strategies that provide both a feed forward element that generates the desired motion and a feedback element that responds to disturbances. Such approaches allow one to tune these two aspects separately. While these approaches are decentralized in that they do not require state information of the amputee, they do borrow aspects of centralized approaches such as trajectory planning, and model-based computation of feed-forward torques.

For example, Lenzi et al. [2014b,a] compute minimum jerk trajectories for the knee and ankle joints during the swing phase. These trajectories are parameterized by fifth order polynomials that connect the initial states of the knee and ankle joints to desired final states. The method uses the measured joint angles, velocities and acceleration just before toe-off as the initial state and specifies the desired final state for both joints as zero angle, velocity, and acceleration.

The ankle joint uses a single trajectory, while the knee joint uses two trajectories, one that connects the initial state to a maximum knee flexion state and one that connects the maximum knee flexion state to the final state. Using a model of the system represented by Euler-Lagrange dynamics equations (eq. (2.2)) one can calculate the required feed forward torque to follow the planned trajectories. Minimizing the jerk, the derivative of acceleration, helps ensure smoothness of the computed torques. A proportional derivative feedback control then determines the disturbance response behavior. The use of a strong feed forward term allows for lower PD feedback gains and more compliant behavior.

A disadvantage of the minimum jerk trajectory approach is it generates and executes a trajectory whose duration is heuristically determined at toe-off. Recently, Gregg et al. [2014] and Zhao et al. [2016] have proposed methods similar to the centralized virtual constraint control discussed in section 2.1.1, in which the natural progression of a phase variable determines the rate at which the control follows preplanned trajectories. Gregg et al. [2014] chooses to follow the ankle-foot and knee-ankle-foot rollover shapes, which are defined as the location of the center of pressure with respect to coordinate systems attached to the shank and the ankle-hip line respectively. The center-of-pressure naturally becomes the phase variable for these trajectories. The observation that the roll-over shapes are invariant across walking speed, shoe geometry, and amputee weight motivates this choice. In this strategy, a model-based feedback linearization controller enforces adherence to these desired trajectories as the center of pressure progress through its natural dynamics. This formulation provides both the feed forward torque command and a disturbance response command that provides

exponential converge to the desired rollover shapes.

As we noted earlier for centralized robotic control approaches, a downside of these two trajectory following controllers is their reliance on accurate dynamics models to compute feed forward torques. To overcome this issue, Zhao et al. [2016] propose a model-independent virtual constraint control. In this scheme, quasi-stiffness control provides a feed-forward torque signal that reduces the dependence on the model. A quadratic program then computes the minimum required extra effort to ensure convergence to a preplanned trajectory that is parameterized with respect to hip angle.

2.1.4 Walking Control Summary

The dynamic control prosthesis control strategies we outlined in this section in some sense all provide a feed-forward torque that generates a desired nominal trajectory, and an impedance behavior that determines the disturbance response characteristics. In the case of quasi-stiffness control, the same function encodes both of these characteristics. In the case of trajectory following controllers, model inversion provides the necessary torque to execute the plan while either a proportional derivative controller, feedback linearization, or control Lyapunov function provides impedance behavior.

However, it is not clear that these approaches generate the impedance responses of the system we actually want to replicate in the field of prosthetics, that of the amputee's missing limb. In the biological leg, impedance characteristics may play a crucial role when it comes to stabilizing movement [Won and Hogan, 1995, Burdet et al., 2001] and changes in response to a number of factors including any of mean ankle torque, ankle position, perturbation amplitude, and muscle fatigue [Kearney and Hunter, 1989]. It may be possible to model the both the quasistatic and impedance behaviors via powerful function approximators such as Gaussian Processes or Neural Networks, but these approaches could also suffer from the curse of dimensionality and the difficulty of gathering biomechanical training data. Therefore, in the next section we will discuss approaches that seek to directly model the underlying biological system that generates these behaviors.

2.2 Bioinspired Control

An alternative approach to prosthesis control, which may better model both the joint quasi-stiffness and joint impedance, is to model the underlying biological neuromuscular dynamical system that gives rise to these characteristics. Two hypothesized mechanisms that govern the neuromuscular system are central pattern generators

(section 2.2.1) and reflexes (section 2.2.2). These two mechanisms are naturally decentralized and dynamic and are thus attractive models to utilize in a prosthesis controller.

2.2.1 Central Pattern Generators

Central Pattern Generators in Biology

Central Pattern Generators (CPGs) are hypothesized nonlinear oscillators, comprised of neurons in the central nervous system, that can autonomously generate periodic neural activation patterns [Ijspeert, 2008]. Brown [1911] first suggested their existence based on experiments he conducted on decerebrated and deafferented cats. In these experiments, Brown severed the cat's sensory information pathways (deafferentation) and decerebrated the cats to cut-off high-level commands from the brain to alpha motor neurons. Despite the lack of high level control and sensory feedback, the cats still displayed cyclical motions in their hind legs similar to those seen during normal gait. This result suggests CPGs may play an important role in generating locomotion controls in vertebrate animals. Similar cyclical neural activity (called fictive locomotion) has been found in isolated lamprey spinal cords [Cohen and Wallén, 1980], salamanders [Delvolvè et al., 1999], and frog embryos [Soffe and Roberts, 1982].

Moreover, research has shown that stimulation of a region of the brain stem called the Mesencephalic Locomotor Region (MLR) can manipulate the neural activity generated by CPGs. For example, electrical stimulation of the MLR led to gait transitions in both decerebrated cats [Shik et al., 1966] and salamanders [Cabelguen et al., 2003]. Therefore, CPGs may serve as a form of dimensionality reduction and decentralization for the biological control system as low-dimensional, high-level signals from brain can shape the high-dimensional, low-level CPG output. Consequently, CPGs may also represent an attractive option for generating feed-forward commands for robotic legged systems as decentralization and dimensionality reduction are desirable properties in this domain as well.

Neuromechanical Models and Robot Implementations with CPGs

The seminal work on CPG-based bipedal locomotion control is presented in Taga et al. [1991]. In this model, a CPG neural network of six interconnected oscillators describes the joint torques applied to a five link biped model. Differential equations, first presented in Matsuoka [1987] with additional sensory feedback from joint and inertial link angles, describe the output of the CPG network. The resulting biped model is capable of both running and walking gaits

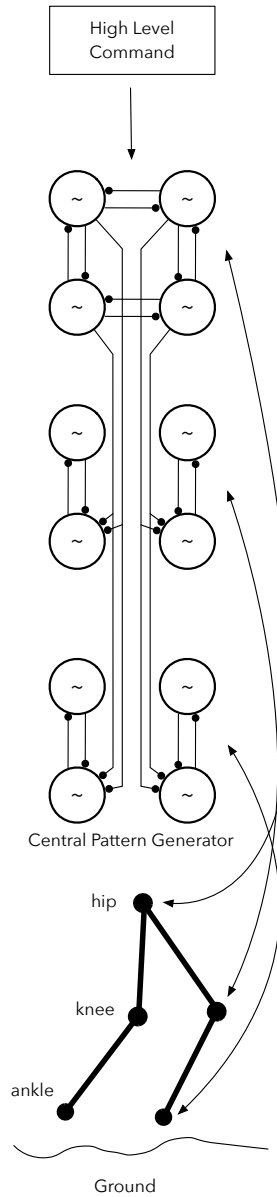


Figure 2.3: Central Pattern Generator for bipedal locomotion as described in Taga et al. [1991]. Six neural oscillators receive feedback from and command joint torques for the hips, knees, and ankles of a planar biped model. A one dimensional high-level control signal enables control of speed and elicits gait transitions.

and demonstrates robustness to a variety of disturbances including changes to ground stiffness, damping, and slope. Additionally, tuning a single parameter induced a transition from walking to running in the model in a manner comparable to the biological gait transitions observed after stimulation of the MLR.

CPGs have successfully controlled several bipedal humanoid robots. For example, Endo et al. [2005] used Matsuoka's nonlinear oscillators along with bio-inspired feedback pathways that regulate ground reaction forces and body roll to generate desired foot trajectories for the bipedal QRIO robot. As in Taga et al.'s simulations walking speed can be controlled via adjustment of a single parameter and the robot is robust to changes in step height. Authors have also successfully employed other nonlinear oscillator models. In Shan and Nagashima [2002], a Recurrent Neural Network generates oscillatory signals for a 20-DOF humanoid robot, HOAP-1, that allow it to walk up and down stairs. In Righetti and Ijspeert [2006], programmable "Hopf" oscillators [Righetti et al., 2006] learn desired walking trajectories through entrainment enabling HOAP-2, a 25-DOF robot, to walk forwards and backwards at varying speeds and step lengths.

CPGs for Prostheses Control

CPGs have also been proposed for controlling both mechanically-passive and active lower limb prostheses. Nandi et al. [2009] optimize CPG parameters to fit recorded knee angle trajectories from healthy human subjects. During walking, the CPG entrains desired knee motions to the oscillations of the amputee's hip joint. The desired knee angles are achieved in a mechanically-passive prosthesis via online adjustment of the knee damping. Similarly, Torrealba et al. [2010] and Mora et al. [2012] also use a CPG to control a mechanically-passive variable damping prosthesis but use phase resetting to synchronize the amputee and CPG dynamics.

For active prostheses, Geng et al. [2012] suggest using a Hopf oscillators to fit the trajectory of the knee angle during walking. Guo et al. [2010] extend the idea of using a CPG for active prosthesis control by proposing a hierarchical approach with a support vector machine (SVM) at the high-level inferring amputee intent from EMG signals, and a CPG at the lower-level determining the desired knee and ankle angles for an active transfemoral prosthesis. However, in both cases, the authors do not provide experimental results on real prosthesis hardware. Moreover, unlike in Taga et al.'s original work, these proposed CPG networks for prostheses generate desired joint kinematics instead of torques. Consequently, these controllers may not allow prostheses to exhibit the dynamism and compliance we

desire.

2.2.2 Neuromuscular Reflexes

Neuromuscular Reflexes in biology

Around the same time Brown hypothesized the existence of central pattern generators, Sherrington [1910a,b] suggested another mechanism for oscillatory neural signals: chains of *reflexes*, or local feedback loops, that trigger in response and entrain to sensory signals. Sherrington identified complex, multi-joint, multi-limb reflex arcs involving both excitation and inhibition in response to cutaneous stimulation in decerebrated cats. Moreover, he observed rhythmic stepping behavior in decerebrated cats suspended off the ground and concluded that the behavior emerged reflexively based on proprioceptive signals emanating from the muscles themselves and not from centrally generated oscillatory signals.

In animal experiments discussed earlier, while CPGs can go a long way towards explaining locomotion neural activity, they still do not fully explain all observed phenomena. Reflexes likely at least shape locomotion activation patterns through entrainment, for example in Lamprey's movement of the tail generates activation in the spinal chord of equal frequency [McClellan and Jang, 1993], and phase resetting, as demonstrated by the ability of decerebrated cats to walk on treadmills across a range of speeds [Rossignol, 2000].

For human and primate bipedal locomotion, the role of CPGs is less clear and the role of reflexes more evident than for decerebrated cats and simpler vertebrate animals [MacKay-Lyons, 2002, Vaughan, 2003, Nielsen, 2003]. This is perhaps due to the demands of controlling the inherently unstable dynamics of upright walking [Capaday, 2002]. For example, while rhythmic spinal activity has been observed in humans, it is not clear if the neural signals are an example of autonomous fictive motion, indicative of a CPG, or entrainment with stretch reflexes in leg muscles [Capaday, 2002, Stewart et al., 1991].

In this case, we can also look to robotics to provide insight about biology: in the previously discussed experiments on humanoid robots controlled by CPGs, a significant reduction in robustness was observed after blocking sensory feedback pathways [Endo et al., 2005, Righetti and Ijspeert, 2006] indicating CPGs alone may not fully explain bipedal locomotion. Whereas research has not yet clearly established the presence of a CPG driving human locomotion, research has identified many reflexes that contribute to locomotion such as stretch reflex in the knee during swing [Garrett and Luckwill, 1983], stretch reflex in the soleus [Yang et al., 1991], soleus force feedback [Grey et al., 2007], and cutaneous reflexes that induce

withdrawal responses [Yang and Stein, 1990].

Neuromuscular Models with Reflexes

To model the potential interplay between muscular reflexes and CPGs in human locomotion Ogihara and Yamazaki [2001] extend the model presented in Taga et al. [1991] by adding muscles stimulated by alpha motor neurons. This model simulates nine muscles of the leg, each stimulated by an alpha motor neuron that receives input from a CPG oscillator and proprioceptive feedback from one or more muscles. The muscles produce forces according to their state and activation input (computed using models presented in Pierrynowski and Morrison [1985] and Davy and Audu [1987]). These forces are applied to constant moment arms in order to produce joint torques summed about joints as in a virtual model control. The authors optimize the cost of transport of the biped with a genetic algorithm and achieve a gait with human-like kinematics and kinetics. Moreover, the forces produced by many of the muscles resemble those produced during human locomotion. Despite the fact that the CPG used in this model received no feedback signals, the resultant gait still exhibited a small degree of robustness to perturbations although not as much as Taga et al.'s model. The author's attribute the robustness to the stabilizing feedback provided by muscle reflexes.

Whereas models and robot experiments show reflexes are vital for maintaining bipedal gait stability, the same cannot be said about CPGs. In fact, as shown by Geyer and Herr [2010], it is possible to simulate robust and human-like bipedal locomotion using only reflexes. This work employs a neuromuscular model, similar to that used in Ogihara and Yamazaki [2001], but does away with the feed forward CPG stimulations sent to alpha motor neurons. Instead, Geyer and Herr hypothesize the existence of several force and length muscle reflexes that implement three key aspects of bipedal locomotion: compliant leg behavior, preventing joint over extension, and providing trunk stabilization. The gait achieved by this model is more robust than and more accurately reproduces kinematics, kinetics, and ground reaction forces seen in human walking than Ogihara and Yamazaki's model. Moreover, it also produces human-like stimulations for many of its muscles.

While we cannot say based on this result alone that CPGs do not play an important role in human locomotion, the fact that human locomotion can emerge from purely reflexive controls increases the attractiveness of using this approach for prosthesis control. The reflex-only paradigm may be easier to design and optimize than the CPG+reflex paradigm for two reasons: First, the reflex connec-

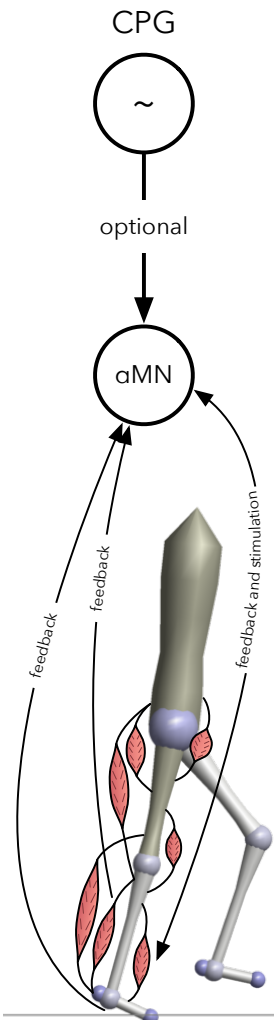


Figure 2.4: Neuromuscular models with reflex feedbacks. The model developed by Ogihara and Yamazaki [2001] activates individual muscles according to the activity of a CPG and proprioceptive reflexes that can involve the muscle itself, other muscles, and ground contact sensing. Geyer and Herr [2010] does away with the CPG and achieves locomotion with only reflex feedbacks.

tion graph used by Geyer and Herr [2010]’s reflex-only model is much more sparse than that used by Ogihara and Yamazaki [2001] CPG+reflex model. Using a sparse set of reflexes and no CPG reduces the number of parameters that we must tune in order to achieve locomotion. Second, the reflexes in the reflex-only model are functionally motivated, which may increase our intuition about the role of each reflex and assist our ability to tune the model’s parameters. This is evidenced by the fact that Geyer and Herr hand tuned the parameters of their model whereas Ogihara and Yamazaki used a genetic algorithm. Moreover, functionally motivated feedbacks used in the reflex-only approach has allowed further research to extend this model to include swing leg placement [Desai and Geyer, 2013], 3D locomotion, running, speed changes, stair and slope negotiation, turning, and obstacle avoidance [Song and Geyer, 2015].

The robustness properties exhibited by neuromuscular model are especially relevant to our goal of developing a robust prosthesis control that will help transfemoral amputees avoid falls. In Song and Geyer [2015] the author’s improve the model’s robustness by incorporating reflexes that place the swing leg into target landing angles. The authors optimize this model to achieve a combination of robustness and energy efficiency. The resulting gait can walk on terrains featuring random steps up to ± 6 cm (50 % success rate) and rejects pushes in both the forward and backward directions at various points in the gait cycle. In another work, Murai and Yamane [2011] subject a neuromuscular model, initially trained to match kinematic data of single subject, to impacts during early and late swing. They find the learned model exhibits the elevating and lowering trip response strategies of the biological leg despite not being explicitly trained to do so. These disturbance response characteristics point to reflex control providing the appropriate quasi-static and impedance behaviors.

Neuromuscular Reflexes for Prosthesis Control

Motivated by the robustness and natural gait achievable by neuromuscular reflex control, past research has applied this model to active prostheses and exoskeletons. Eilenberg et al. [2010] applied a simplified version of the control to a powered ankle prosthesis (fig. 2.5). In this work, the neuromuscular model was reduced to a single ankle plantarflexor muscle driven by a positive force feedback reflex during stance. During swing, the control applies torque to dorsiflex the ankle according to a virtual spring damper model. In amputee testing of a prosthesis controlled by the neuromuscular model the control produced ankle kinematics and kinetics similar to those observed in

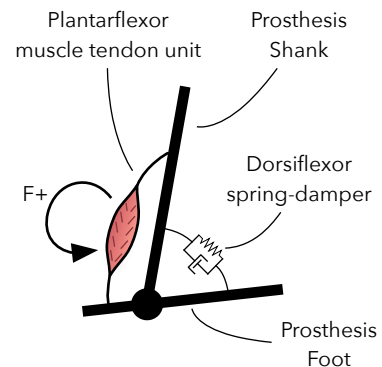


Figure 2.5: Neuromuscular model used by Eilenberg et al. [2010] to control an active ankle prosthesis. During stance, a virtual muscle driven by positive force feedback, generates plantarflexion torque. During swing, a virtual spring damper provides dorsiflexion torque to prevent toe scuffing.

healthy human walking. Significantly, Eilenberg et al. found evidence that the robustness and entrainment properties observed in neuromuscular model simulations may carry over to amputee gait as well. The author's note that the prosthesis automatically adapts torque output when walking on slopes, producing more plantarflexion torque when walking up slopes and less when walking down slopes. Additionally, Markowitz et al. [2011] found that a similar neuromuscular reflex model automatically produced more ankle plantarflexion work as the amputee increased his gait speed.

EMG-based Control

The inclusion of user intent recognition via surface electromyography (EMG) signals represents an interesting extension of neuromuscular reflex prosthesis control. In these approaches, muscle activity in the residual limb is directly measured via EMG sensors embedded in the amputee's prosthesis socket. These EMG sensors are then used to control the torque generation of the amputee's leg prosthesis. Because neuromuscular models describe how joint torque is generated in response to muscle activations, a natural approach is to use the EMG signal in reflex pathways in order to activate virtual muscles. This is the approach proposed by Wu et al. [2011]. In this work, Wu et al. control an active transfemoral prosthesis using EMG sensor readings from the residual thigh to activate virtual knee flexor and extensor muscles according to a linearised Hill muscle model. The resulting prosthesis control allowed an intact subject wearing the prosthesis via an able-bodied emulator to achieve nearly normal gait. In a similar approach, Wang et al. [2013] use EMG signals to modify the gain on a positive torque feedback loop (similar to positive force feedback used in Geyer and Herr [2010]) in order to control ankle plantarflexion torque. As seen in healthy human walking, toe off angle and ankle net work increased with increasing walking speed.

These two works have demonstrated that neuromuscular approaches have enabled EMG based control to go beyond its typical application of high-level mode recognition. For example, Huang et al. [2009, 2011], and Hargrove et al. [2015] recognize walking modes, such as level ground walking, ramp and stair ascent, and ramp and stair descent, by training classifiers on features of EMG and mechanical sensor data. In contrast, the EMG + neuromuscular approaches allow the use typically noisy EMG sensor data for low-level continuous control. Wu et al. [2011] and Wang et al. [2013] propose that because EMG + neuromuscular approaches model physiologically plausible feedback loops and dynamics, they may allow amputees to use muscle activations to control their prostheses in an intuitive way.

2.2.3 Conclusion

In summary, simulations and implementations of the neuromuscular reflex control approach have repeatedly demonstrated its ability to generalize to a variety of situations and exhibit robustness to a variety of disturbances. Due to the gait deficits and fall risk transfemoral amputees face, these two properties make this control paradigm very attractive for application to transfemoral prostheses. Moreover, neuromuscular approaches have been successfully extended with EMG sensor feedback from amputees' residual limbs, enabling intuitive low-level prosthesis control. In contrast, other control approaches for prostheses such as quasi-stiffness control have not demonstrated these properties. Importantly, neuromuscular control addresses challenges 1 and 2 of amputee locomotion (section 1.1.1) as we can implement them via a decentralized, sparse set of reflexes and they allow for dynamism by providing both a quasi-stiffness and impedance response via the dynamics of the stimulated muscle models..

As yet, there have not been any published works applying neuromuscular reflex control to active knee and ankle transfemoral prostheses. Therefore, in this thesis, we work towards this goal with the hope of improving transfemoral amputee gait robustness and naturalness. Chapter 3 will review the details of the particular neuromuscular implementation used in this thesis.

2.3 Prosthesis Design

We can trace efforts to build an active knee-ankle prostheses to the seventies when Flowers [1974] created an active knee-ankle prosthesis emulator in order simulate potential control schemes. This prosthesis used a hydraulic actuator capable of producing $90 \text{ N} \cdot \text{m}$ of torque and 0.5 rev/s of no-load speed, sufficient for simulation of passive prostheses. With this device, Donath [1974] tested proportional EMG control, a problem researchers are still investigating today (see section 2.2.2). Indeed, this line of research proved to be far ahead of its time, as most relevant research in active lower-limb prostheses design has occurred only in the last ten years. The recent interest in active knee ankle prostheses has been spurred by hardware improvements that allow designs to approach the strength, speed, and low weight of the biological leg. Enabling technologies include power-dense brushless motors, motor controllers, and lithium-ion batteries, inexpensive microcontrollers and inertial measurement units (IMUs), and strong but light composite materials such as carbon fiber. With these advancements, engineers have successfully designed prostheses to meet or exceed the requirements for walking (table 2.1).

	Ankle Max	Knee Max
Velocity	0.72 rev/s	1.17 rev/s
Torque	$130 \text{ N} \cdot \text{m}$	$57 \text{ N} \cdot \text{m}$
Power	350 W	120 W

Table 2.1: Required knee and ankle torque, velocity, and power for walking (1.40 m/s average speed, scaled to 85 kg subject, data from Winter [2009])

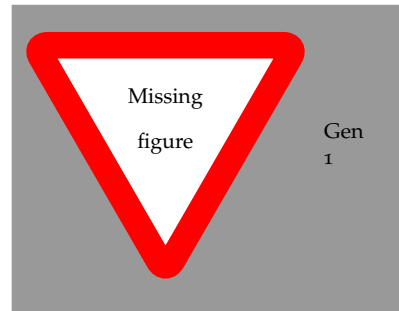
In this section, we review a number of recent prosthesis designs and analyze their ability to enable dynamic locomotion (challenges 1 and 2 of transfemoral prosthesis locomotion). To address this challenge, prostheses should be able to regulate their output joint torques and behave as though they have inertial properties similar to that of a normal human leg. This will ensure that the prosthesis will emulate the energy efficient gaits of normal walking and remain compliant to unforeseen disturbances and uneven terrain.

2.3.1 Rigid Transmission Transfemoral Prostheses

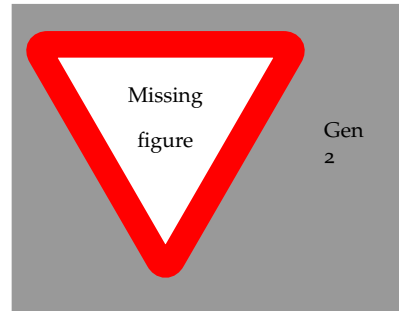
The most common approach for active transfemoral prosthesis design employs electric motors with transmissions that are rigidly coupled to the knee and ankle joints. The transmissions may utilize a combination of gears, chains, belts, ball screws, and four-bar-mechanisms in order to increase the torque output of the actuator, at the expense of speed, in order to satisfy the requirements listed in table 2.1. A successful line of transfemoral prostheses following this design paradigm comes from Vanderbilt university. The first prosthesis in this line (fig. 2.6a) used a pair of ball screw transmissions and brushless motors capable of 200 W of continuous power output to drive its knee and ankle joints [Sup et al., 2009].

With these actuators, the knee motor can achieve the required peak torque and peak power intermittently (table 2.1). However, the ankle motor may be overly stressed due to the high requirements of walking. To remedy this, this prosthesis includes of a unidirectional parallel spring in the ankle that reduces the required ankle motor torque. As shown in figure fig. 2.7, during level ground walking, a linear torsion spring accounts for a significant portion of the ankle's torque versus angle relationship. Therefore, incorporating a spring into the ankle offloads this portion of the torque from the motor. The ankle motor only needs to provide the difference between the desired output torque and the linear spring. As a result, the spring reduces motor energy consumption, heat generation, and transmission wear.

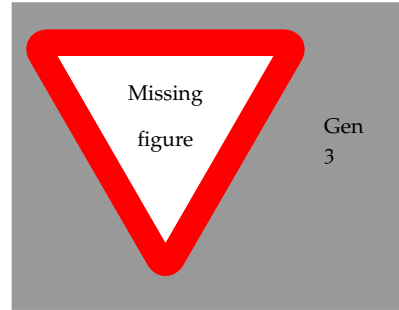
Further improvements resulted in two more generations of prostheses (figs. 2.6b and 2.6c) [Lawson et al., 2013, 2014]. These versions replaced ball screw transmissions with a multi-stage belt/chain due to the improved packaging and reduced noise and wear they afford (Michael Goldfarb, personal communication, September 18, 2013). With these prostheses, researchers have extensively tested a variety of control strategies including quasi-stiffness control [Sup et al., 2009, 2011, Lawson et al., 2013, 2014, Lenzi et al., 2014b], EMG-based control [Ha et al., 2011, Varol et al., 2010], minimum jerk trajectory following [Lenzi et al., 2014a], and virtual constraint control [Gregg



(a) Generation 1 used ball screw transmissions, 200 W brushless motors, and a unidirectional parallel spring in the ankle that reduced motor torque requirements [Sup et al., 2009].



(b) Generation 2 replaced ball screws with custom gear-based transmission that is less noisy and more durable [Lawson et al., 2013].



(c) Generation 3 features a modular design with separable knee and ankle units [Lawson et al., 2014].

Figure 2.6: Vanderbilt University's Robotic Transfemoral Prostheses.

et al., 2014].

Additional prostheses in the rigid transmission category include AMPRO [Zhao et al., 2016], and a commercially available active knee and ankle prostheses: the Össur Power Knee and Proprio Foot. The AMPRO prosthesis features two 374 W motors coupled to Harmonic Drive transmissions. Zhao et al. [2016], use this prosthesis to assess the merits of a virtual constraint controller. The Össur Power Knee features an electric motor that can provide torque to facilitate sit-to-stand motions, stair climbing, and active extension and flexion during walking. The Proprio Foot also features electric actuation that allows it to adapt to terrain and dorsiflex the ankle during swing to help avoid trips.

Torque Control Strategies for Rigid Transmission Prostheses

In order to achieve dynamic locomotion capabilities, it is crucial that prosthesis designs allow for closed loop control of torques. To do this control system must be able to accurately measure the torque at the joint output. There are two main strategies for torque measurement used by prostheses with rigid transmissions.

The first strategy is to measure the current draw of the motors windings, which is related linearly to the motor torque. One can then multiply this measurement by the gear ratio to obtain an estimate of the output joint torque. This is the method used by Generations 2 and 3 of the Vanderbilt prosthesis as well as the AMPRO prosthesis. The benefit of this method is that it utilizes existing hardware and allows one to use high frequency current control modes of motor drivers. However, a drawback of this method is that it measures the torque before the transmission. Consequently, it does not account for frictional losses, which can be difficult to model, especially for geared systems. A strategy that deals with this problem is to install load cells in series with the motor after the transmission, as was done on Generation 1 of the Vanderbilt prosthesis. With this method, the closed-loop control can compensate for frictional losses as they are included in the torque measurement.

However, this method may still not address a second problem: sluggish passive dynamics caused by reflected inertia and damping. Reflected inertia refers to the apparent magnification of motor rotor and gearing inertia on the outside of gearbox. We can derive this effect through Newton's second law for the geared motor

$$J_i \ddot{\theta}_i = \tau_i - b_i \dot{\theta}_i. \quad (2.5)$$

Here, θ and its derivatives refer to angular states of the motor, b is the damping constant, J is the inertia and τ is the motor torque.

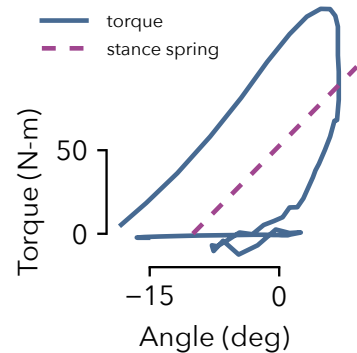


Figure 2.7: Torque vs angle relationship for the ankle during level ground walking. A linear spring relationship captures a significant portion of ankle function during stance. Data from Winter [2009] scaled to 85 kg subject.

We use subscript i to refer to these quantities as seen before the gear reduction, and subscript o to refer to those quantities reflected outside of the motor. Plugging in $\theta_i = n\theta_o$ and $\tau_i = \frac{1}{n}\tau_o$, where n is the gear ratio, and multiplying through by n yields

$$J_i n^2 \ddot{\theta}_o = \tau_o - b_i n^2 \dot{\theta}_o \quad (2.6)$$

$$\implies J_o \ddot{\theta}_o = \tau_o - b_o \dot{\theta}_o. \quad (2.7)$$

These equations show that the inertia and damping of the motor rotor are amplified by the square of the gear ratio. As prostheses may often use gear ratios in excess of 100:1, this effect can be substantial.

	Knee	Ankle
rotor inertia	0.035 kg · cm ²	1.210 kg · cm ²
gear ratio	176:1	115:1
reflected inertia	0.11 kg · m ²	1.6 kg · m ²
human inertia	0.66 kg · m ²	0.019 kg · m ²
percent increase	17%	8400%

For example, table 2.2 shows the calculated reflected inertias of the Maxon Motors used in Generation 3 of the Vanderbilt prosthesis and compares the values to the estimated inertia of the shank and foot about the knee and the foot about its center of mass. We see that at the knee, the reflected inertia is roughly 17% of that of the human shank and foot. In practice, this value is likely several times higher after including the inertia of the encoder, bearings, and gearing. Consequently, we can estimate that the reflected inertia may be on the order of the leg itself. At the ankle, the reflected inertia of the rotor alone is several orders of magnitude more than that of the foot and more than twice that of the shank and foot. When we also consider reflected damping and friction, the dynamics of prosthesis system may be significantly slower than assumed.

The increase in joint impedance created by transmissions could present an issue when attempting to execute dynamic behaviors involving impact such as running or trip recovery. In an impact event, the impulse will move through the system at the speed of sound through metal, roughly 6420 m/s for aluminum [Lide, 2004]. If the prosthesis is 0.5 m long, the shock will traverse its length in 0.00008 seconds. This is about 10 times faster than the typical 1000 Hz control frequency of prosthesis control systems, rendering closed loop torque control with load cells unresponsive. The impact shock could cause damage to gearing and discomfort for the amputee.

Table 2.2: Estimated reflected inertia at knee and ankle joints of Generation 3 Vanderbilt Prosthesis [Lawson et al., 2014]. Motor data taken from Maxon Motors Catalog [Motor, 2016b,a] Knee reflected inertia compared to inertia of human shank and foot about knee. Ankle inertia compared to human foot about its center of mass. Human inertias estimated from Winter [2009] for an 85 kg, 1.7 m tall person.

2.3.2 Design of Dynamic Prostheses

In contrast to the rigid transmission actuation discussed in the previous subsection, prostheses that employ series elastic actuation may be better poised to achieve dynamic locomotion [Pratt and Williamson, 1995]. This actuation scheme (illustrated in fig. 2.8) aims to solve the torque measurement and impedance amplification caused by transmissions by placing a spring in series with the actuator. Measuring the deflection of the spring allows for accurate closed-loop control of the joint torque. Moreover, the spring low-pass filters external impulses, granting the control system more time to move the motor rotor in response to the external load. Due to these properties, designers have integrated series elastic actuators into a number of bipedal robots that seek to achieve dynamic locomotion such as M2V2 [Pratt and Krupp, 2008] and ATRIAS [Grimes, 2013].

Series elastic actuators have found use in a variety of transtibial and transfemoral prostheses. We can further split these applications into two categories, those that optimize the spring stiffness for control bandwidth subject to shock tolerance and those that optimize spring stiffness to optimize efficiency.

Springs for Bandwidth and Shock Tolerance

Adding a spring between the gear and load introduces additional dynamics between external torques and torques applied to the gearbox as external torques must physically displace the load before they generate torque on the motor. This property can improve the shock tolerance of SEA actuators over that of direct drive motors [Robinson, 2000]. However, by the same token, the SEA also introduces additional dynamics between motor torque and load torque, hence reducing force control bandwidth. Therefore, a trade-off exists between the compliance of the actuator and speed with which it can generate desired torques.

Au et al. [2007], Au and Herr [2008] design powered ankle prostheses with this trade off in mind. In these publications, the authors find that using an SEA spring soft enough to protect the ball screw transmission results in insufficient closed loop torque control bandwidth. To overcome this shortcoming, the authors incorporate a parallel spring into the ankle as was done for some of the knee and ankle prostheses discussed in section 2.3.1. Because the parallel spring offsets the motor's torque requirements, Au and Herr find that it also improves the bandwidth of the system from 4 Hz to 20 Hz, thereby exceeding the requirement for walking.

Caputo and Collins [2013] also used series elastic actuators in a robotic prosthesis testbed. This system uses a large, 1.61 kW offboard

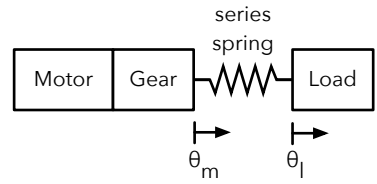


Figure 2.8: Series elastic actuation inserts a spring between the gear output and the load (here drawn as linear actuator for simplicity). Torque is measured via the spring deflection, $\tau = k(\theta_l - \theta_m - \theta_0)$ where τ is the output joint torque, k is the spring constant, and θ_l and θ_m are the load and motor positions and θ_0 is the spring's rest length.

motor connected to a light-weight prosthesis end-effector via a Bowden cable transmission. The Bowden cable applies forces to one end of a fiberglass leaf spring strain gauges measure its deflection. The author's note that the series springs isolate the prosthesis end effector from the motor's rotor inertia. With this system the authors achieve a large peak output torque ($175 \text{ N} \cdot \text{m}$) and high bandwidth (17 Hz), allowing them to rapidly test the effects of different control strategies and emulate prosthesis hardware [Caputo et al., 2015].

Springs for energy efficiency

Designers can also tune series elasticity in order to improve energy efficiency by mimicking the role of tendons in the biological human leg. In the human ankle, the Achilles tendon, which is in series with the ankle plantarflexor muscles, stores energy throughout stance and releases it just prior to toe-off, producing a surge of mechanical power. During this process, the ankle plantarflexor muscles hold the proximal end of the tendon nearly stationary via isometric contraction. This kind of length-preserving muscle contraction consumes relatively little metabolic energy compared to concentric or length-shortening contractions [Rall, 1984]. Consequently, ankle elasticity helps store and release energy, thereby improving metabolic cost of walking [Sawicki et al., 2009].

Similarly, the SPARKy prosthesis uses a *Robotic Tendon* comprised of helical springs in series with the motor to store and release energy ankle energy during stance [Hitt et al., 2007, Bellman et al., 2008, Holgate et al., 2008]. Adding a series spring changes the ankle motor movement to that required to generate desired output torque given the stiffness of the spring and trajectory of the ankle joint⁴. Therefore, with a properly tuned series spring the design reduces motor movement and thus required motor power from 250 W to 77 W [Hitt et al., 2007].

Transfemoral prosthesis designs have also sought to use springs in the knee joint in order to improve energy efficiency. However, these prostheses require more sophisticated designs due to the complex behavior of the knee. Whereas a single spring relationship explains a significant portion of ankle joint behavior (fig. 2.7), as shown in fig. 2.9, the knee joint requires two springs: one for early stance and one for pre-swing and swing. Two prostheses that tackle this design problem are AAAKP (agonist-antagonist active knee prosthesis) [Martinez-Villalpando et al., 2008, 2011] and the CSEA (clutchable series elastic actuator) knee [Rouse et al., 2014, 2015].

The AAAKP prosthesis uses two unidirectional springs, one for extension and one for flexion, each in series with its own actuator.

⁴ $\theta_m = \theta_l - \tau/k - \theta_0$, where τ is the desired ankle torque, θ_l is the ankle trajectory, and k and θ_0 are the spring stiffness and offset

With this setup, AAAKP is able to store energy during the knee flexion phase just after heel strike, and transfer it to a flexion spring for use during pre-swing and swing. The prosthesis consumes just 5.6J/stride. However, the downside of this design is inefficient use of actuator mass, as two electric motors are required, one for extension and one for flexion.

A second concept is to use a series elastic actuator with a clutch on the motor [Rouse et al., 2014, 2015]. The clutch saves energy by holding the motor side of the series spring stationary while the spring is loaded in early stance; no electrical energy is consumed holding the rotor in place. In this design the spring-like behavior of the knee during swing is reproduced by the electric motor alone unlike in the AAAKP prosthesis. Despite this, the CSEA knee consumes less energy than the AAAKP, just 3.6J/stride. Moreover, the simplified design of the CSEA has a mass of 2.7 kg vs 3.6 kg for the AAAKP.

A potential drawback of SEA designs that are tuned for energy efficiency is that they typically tune the spring stiffness to match observed quasi-stiffness of the biological joint during a certain phase of the gait. However, this stiffness value is not necessarily that which maximizes torque control bandwidth. Therefore, while prostheses tuned for efficiency can consume less energy, which is desirable for a product needing long battery life, they may not represent the most versatile design for evaluating new control ideas or different gait modes.

2.4 Stumble Recovery for Prostheses

The prosthesis controls we reviewed in sections 2.1 and 2.2 primarily sought to reproduce typical walking kinematics and dynamics. Some control strategies, such as neuromuscular reflex control (section 2.2.2) also demonstrated the ability to generalize to sloped walking and changes in speed by producing more push off work in these situations [Eilenberg et al., 2010, Markowitz et al., 2011]. However, it is not clear that the low-level reflexes in the neuromuscular control model will generate trip recovery responses, which in human control likely utilize more complex supraspinal and cortical reflexes [Eng et al., 1994, Schillings et al., 2000, Hofstad et al., 2009]. We therefore seek to improve upon neuromuscular control's inherent stability by augmenting it with explicit trip detection and recovery actions.

As discussed in section 1.1, falling and the fear of physical activity it engenders are two major issues amputees face [Miller et al., 2001]. Avoidance of physical activity can potentially cause deterioration of strength, balance and control, which may lead to further inactivity, debilitation, and social isolation. Currently, the microprocessor con-

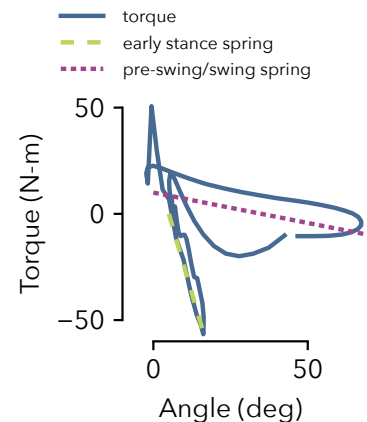


Figure 2.9: Torque vs angle relationship for the knee during level ground walking. Knee displays more complicated functionality than the ankle (see fig. 2.7), with two distinct springs need to explain early stance and pre-swing/swing behavior. Data from Winter [2009] scaled to 85 kg subject.

trolled, mechanically-passive prostheses feature trip recovery modes that “lock” or highly damp knee movement. However, Bellmann et al. [2010] show that these modes fail to adequately respond to trips during a large portion of swing due to knee buckling at touch-down. It is unclear that passive, locking responses are intuitive for amputees or coordinate well with innate trip recovery responses, which can require positive joint power [Cordero et al., 2005]. The advent of active transfemoral prostheses gives us the opportunity to replicate amputee’s preferred responses, which will hopefully yield more effective and intuitive fall-prevention actions.

2.4.1 Responses to Trips

Able-bodied persons primarily use two strategies to recover from trips to their swing legs: When tripped in early swing, people usually use an *elevating strategy*, in which the knee is actively flexed to lift the foot over and in front of the obstacle. In late swing, people typically use a *lowering strategy*, in which knee extensor muscles rapidly bring the foot in contact with the ground in front of the obstacle [Eng et al., 1994]. In response to mid-swing trips, people may use either strategy [Schillings et al., 2000]. Finally, people also use the *delayed lowering* strategy in early swing. This strategy is an aborted attempt at an elevating strategy, followed by a lowering strategy, and is used when the toe catches on the obstacle [Eng et al., 1994].

Interestingly, Shirota et al. [2015] show that transfemoral amputees using mechanically-passive prostheses utilize these same strategies despite the lack of control and positive power production at the knee joint. Amputees compensated for these deficiencies and achieved elevating, lowering, and delayed lowering foot trajectories via movements of the hip and sound side leg. The lack of sensory feedback information from the prosthesis leg to the nervous system did not seem to impede utilization of these strategies. Consequently, the authors hypothesize that mimicking able-bodied responses to trips may also be intuitive for amputee subjects.

While amputees using mechanically-passive prostheses exploit the same strategies as able-bodied subjects for trip recovery, they do not use these strategies in the same proportions during the phases of swing as do able-bodied subjects. Amputees typically use elevating strategies less frequently and lowering strategies more frequently. This difference increases when the prosthesis is the stance leg, and the intact leg is tripped. A possible reason for decreased reliance on the elevating strategy may stem from the inability of mechanically-passive prostheses to produce positive joint power. Cordero et al. [2005] show that in an elevating strategy, positive power is required

in the swing-leg's knee joint in order to rapidly flex the knee to achieve obstacle clearance. Likewise, Pijnappels et al. [2004] show that powered stance leg push-off helps raise the foot during the elevating strategy. Empowering transfemoral prostheses with active joints may help amputees more easily realize the elevating strategy, normalize amputee trip recovery strategy selection, and allow them to recover from a larger range of disturbances.

2.4.2 Trip Detection and Classification

Human responses to gait disturbances likely involve signal processing at the supraspinal and cortical level. This is evidenced by the relatively high latency (> 100 ms) of EMG signals relevant to the utilized strategy, the utilization of both elevating and lowering strategies in mid-swing, the existence of the delayed lowering strategy [Schillings et al., 2000], and the inconsistent resolution of motor redundancy during the lowering strategy [Eng et al., 1994]. Furthermore, Hofstad et al. [2009] found that latencies are further increased for amputee subjects executing obstacle avoidance tasks, suggesting that amputee trip recovery may require additional data processing and cognitive control as compared to able-bodied persons.

A control system that seeks to be intuitive and effective for amputees by mimicking their responses to trips needs to be able to model these complexities. As a result, researchers have relied on data-driven, machine learning approaches to detect and classify trips so that prostheses can take the appropriate actions. All systems proposed to date use a two-layer classification scheme, where the first layer distinguishes trips from normal walking, and the second layer classifies the recovery strategy as either elevating or lowering. The first such system by Lawson et al. [2010] used Fast Fourier Transform features of data collected from six accelerometers placed on the lower limb. To collect training data, the author's outfitted healthy subjects with sensors, and randomly subjected them to trips. They classified stumbles from normal walking via a threshold on power between 10 and 40 Hz and classified elevating versus lowering strategies based on the root-mean-squared thigh acceleration in a 50 ms window before the stumble. Zhang et al. [2011] further add EMG sensors to the trip detection system, and employ outlier detection methods so that the trips were not required in the training dataset. They find EMG sensors improve the false alarm rate, at the expense of classification latency. However, the false alarm rate is still quite high, corresponding to an incorrect positive classification every 1.6 min. Finally, Shirota et al. [2014] use linear discriminant analysis on kinematic features from the tripped leg. They find evidence supporting

the use of the two-stage classification scheme, and identify the optimal update frequency and length for the window in which they compute features.

A major drawback of these previous works is that they report error rates based on offline validation results; *i.e.* they collect data from subjects who are responding to trips and then evaluate how well the classifier would have performed on the collected data. This is fundamentally different than online validation, in which one reports the error rate obtained when using the learned classifier to control the system. Previous work on a classifier for recognizing gait modes such as level walking and stair and ramp ascent and descent found that online error rates were significantly higher than offline error rates [Hargrove et al., 2015]. As we discuss in section 5.3, it is likely this trend will hold true for stumble classification as well.

2.5 Backgorund Summary

From this literature review, we see that in order to achieve dynamic prosthesis behaviors, such as trip recovery, both the prosthesis controls and mechanical must address both the nominal walking gait as well as the disturbance response. We see a clear trend in the literature in this direction: Control algorithms have evolved from kinematic strategies that follow preplanned trajectories with stiff position control to dynamic strategies that allow us to design both the nominal trajectory the disturbance response characteristics. Likewise, in prosthesis design we see a trend towards series elastic actuators that enable accurate sensing and control of the prosthesis joint torque. With these actuators, we can design prosthesis joints that can simulate the passive dynamics of the human leg, allowing for natural interactions with the environment.

In this thesis, we intend to take an integrated approach to the hardware and control design in order to maximize the dynamism of the resulting system. We plan design and build a series elastic actuator transfemoral prosthesis, capable of executing dynamic motions, and combine it with neuromuscular reflex control, which provides a unified explanation for both the quasistatic and impedance behaviors of the human leg. With this approach, we hope the prosthesis will be respond to smaller disturbances like biological human leg and will be able to execute dynamic trip recovery responses such as the raising and lowering strategies in response to larger disturbances.

3

Neuromuscular Model

In this thesis we intend to investigate the ability of neuromuscular reflex control to improve amputee gait robustness. To this end, here we provide a more detailed review the neuromuscular model components on which we base our prosthesis control. Four parts comprise the model: a mechanical simulation environment we use to obtain simulation results (section 3.1), biological motors modeled by the hill muscle model that apply torques to joints (section 3.2), and finally functionally-motivated stance (section 3.3) and swing (section 3.4) reflexes that implement the key behaviors required for walking.

3.1 Mechanical Model

To obtain the simulation results we present in section 4.2, we construct a mechanical model in the Matlab Simscape Multibody environment similar to those presented in Geyer and Herr [2010], Song et al. [2013], Song and Geyer [2015]. This model represents the seven link biped in fig. 3.1 and includes two legs with thigh, shank, and foot segments as well as a lumped head-arms-trunk (HAT) segment. Table 3.1 lists the segment lengths, center of mass and joint locations measured from the distal end, masses, and inertias that approximate those of a 80 kg, 1.8 m tall person.

The mechanical model interacts with the environment through ground reaction forces on the toes and balls of the feet. Specifically, we use a 2-dimensional reduction of the 3D ground contact model

	Feet	Shanks	Thighs	HAT
l (cm)	20	50	50	80
d_{COM} (cm)	14	30	30	35
d_{Joint} (cm)	16	50	50	
m (kg)	1.25	3.5	8.5	53.5
J (kg)	0.005	0.05	0.15	3

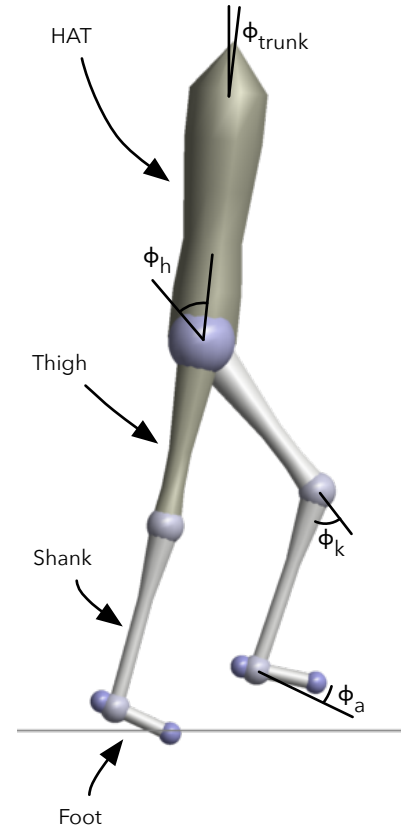


Figure 3.1: The skeletal model we use to simulate neuromuscular reflex control. The model consists of seven segments: left and right feet, shanks, and thighs, as well as a lumped head-arms-trunk (HAT) segment. Flexion joint angles are positive, extension joint angles are negative, and the zero angle configuration represents standing.

Table 3.1: Segment lengths (l_s), center of mass (d_{COM}) and joint (d_{Joint}) locations measured from the distal end, masses (m), and inertias (J) approximated from Günther and Ruder [2003].

presented in Song and Geyer [2013] to calculate forces in the normal and tangential directions with respect to the terrain. In the normal direction the force is

$$F_n = k_n \Delta n_c (1 + \dot{n}_c) (\Delta n_c > 0) (\dot{n}_c / v_{\max} > -1), \quad (3.1)$$

where $k_n = 78.45 \text{ N/mm}$ is the stiffness coefficient in the normal direction and Δn_c and \dot{n}_c are the penetration direction and velocity in the normal direction. The form of the normal force is inspired by Günther and Ruder [2003] and Scott and Winter [1993] and represents a linear spring with multiplicative damping. $v_{\max} = 3 \text{ cm/s}$ represents the maximum recovery velocity of the ground. If \dot{n}_c exceeds this velocity, ground contact is lost.

In the tangential direction, a state machine switches between two force models representing sliding and static friction. Sliding friction is given by

$$F_{t,slide} = -\text{sign}(\dot{t}_c) \mu_{slide} F_n \quad (3.2)$$

while static friction is given by

$$F_{t,static} = -k_t \Delta t_c \left(1 + \text{sign}(\Delta t_c) \frac{\dot{t}_c}{v_{\max}} \right), \quad (3.3)$$

where Δt_c is the penetration in the tangential direction \dot{t}_c is the penetration velocity, $\mu_{slide} = 0.8$ is the sliding coefficient of friction, and $k_t = 78.45 \text{ N/mm}$ is the stiffness coefficient in the tangential direction.

The contact model begins in the sliding mode and switches to the static mode if $\dot{t}_c < 1 \text{ cm/s}$. It switches back to the sliding mode when $|F_{t,static}| < \mu_{static}|F_n|$, where $\mu_{static} = 0.9$.

Finally, the biped skeletal model includes soft joint limits to represent the skeletal joint limits on the knee, ankle, and hip joints. The functional form of the soft limit joint torque is identical to that of the normal ground reaction force given by eq. (3.1).

$$\tau_{jl} = k_{jl} \Delta \phi_{jl} (1 + \dot{\phi}_{jl}) (\Delta \phi_{jl} > 0) (\dot{\phi}_{jl} / \dot{\phi}_{\max} > -1), \quad (3.4)$$

where $k_{jl} = 0.3 \text{ N}\cdot\text{m/deg}$ is the joint stiffness $\Delta \phi$ and $\dot{\phi}_{jl}$ are the joint limit penetration angle and velocity respectively, and $\dot{\phi}_{\max} = 1 \text{ deg/s}$ is the maximum joint limit retraction velocity. Table 3.2 lists the engagement angles for the joint limits.

To obtain simulation results, we simulate the mechanical system with the `ode15s` variable step solver. We set the maximum step size to 10 ms, relative error tolerance to 10^{-4} , and absolute error to 10^{-6} .

Joint	ext. lim.	flex lim.
hip		50
knee	5	
ankle	-40	20

Table 3.2: Joint limits for the hip, knee, and ankle joints listed in degrees. Positive joint angles represent flexion and negative joint angles represent extension (see fig. 3.1).

3.2 Hill Muscle Models

Our proposed transfemoral prosthesis control is comprised of biological muscle actuators that are stimulated according to hypothesized reflex pathways. Specifically, we use a Hill-type *muscle tendon unit* (MTU) developed in Geyer and Herr [2010]. It is comprised of a contractile element (CE) that represents muscle fibers and produces force when activated, a parallel elastic (PE) element that represents the stiffness of the collagen tissue between muscle fascicles, and series elastic (SE) element that models tendon stretch. Figure 3.2 shows the arrangement of these elements. Note that the PE and SE both are unidirectional springs with engagement lengths of l_{opt} and l_{slack} respectively.

The CE generates force according to

$$F_{\text{CE}} = F_{\max} A f_l(l_{\text{CE}}) f_v(v_{\text{CE}}). \quad (3.5)$$

In this equation, the force generated by the CE (F_{CE}) is the maximum isometric (constant length) force (F_{\max}) multiplied by activation (A), the force-length ($f_l(\cdot)$), and force-velocity ($f_v(\cdot)$), relationships of the CE. The activation A is a low-pass filtered version of the stimulation signal muscle $S(t)$ generated by the muscle reflexes we will detail in the next section. This filter, given by $A(t) = S - \tau \dot{A}(t)$ with time constant τ , represents the diffusion dynamics of calcium ions that activate binding sites in the muscle fibers.

The binding sites are where overlapping actin and myosin filaments attach and generate pulling force. The contractile element length of l_{opt} corresponds to maximum overlap between these filaments. Therefore, as the muscle length moves away from l_{opt} , its force production capacity decreases leading to the force-length relationship shown in fig. 3.3. We model the force-length relationship via a bell curve

$$f_l(l_{\text{CE}}) = \exp \left(\ln(0.05) \left| \frac{l_{\text{CE}} - l_{\text{opt}}}{w l_{\text{opt}}} \right|^3 \right). \quad (3.6)$$

The velocity-dependent filament attachment probabilities give rise to a force-velocity relationship shown in fig. 3.4. The following expression captures this relationship.

$$f_v(v_{\text{CE}}) = \begin{cases} \frac{v_{\max} - v_{\text{CE}}}{v_{\max} + K v_{\text{CE}}}, & \text{if } v_{\text{CE}} < 0 \\ N + (N - 1) \frac{v_{\max} + v_{\text{CE}}}{7.56 K v_{\text{CE}} - v_{\max}}, & \text{if } v_{\text{CE}} \geq 0 \end{cases} \quad (3.7)$$

In this expression, K is a shape parameter and N determines the force amplification when the contractile element is lengthening. The force-velocity relationship acts as a multiplicative damper causing the

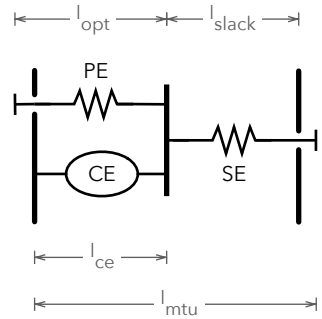


Figure 3.2: Hill-type muscle tendon unit with contractile element (CE), parallel elasticity (PE), and series elasticity (SE).

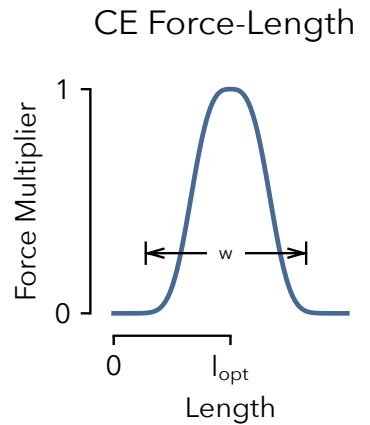


Figure 3.3: Force-length relationship of the CE.

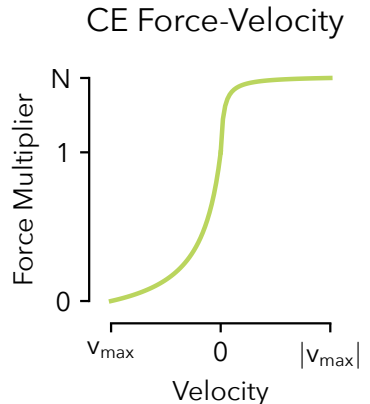


Figure 3.4: Force-velocity relationship of the CE.

Param	Value	Param	Value
τ	0.1 s	$l_{\text{opt}}^{\text{ham}}$	0.10 m
w	0.56	v_{\max}^{ham}	-1.2 m/s
K	5	F_{\max}^{ham}	3000 N
N	1.5	$l_{\text{slack}}^{\text{ham}}$	0.31 m
ϵ_{PE}	w		
ϵ_{SE}	0.04		

Table 3.3: Neuromuscular parameters for shared entities (left) and the hamstring muscle (right)

CE to produce more contractile force when it is lengthening and less as it contracts.

We model both passive elements, the PE and SE, using the same functional form representing a unidirectional, stiffening spring, the behavior of which is shown in fig. 3.5. The expressions for the elastic force produced by these elements are

$$F_{\text{PE}}(l_{\text{CE}}) = F_{\max} \left(\frac{l_{\text{CE}} - l_{\text{opt}}}{\epsilon_{\text{PE}} l_{\text{opt}}} \right)^2 (l_{\text{CE}} > l_{\text{opt}}) \quad (3.8)$$

$$F_{\text{SE}}(l_{\text{SE}}) = F_{\max} \left(\frac{l_{\text{SE}} - l_{\text{slack}}}{\epsilon_{\text{SE}} l_{\text{slack}}} \right)^2 (l_{\text{SE}} > l_{\text{slack}}). \quad (3.9)$$

The left-hand side of table 3.3 lists the parameters common among all seven muscles of each leg of the neuromuscular model. On the right-hand side of the table, we list four muscle-specific parameters for hamstrings muscle. For a complete list of muscle parameters please refer to Song and Geyer [2015].

The full biped model, shown in fig. 3.6, includes seven Hill-Type muscle-tendon units: soleus, gastrocnemius, tibialis anterior, vastus, hamstring, hip flexors, and gluteus. The length of these MTUs is related to the joint angles according to the variable-length moment arms $r_{\text{mtu}}^j(\phi^j)$ for each muscle about each joint. For example, the

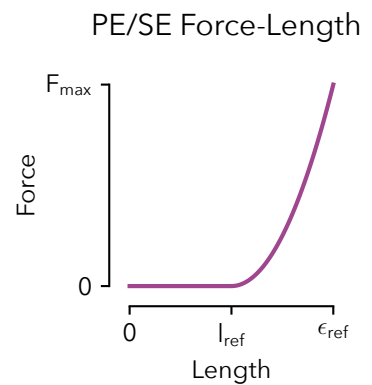


Figure 3.5: PE and SE force length relationship. For the PE, $l_{\text{ref}} = l_{\text{opt}}$ and $\epsilon_{\text{ref}} = \epsilon_{\text{PE}}$. Likewise, for the SE, $l_{\text{ref}} = l_{\text{slack}}$ and $\epsilon_{\text{ref}} = \epsilon_{\text{SE}}$.

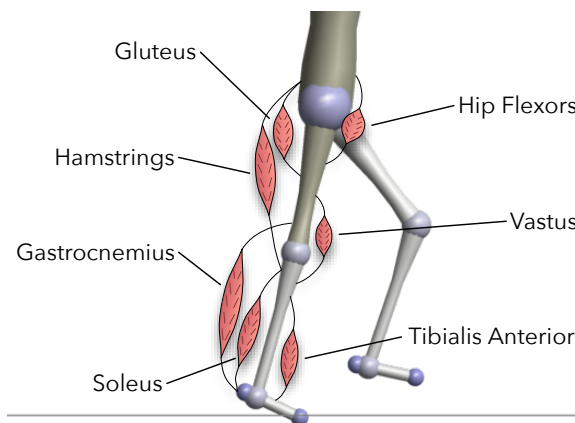


Figure 3.6: Biped walking model with labeled muscles.

length of a biarticular muscle spanning joints j and k is

$$l_{\text{mtu}} = l_{\text{opt}} + l_{\text{slack}} + \rho \left(\int_{\phi_0^j}^{\phi^j} r_{\text{mtu}}^j(\phi^j) d\phi^j + \int_{\phi_0^k}^{\phi^k} r_{\text{mtu}}^k(\phi^k) d\phi^k \right). \quad (3.10)$$

Where ρ is a parameter that approximates the effect of the pennation angle of the muscle fibers. The variable length moment arms also govern the torque a muscle produces about a joint according to

$$\tau_{\text{mtu}} = r_{\text{mtu}}^j(\phi^j) F_{\text{mtu}}. \quad (3.11)$$

3.3 Stance Reflexes

During stance, hypothesized reflex feedback pathways stimulate the muscles of the leg. In general, a linear feedback law governs the stimulation $S^m(t)$ of muscle m ,

$$S^m(t) = S_0^m + \sum_n G_n^m \text{Pro}_n(t - \Delta t_n), \quad (3.12)$$

where S_0^m is a constant pre-stimulation, $\text{Pro}_n(t - \Delta t_n)$ is the time-delayed proprioceptive signal from muscle n , and G_n^m is the gain on that signal. The proprioceptive signal can take the form of force feedback, $F_n^m(\cdot)$, which uses the time delayed tendon force, or length feedback, $L_n^m(\cdot) = l_{\text{CE},n}(\cdot) - l_{\text{off},n}$, which uses the difference between the length of the contractile element and an offset length l_n^{off} .

The time delay we apply to proprioceptive signals estimate the round-trip neural signal transmission delay of afferent signals from muscle spindles and Golgi tendons to the spine and efferent signals back to the muscles. For ankle muscles, the soleus, tibialis anterior, and gastrocnemius, the time delay is $\Delta t_n = 20$ ms. For knee muscles, the vastus and hamstrings, it is $\Delta t_n = 10$ ms. For the hip muscles, the hamstrings, gluteus, and hip flexors, the time delay is $\Delta t_n = 5$ ms. We will denote time delayed signals using $t_1 = t - 20$ ms, $t_m = t - 10$ ms, and $t_s = t - 5$ ms.

The reflexes encode several key functions of legged locomotion: generating compliant leg behavior, preventing knee overextension, and balancing the trunk.

The reflexes achieve the first function, generating compliant leg behavior, via positive force feedback on the monoarticular leg extensors: the soleus, vastus, and gluteus. For example, the reflexes stimulated the vastus in part by

$$S^{\text{vas}}(t) = S_0^{\text{vas}} + G_{\text{vas}}^{\text{vas}} F_{\text{vas}}(t_m) + \dots. \quad (3.13)$$

To implement the second function, preventing knee overextension, the reflex control uses two strategies. First, positive force feedback

of the biarticular gastrocnemius and hamstrings muscles helps counteract the tendency for knee overextension caused by ankle plantarflexion and hip extension torques, respectively. For example, the gastrocnemius has a force feedback reflex,

$$S^{\text{gas}}(t) = S_0^{\text{gas}} + G_{\text{gas}}^{\text{gas}} F_{\text{gas}}(t_l), \quad (3.14)$$

that flexes the knee as it contributes to ankle plantarflexion. The hamstring also has a positive force feed back

$$S^{\text{ham}}(t) = S_0^{\text{ham}} + G_{\text{ham}}^{\text{ham}} F_{\text{ham}}(t_s) + \dots \quad (3.15)$$

that counteracts knee extension caused by hip extension. Also, the hamstring force feedback helps prevent hip flexion caused by heel-strike.

A second mechanism further protects the knee by inhibiting the vastus stimulation in proportion to knee extension beyond a threshold, resulting in the complete vastus stimulation

$$\begin{aligned} S^{\text{vas}}(t) &= S_0^{\text{vas}} + G_{\text{vas}}^{\text{vas}} F_{\text{vas}}(t_m) - k_\phi (\phi_k(t_m) - \phi_k^{\text{off}}) \\ &\times (\phi_k(t_m) < \phi_k^{\text{off}}) (\dot{\phi}_k(t_m) < 0) \end{aligned} \quad (3.16)$$

where ϕ_k^{off} is the angle beyond which the vastus is inhibited.

The reflexes achieve the final function of balancing the trunk by proportional-derivative control that produces stimulations for the hip muscles (hip flexors, gluteus, and hamstrings) to stabilize the trunk at a reference lean. Because muscles can only provide pulling force, the proportional derivative control signal is distributed as hip flexor stimulation if the signal represents flexion torque and as simultaneous stimulation for the gluteus and hamstrings if it represents hip extension torque. For example, the complete hamstrings stimulation becomes

$$\begin{aligned} S^{\text{ham}}(t) &= S_0^{\text{ham}} + G_{\text{ham}}^{\text{ham}} F_{\text{ham}}(t_s) \\ &+ \left\{ k_p^{\text{ham}} (\phi_{\text{trunk}}(t_s) - \phi_{\text{ref}}) + k_d^{\text{ham}} \dot{\phi}_{\text{trunk}}(t_s) \right\}_+ \end{aligned} \quad (3.17)$$

where the third term returns the positive reflex contribution from the trunk balance control.

The full set of stance reflexes are:

$$S^{\text{sol}}(t) = S_0^{\text{sol}} + G_{\text{sol}}^{\text{sol}} F_{\text{sol}}(t_1) \quad (3.18)$$

$$S^{\text{ta}}(t) = S_0^{\text{ta}} + G_{\text{ta}}^{\text{ta}} L_{\text{ta}}(t_1) - G_{\text{sol}}^{\text{ta}} F_{\text{sol}}(t_1) \quad (3.19)$$

$$S^{\text{gas}}(t) = S_0^{\text{gas}} + G_{\text{gas}}^{\text{gas}} F_{\text{gas}}(t_1) \quad (3.20)$$

$$S^{\text{vas}}(t) = S_0^{\text{vas}} + G_{\text{vas}}^{\text{vas}} F_{\text{vas}}(t_m) - k_\phi (\phi_k(t_m) - \phi_k^{\text{off}}) (\phi_k(t_m) < \phi_k^{\text{off}}) (\dot{\phi}_k(t_m) < 0) \quad (3.21)$$

$$S^{\text{ham}}(t) = S_0^{\text{ham}} + G_{\text{ham}}^{\text{ham}} F_{\text{ham}}(t_s) + \left\{ k_p^{\text{ham}} (\phi_{\text{trunk}} - \phi_{\text{ref}}) + k_d^{\text{ham}} \dot{\phi}_{\text{trunk}} \right\}_+ \quad (3.22)$$

$$S^{\text{glu}}(t) = S_0^{\text{glu}} + G_{\text{glu}}^{\text{glu}} F_{\text{glu}}(t_s) + \left\{ k_p^{\text{glu}} (\phi_{\text{trunk}} - \phi_{\text{ref}}) + k_d^{\text{glu}} \dot{\phi}_{\text{trunk}} \right\}_- \quad (3.23)$$

$$S^{\text{hfl}}(t) = S_0^{\text{hfl}} + \left\{ k_p^{\text{hfl}} (\phi_{\text{trunk}} - \phi_{\text{ref}}) + k_d^{\text{hfl}} \dot{\phi}_{\text{trunk}} \right\}_+ \quad (3.24)$$

3.4 Swing Leg Control

During swing, the reflexes shape the natural double pendulum dynamics of the leg in order to achieve sufficient knee flexion, prevent toe scuffing, reach a target landing leg angle, and then extend the leg towards the ground. We here review two versions of the swing leg control: First, an idealized control, proposed in Desai and Geyer [2012], which proposes reflexes that directly applies torques to the hip and knee joints (section 3.4.1), and second, a muscle reflex control, presented in Desai and Geyer [2013], which applies neural stimulations to Hill-type muscles to achieve the functionality of the idealized control (section 3.4.2).

3.4.1 Idealized Swing Leg Control

The idealized swing control comprises two layers. In the first layer, a leg placement policy,

$$\alpha_{\text{tgt}} = \alpha_0 + c_d d + c_v v, \quad (3.25)$$

prescribes leg angle for the leg to reach by the end of swing. We measure the leg angle between the hip-ankle line and horizontal as shown in fig. 3.7. In eq. (3.25), α_{tgt} is the target leg angle, α_0 is the default leg angle, d is the horizontal distance between the stance leg ankle and the model's center of mass, v is the velocity of the center of mass, and c_d and c_v are constant gain parameters. This policy is taken from Yin et al. [2007] and represents an empirical generalization of the leg placement strategies that recover the linear inverted pendulum model of human walking from disturbances [Kajita et al., 2001, Pratt et al., 2006].

The target angle generated by this policy forms a central input to the second layer comprised of hip and knee controls. The portion of this control that governs the knee action uses a finite state

machine to switch between three phases. The first phase allows the knee to passively flex in response to hip moments generated at the onset of swing. If the passive knee flexion is insufficient (the foot swings forward with a tendency to scuff the ground), the control produces active flexion torque of the knee in proportion to the rate $\dot{\alpha}$ of forward leg motion,

$$\tau_k^i = \begin{cases} 0, & \dot{\alpha} > 0 \\ -k^i \dot{\alpha}, & \dot{\alpha} \leq 0 \end{cases}, \quad (3.26)$$

where k^i is the flexion gain and the leg angle α is defined as the angle between the horizontal and the hip-ankle line.

The second phase activates when the leg length, defined as the distance between the hip and ankle, contracts below a threshold. In this phase, the knee torque is given by

$$\tau_k^{ii} = \begin{cases} -k_1^{ii} \dot{\phi}_k, & \dot{\phi}_k \geq 0 \\ -k_2^{ii} \dot{\phi}_k (\alpha - \alpha_{tgt}) (\dot{\alpha} - \dot{\phi}_k), & \dot{\phi}_k < 0 \text{ \& } \dot{\phi}_k < \dot{\alpha}, \\ 0, & \text{otherwise} \end{cases}, \quad (3.27)$$

where k_1^{ii} and k_2^{ii} are damping coefficients. The first case dampens knee flexion, while the second case dampens knee extension, but allows progressively more extension as the leg angle approaches its target. The modulation term $(\dot{\alpha} - \dot{\phi}_k)$ prevents premature landing of the leg by damping the knee if it extends faster than the overall leg angle.

The third phase engages when the leg angle gets within a threshold of the target leg angle. The control then applies torque to stop and extend the knee,

$$\tau_k^{iii} = \begin{cases} k^{iii} (\alpha_{thr} - \alpha) \left(1 - \frac{\dot{\alpha}}{\dot{\alpha}_{max}}\right), & \alpha < \alpha_{thr} \text{ \& } \dot{\alpha} < \dot{\alpha}_{max} \\ 0, & \text{otherwise} \end{cases}, \quad (3.28)$$

where $\dot{\alpha}_{max}$ is the maximum leg retraction velocity for which the stopping knee torque is applied. When this torque brings the leg velocity to zero, a knee extension torque is added,

$$\tau_k^{iii'} = \tau_k^{iii} - k^{ext} (l_0 - l), \quad (3.29)$$

where l_0 is the rest leg length, l is the current leg length, and k^{ext} is a proportional gain.

The swing leg control also specifies a hip torque in the form of a proportional derivative control on the leg angle,

$$\tau_h^\alpha = k_p (\alpha - \alpha_{tgt}) + k_d \dot{\alpha}. \quad (3.30)$$

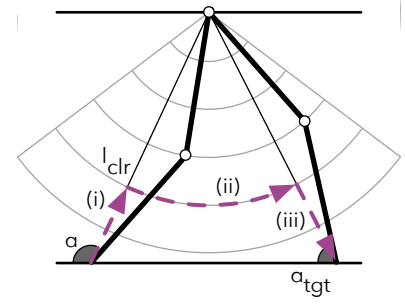


Figure 3.7: The swing leg control guides the leg towards a desired landing leg angle α_{tgt} through three phases: (i) Flex the knee until it achieves a clearance leg length l_{clr} . (ii) Hold the leg length via knee damping. (iii) Stop and Extend the leg towards the ground when the leg reaches α_{tgt} . Figure reproduced from Desai and Geyer [2012].

This hip torque is supplemented by a feed forward term

$$\tau_h = \tau_h^\alpha - 2\tau_k^{\text{iii}} \quad (3.31)$$

that neutralizes the coupling dynamics between the knee and hip during the knee's stop and extend phase (Eq. 3.28).

The torques produced by the swing controller augment the net torques produced by the Hill-type muscles and reflexes during stance. At heel strike, the control policy switches from using the swing leg control torques to the stance torques generated by the muscle models. In late stance, the policy mixes the torques specified by the stance and swing controllers by scaling the stance and swing torques and muscle stimulations in proportion to the normalized ground reaction force,

$$\tau_{\text{late stance}} = \tau_{\text{stance}}(\text{GRF}) + \tau_{\text{swing}}(1 - \text{GRF}), \quad (3.32)$$

$$S_{\text{late stance}}^m = S^m(\text{GRF}). \quad (3.33)$$

During swing, only the swing leg torques are used.

3.4.2 Neuromuscular Reflex Swing Leg Control

The muscle reflex interpretation of the idealized swing leg control presented in the previous oposes reflexes to achieve the same three goals as the ideal swing leg control: (i) flex the knee to achieve sufficient ground clearance, (ii) prevent toe scuffing by damping the knee (iii) stop and extend the leg when the target leg angle is achieved (see fig. 3.7). This control assumes a leg with nine-muscles, the seven included in the stance control (fig. 3.6), as well as two additional muscles shown in figure (fig. 3.8). These muscles are a monoarticular knee flexor, the biceps femoris short head, and a biarticular hip flexor/knee extensor, the rectus femoris. As in the case of the stance control, the reflexes primarily consist of linear feedback laws of the form

$$S_{\text{phase}}^m(t) = G_n^m \text{Pro}_n(t - \Delta t_n). \quad (3.34)$$

For the swing control, the proprioceptive feedback can be either on length, $L_n^m(\cdot) = l_{\text{CE},n}(\cdot) - l_{\text{off},n}$, or velocity, $V_n^m(\cdot) = v_{\text{CE},n}(\cdot) - v_{\text{off},n}$. In these equations $l_{\text{off},n}$ and $v_{\text{off},n}$ are offset lengths and velocities the control tries to obtain.

As in the idealized control, the knee control is divided into three phases. In phase 1, the behavior of the idealized control is to provide knee flexion torque in proportion to the rate of forward leg angle progression (eq. (3.26)). The muscle interpretation uses the rate of length change of the rectus femoris contractile element as a proxy

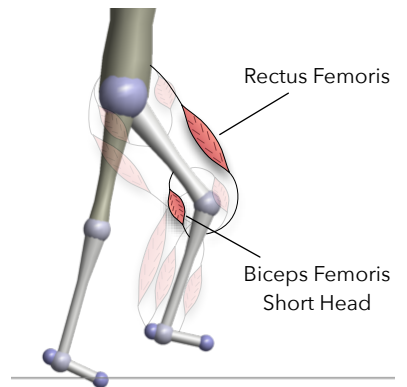


Figure 3.8: Neuromuscular Swing leg control employs the seven muscles used in the stance control as well as a monoarticular knee flexor, the biceps femoris short head, and a biarticular hip flexor/knee extensor, the rectus femoris

for the speed of the leg angle. It therefore implements phase 1 by stimulating a monoarticular knee flexor, the biceps femoris short head, based on velocity feedback from the rectus femoris.

$$S_i^{\text{bfsh}}(t) = G_{\text{rf}}^{\text{bfsh}} V_{\text{rf}}(t_m). \quad (3.35)$$

In the second phase, the control dampens knee flexion and modulates the damping of knee extension (eq. (3.27), allowing more extension as the target angle is approached and only damping the knee if it extends faster than the leg angle progresses. In this phase, the control uses velocity feedback to dampen knee flexion according to

$$S_{ii}^{\text{rf}}(t) = G_{\text{bfsh}}^{\text{bfsh}} V_{\text{bfsh}}(t_m), \quad (3.36)$$

and a modified velocity feedback to dampen knee extension according to

$$S_{ii}^{\text{bfsh}}(t) = G_{\text{bfsh}}^{\text{bfsh}} V_{\text{bfsh}}(t_m) L_{\text{rf}}^{\text{bfsh}}(t_m) (V_{\text{bfsh}}(t_m) + V_{\text{rf}}(t_m)). \quad (3.37)$$

The final task of the swing control, is to stop and extend the leg. Stopping is achieved by length feedback on the hamstring

$$S_{iii}^{\text{ham}}(t) = G_{\text{ham}}^{\text{ham}} L_{\text{ham}}(t_s), \quad (3.38)$$

and is augmented by the other knee flexors if $S_{iii}^{\text{ham}}(t) > S_{\text{thr}}$, where S_{thr} is a threshold.

$$S_{iii}^{\text{bfsh}}(t) = G_{\text{bfsh}}^{\text{ham}} (S_{iii}^{\text{ham}}(t) - S_{\text{thr}}) \quad (3.39)$$

$$S_{iii}^{\text{gas}}(t) = G_{\text{gas}}^{\text{ham}} (S_{iii}^{\text{ham}}(t) - S_{\text{thr}}) \quad (3.40)$$

The control triggers knee extension through vastus length feedback, when the leg angle velocity crosses zero,

$$S_{iii}^{\text{vas}}(t) = G_{\text{vas}}^{\text{vas}} L_{\text{vas}}(t_s). \quad (3.41)$$

The hip and ankle joints are controlled via length feedbacks. The hip control approximates α through the length of the rectus femoris. Consequently, the hip control uses length feedback from the rectus femoris in order to drive the leg towards α_{tgt} ,

$$S^{\text{hfl}}(t) = S_0^{\text{hfl}} + G_{\text{rf}}^{\text{hfl}} L_{\text{rf}}(t_s) \quad (3.42)$$

$$S^{\text{glu}}(t) = S_0^{\text{glu}} + G_{\text{rf}}^{\text{glu}} L_{\text{rf}}(t_s). \quad (3.43)$$

During swing length feedback on the tibialis anterior dorsiflexes the ankle to prevent toe scuffing

$$S^{\text{ta}}(t) = S_0^{\text{ta}} + G_{\text{ta}}^{\text{ta}} L_{\text{ta}}(t_1) \quad (3.44)$$

4

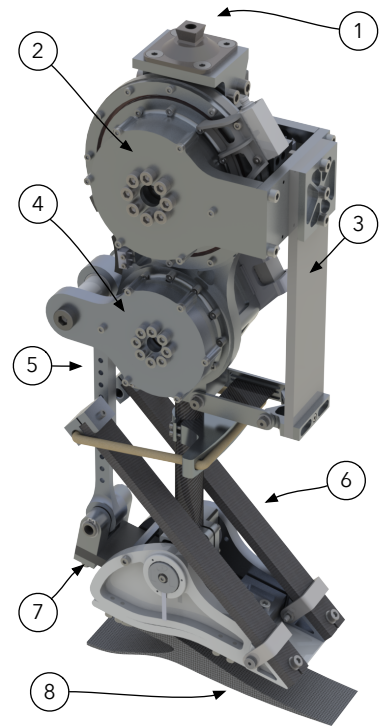
Completed Work

4.1 Transfemoral Prosthesis Design

To test our proposed Neuromuscular control approach, and its ability to help subjects maintain or recover their balance, we build a custom transemoral prosthesis capable of reproducing dynamic locomotion tasks. The proposed design, shown in fig. 4.1, uses brushless electric motors coupled to harmonic drive gear sets to drive both the knee and ankle joints. Additionally, the joints employ series elastic actuation to enable accurate torque control and to protect the Harmonic Drive gear sets from sudden impacts. The design also features a unidirectional parallel spring in the ankle that partly offsets the torque demands on the ankle motor. We design both joints to meet the demands of dynamic locomotion tasks such as running and trip recovery.

The overall design concept sits in a niche between low powered prostheses designed with commercial applicability in mind [Sup et al., 2007, 2009, Lawson et al., 2014, Rouse et al., 2015, Martinez-Villalpando et al., 2011] which feature onboard actuation and power sources, and high-powered tethered systems [Caputo and Collins, 2013, Caputo et al., 2015] with off board actuation designed exclusively for use in lab environment. Our design features onboard actuators that are more powerful than those used in standalone devices, but less capable than those employed in tethered devices. To ensure a reasonable overall weight the device's batteries, motor drivers, and computers are off board. With this design, we expect to be able to test control ideas without encountering hardware performance limitations as with a tethered device. At the same time the device is capable of functioning outside of the lab environment like a standalone prosthesis.

Table 4.1 shows the desired design specifications for the transfemoral prosthesis and the values achieved by the final design. To obtain these design specifications we examined a number of studies



- 1) Pyramid Adaptor
- 2) Knee Motor
- 3) Knee Series Spring
- 4) Ankle Motor
- 5) Adjustable Height
- 6) Unidirectional Parallel Spring
- 7) Ankle Series Spring
- 8) Composite Foot

Figure 4.1: Render of proposed powered knee and ankle prosthesis design. The prosthesis includes series elastic actuators to enable accurate torque control and a unidirectional parallel ankle spring to offset the required angle torque.

Specification	Desired Value	Achieved Value
Maximum Knee Torque	160 N · m	170 N · m
Maximum Knee Speed	1.80 rev/s	1.93 rev/sec
Maximum Ankle Torque	200 N · m	170 (+120*) N · m
Maximum Ankle Speed	1.14 rev/s	1.22 rev/s
Weight	6.8 kg	5.9 kg
Minimum Height	42.5 cm	42 cm

Table 4.1: Designed and achieved design specifications. (*Maximum total ankle torque is 290 N · m achieved at 10 degrees of dorsiflexion.)

that elicited trip responses.

We specify desired joint torque and speed values to meet the requirements of demanding tasks such as running. The maximum knee torque specification comes from the findings of Whitley [2008], who tested the joint torques used during recovery from a simulated fall. The maximum knee speed requirement comes from Grabiner et al. [1993], who tested subjects' responses to simulated trips induced by unseen obstacles on a walkway. We obtain the maximum ankle torque requirement from Pijnappels et al. [2005], who tripped subjects using obstacles that could suddenly emerge through the floor. The maximum ankle speed requirement comes from the running data of Novacheck [1998]. We set to the minimum height specification, measured between the center of the knee and bottom of the foot, to accommodate the 10th percentile female [Gordon et al., 1989]. Finally, the required weight corresponds to the mean leg weight of a 50th percentile male [Winter, 2009].

4.1.1 Knee Joint

In addition to achieving the maximum speeds and torques found in table 4.1, we design the knee joint so that it can reproduce the torque and speed required for a 80 kg person to run at 3.2 m/s as measured by Novacheck [1998]. To reproduce this trajectory in the knee joint, we utilize a RoboDrive ILM 85 × 13 HS-SP motor coupled to a Harmonic Drive Gear set with a 50:1 reduction (CSG-25-50). Figure 4.2 shows the motor torque and speed required to reproduce a running trajectory assuming a gear efficiency of 75%. In this plot, we see that the running trajectory lies within the speed-dependent torque limit of the motor. Moreover, the root mean squared torque of this trajectory (1.46 N · m) exceeds the torque rating of the motor (1.43 N · m) by just 2%. Therefore, the knee joint should be able to provide the necessary torque to enable running for a short amount of time, or continuously for lighter subjects or at a slightly reduced speed.

Figure 4.3 shows the internal and external design of the knee joint. The primary component in the knee joint is the stator housing. On

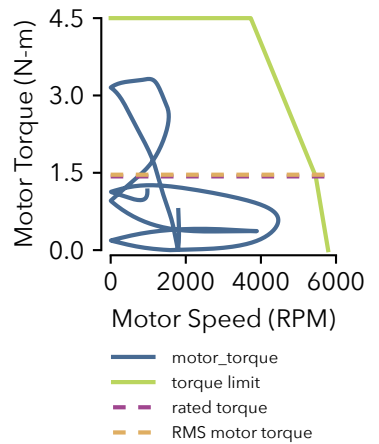
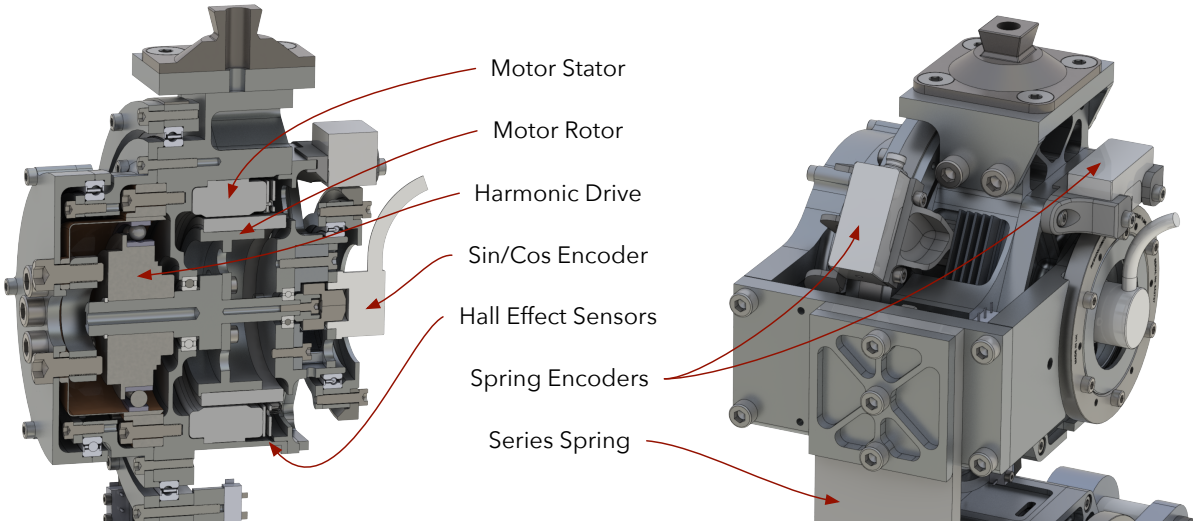


Figure 4.2: Knee motor torque required for running



top of the housing is a standard pyramid adaptor that allows the prosthesis to connect to amputee's sockets. Within the stator housing, lies the brushless motor stator, rotor, and harmonic drive gear set.

We sense absolute rotor angle for commutation of the brushless motor via hall effect sensors and a magnetic complementary sin/cos encoder. To incorporate series elasticity, we take inspiration from the design of the bipedal robot Atrias [Grimes, 2013], which uses fiberglass series leaf springs. In our design, the output of the gear set drives the proximal end of a fiberglass leaf spring in series with the shank. Two Renishaw Resolute absolute encoders measure the deflection of this spring to enable torque control.

In addition to allowing for accurate torque control, as shown by Au et al. [2007], Au and Herr [2008], the series elasticity also plays a crucial role in protecting fragile gear components from impact loads. To choose the spring stiffness for the knee joint, we simulate the prosthesis impacting a rigid wall with the foot during swing. To do this, we construct a model of the prosthesis in Matlab Simulink Simulink Simscape Multibody that includes the series elasticity, gear dynamics, and motor electrical dynamics (for details see ??). ?? shows the simulation environment. The prosthesis is attached to the distal end of a thigh segment with a fixed hip position. We control the hip via the ideal swing leg control outlined in section 3.4.1 (eq. (3.30)) and consider the case where the external voltage applied to the motor is zero. This simulation suggests that a spring stiffness under $2300 \text{ N}\cdot\text{m}/\text{rad}$ will ensure that the peak impact torque remains lower than the peak allowable impact torque of the Harmonic Drive of $242 \text{ N}\cdot\text{m}$.

Figure 4.3: Internal and external design of the knee joint.

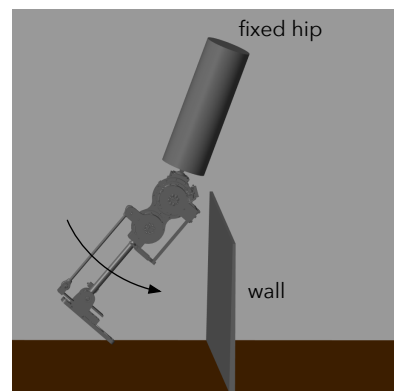


Figure 4.4: Impact simulation we used to determine appropriate series spring stiffness.

4.1.2 Ankle Joint

In the ankle joint we utilize a RoboDrive ILM 70×10 HS-SP motor coupled to a Harmonic Drive Gear set with a 100:1 reduction (CSG-20–100). As with the knee joint, we design the ankle joint to satisfy the requirements listed in table 4.1. Specifically, for the ankle joint we pay considerable attention to the tripping condition described by Pijnappels et al. [2005], in which the ankle generates a peak torque of 202 N · m.

To avoid using a large and heavy motor to achieve this peak torque, we take inspiration from previous prosthetic ankle designs that employ a unidirectional parallel spring in the ankle joint that performs the conservative portion of the ankle’s torque versus angle trajectory during normal walking [Au et al., 2007, Au and Herr, 2008, Sup et al., 2009, Lawson et al., 2014]. The parallel spring offsets the required motor torque, as the actuator only needs to provide the difference between the desired torque and the torque provided by the parallel spring. Figure 4.5 shows the torque versus angle curve during level ground walking (Winter [2009], scaled to 80 kg person). In green we show the torque generated by a 700 N·m/rad parallel spring optimized to minimize the root-mean-squared motor torque for this trajectory. From this plot, we see that with the parallel spring, the peak torque is lower than the repeated peak torque limit of the Harmonic Drive Gear set.

The tripping data obtained by Pijnappels et al. [2005] shows that the ankle kinematics during trip recovery are similar to those seen during normal walking. Therefore, the parallel spring, should be able to contribute torque during the tripping case as well. To confirm this, fig. 4.6 shows the motor torque required for trip recovery (obtained by scaling walking torque data from Winter [2009] to have a peak torque of 202 N · m) We see that the inclusion of the parallel spring allows the prosthesis to produce enough net torque to reproduce

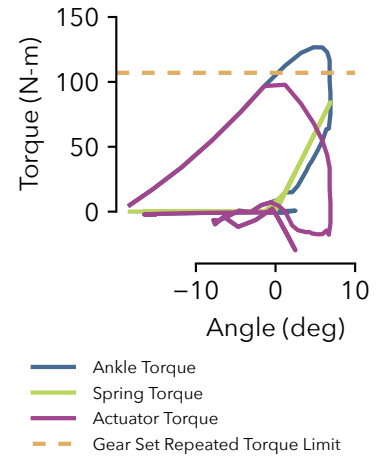


Figure 4.5: Ankle torque vs angle curve during steady, level-ground walking (blue) (Winter [2009] scaled to 80 kg person). A unidirectional parallel spring can provide a portion of this torque (green) and reduces the required actuator torque (purple) to lie under repeated torque limit of the Harmonic Drive Gear set (orange).

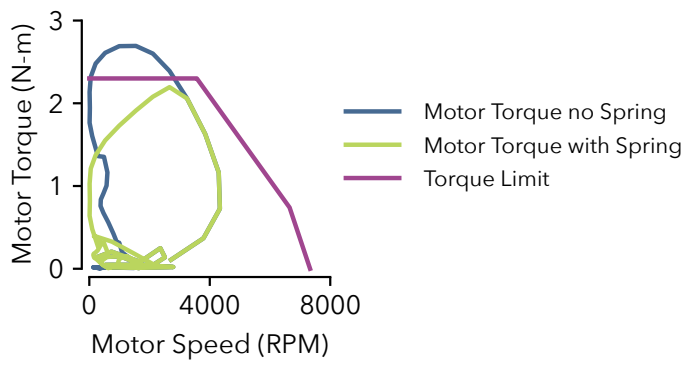


Figure 4.6: Ankle motor torque required to take the trip recovery action observed by Pijnappels et al. [2005] (blue, trajectory obtained by scaling walking data from Winter [2009] to a peak torque of 202 N · m, 75% gear efficiency assumed). Using a parallel spring allows the motor to produce the required torque (green) while remaining within its torque limit (purple).

the trip recovery trajectory without exceeding the torque limit of the motor.

Finally, fig. 4.7 shows the torque and speed required of the motor for running [Novacheck, 1998]. In this case, we use an ankle parallel stiffness of $267 \text{ N}\cdot\text{m}/\text{rad}$. From this plot, we see that this combination of ankle motor and spring is nearly sufficient for running. Increasing the voltage of the prosthesis from 48 V to 60 V or decreasing the gear ratio from 100:1 to 80:1 will allow the torque trajectory to fit completely within the motor limits.

Figure 4.8 shows an internal view of the ankle actuator and external views of the actuator and foot mechanism. In the ankle design, the output of the actuator actuates the foot through a four-bar mechanism. The actuator pulls or pushes on the proximal end of a length-adjustable tendon. The distal end of the tendon attaches to one end of a fiberglass series elastic leaf spring that is also connected to the foot. By measuring the angles of the ankle actuator output and the ankle joint and using the equations of the four-bar mechanism's kinematics, we can calculate the deflection of the leaf spring and thus the torque applied to the ankle.

The design of the ankle actuator represents a second iteration of the knee actuator design and features two main improvements. First, it has increased space on the side of the motor for cable routing. Second, the ankle actuator has a solid rotor shaft. In contrast, the knee actuator's shaft is comprised of two parts: one that held the motor rotor and transferred power through the gear set, and another that held the sin/cos encoder's magnetic shaft component. In practice,

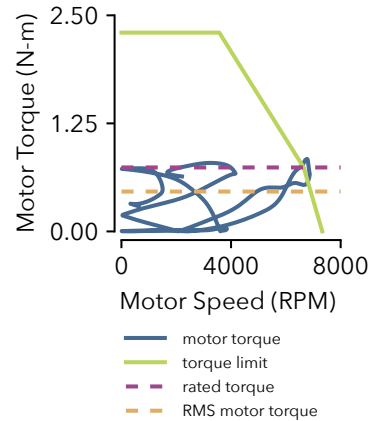


Figure 4.7: Ankle motor torque required to reproduce the running trajectory recorded by Novacheck [1998] assuming a parallel spring stiffness of $267 \text{ N}\cdot\text{m}/\text{rad}$ and a gear efficiency of 75%.

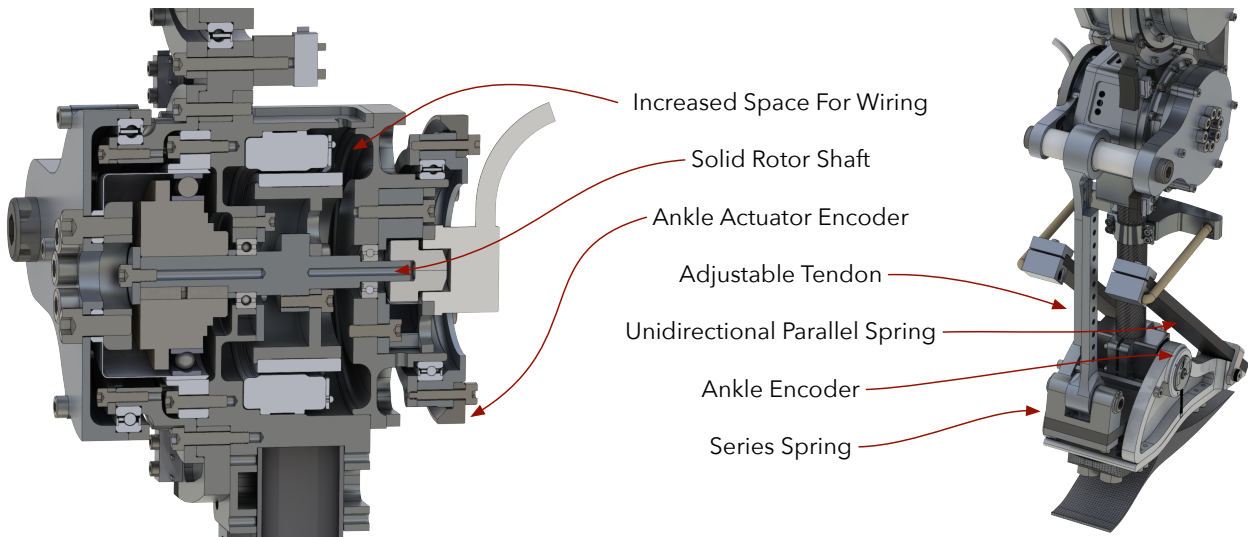


Figure 4.8: Internal and external design of the ankle joint.

these two components proved difficult to align, causing degraded performance of the sin/cos encoder. The ankle actuator's solid shaft ensures the encoder magnet stays aligned with the read head.

As with did for the knee series spring, we again determine an acceptable ankle spring stiffness by performing an impact simulation. For the ankle, we simulate an 80 kg person stepping on the prosthesis when the motor driver provides the ankle motor with zero applied voltage. Figure 4.9 shows the simulation environment. From this simulation we find that a spring stiffness of about $1000 \text{ N}\cdot\text{m}/\text{rad}$ should sufficiently protect the ankle gear set from impacts. This estimate is likely softer than necessary due to the additional series compliance in the amputee's socket and the composite foot that are not included in the simulation.

4.1.3 Experiments on Powered Knee/Passive Ankle Prosthetic

Towards a full realization and study on amputee subjects, we present a partial implementation and evaluation of the control on the current prosthesis prototype worn by a non-amputee user. Figure 4.10 shows an able-bodied user wearing our current prosthesis prototype. The current prosthesis prototype has an active knee SEA unit and an unpowered, spring-loaded, ankle. We connect the prosthesis to a knee crutch (iWalk 2.0 Hands Free Crutch) in order to allow a non-amputee experimenter to test the control. Additionally, the experimenter wears a lift shoe to compensate for the added thigh length of the knee crutch and prosthesis.



Figure 4.9: Impact simulation we used to determine appropriate series spring stiffness.

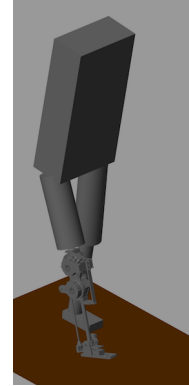


Figure 4.10: A non-amputee experimenter tests the prosthesis using an iWalk Crutch as a knee adaptor. The experimenter wears a lift shoe on the contralateral leg to compensate for the added thigh length of the prosthesis and knee adaptor.

To control the prosthesis knee, we use Simulink Real-Time (Math-

works, USA), which samples all sensors (joint encoders, IMU on thigh, force sensors in foot), runs a velocity-based SEA control [Schepelmann et al., 2012], and sends commands to the motor controller at a rate of 1kHz. Given a desired torque, τ_d , and a measured torque error, τ_e , the commanded motor velocity is given by

$$\omega_m = \frac{1}{k} \frac{d\tau_d}{dt} + \omega_l + PD(\tau_e), \quad (4.1)$$

where ω_l is the velocity of the load-side of the series spring (the shank) and $PD(\cdot)$ is a proportional-derivative feedback term.

The behavior control of the knee is a hybrid model that combines the Neuromuscular Stance control described in section 3.3 with the idealized swing control outlined in section 3.4.1. The missing ankle actuation in the current prosthesis prototype restricts the neuromuscular stance control to those muscles that span the knee: the vastus, hamstring, and gastrocnemius. The hamstring and vastus are stimulated according to eqs. (3.21) and (3.22) respectively. Similarly, the gastrocnemius is stimulated by positive force feedback. (The torso balance contribution of the complete hamstring stimulation, eq. (3.22), is neglected.) The realtime software executes the hybrid neuromuscular behavior control at a rate of 5kHz, ensuring that the integration (ode1) of the simulated muscle dynamics remains stable. During swing, we only use the knee portion of the swing control given by eqs. (3.26) to (3.29). In late swing, the control transitions between the two phases in proportion to the measured ground reaction force (eqs. (3.32) and (3.33)).

4.1.4 Slow Walking Behavior

We first test if the prosthesis control can reproduce normal stance and swing behavior of the lower limb in steady-state walking. For this purpose, we capture joint kinematics and kinetics as well as the virtual muscle activations of the prosthesis control while an experimenter walks for ten trials with the crutch and prosthesis system on a treadmill. Because the fit of the crutch to the experimenter's leg is not very tight, we limit the walking speed to 0.5 m/s and the experimenter holds onto handrails for safety (fig. 4.10).

The control generates steady-state prosthesis behavior that qualitatively reproduces human leg behavior in walking. Figure 4.11 compares the observed prosthesis leg behavior (solid lines) to corresponding human data at preferred walking speed (dashed lines, adapted from Winter [2009], Perry and Burnfield [2010]). The hip and knee kinematics match overall, although later transitions from stance to swing are observed in both joints (θ_h and θ_k) and the prosthesis knee flexes less in stance (θ_k). The knee torque follows trends similar

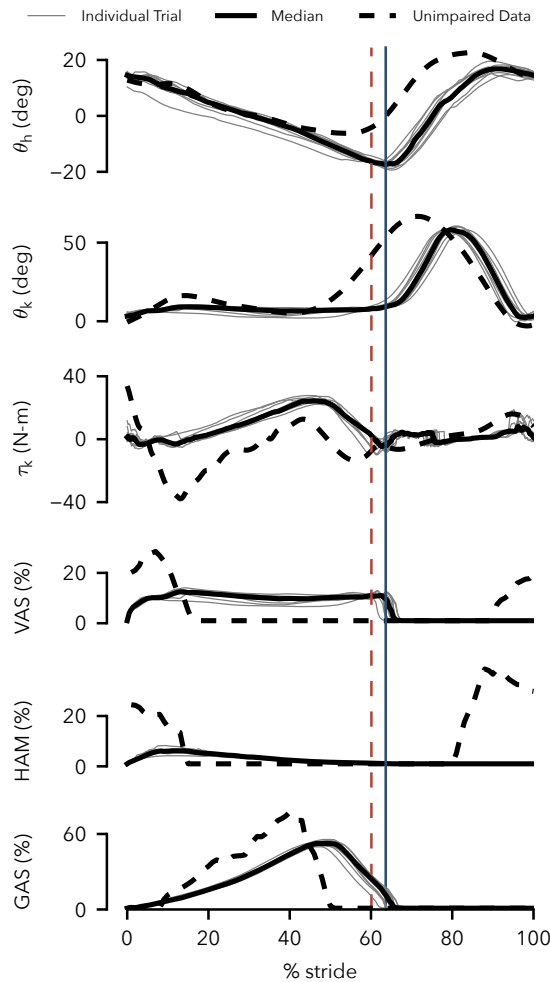


Figure 4.11: Prosthetic behavior at walking speed of 0.5 m/s. Shown are the hip and knee trajectories, the knee controller torque, and the activations of the vastus, hamstring, and gastrocnemius muscles generated by the prosthesis control in the testbed. Solid black lines show averaged data of ten trials with the individual trials depicted in gray. Dashed lines show corresponding data from human walking at preferred speed (joint angles and knee torque: Winter [2009], muscle surface electromyograms: Perry and Burnfield [2010]). Solid and dashed vertical lines indicate median toe off times for the prosthesis and human data respectively.

to human data, but the peak flexion and extension torques in the early stance phase are diminished (τ_k). These lower peaks are caused by reduced activations of the virtual vastus and hamstring muscles (VAS and HAM) in this phase, a clear difference to these muscles' activation in humans, in which bursts of activity at heel strike are followed by relative silence. Finally, the activity of the virtual gastrocnemius muscle (GAS) bears strong similarity the activity of this muscle in human walking.

To some extent, limitations of our current experimental testbed may account for observed discrepancies. The imposed slow walking speed of 0.5 m/s required less energy absorption in early stance than at normal walking speed. Moreover, the experimenter held onto the handrails to assist with lateral balance, which may have channeled some impact energy through the arms. In addition, the hybrid nature of the proposed control prevents the virtual muscles

from activating in swing, which is the case in humans (fig. 4.11, VAS and HAM activities from 80% to 100% of gait cycle), and would alter the response of the virtual muscles at heel strike. Finally, the lack of an active ankle and its control in the current prosthesis prototype further limits how closely the leg behaviors can match.

4.1.5 Response to Swing Leg Tripping

In a second set of experiments, we evaluate the response of the prosthesis controller to trip disturbances. We apply disturbances during treadmill walking by commanding flexion knee torques to the prosthesis in addition to its swing-leg control torque. The added torque simulates an obstacle encounter modeled in the same way as the stopping torque of the swing leg control, eq. (3.28), with α_{thr} replaced by a disturbance leg angle. The foot can pass the simulated obstacle if the leg length contracts beyond a threshold of 94 cm. For an early-, mid-, or late-swing encounter, the disturbance angle is set to 110, 95, or 80 degrees, respectively. In addition, anticipation of the trip by the experimenter is prevented by applying the disturbance only with a probability of 25%.

The experiments reveal that in response to disturbances during early and late swing, the prosthesis control places the swing leg with high repeatability and produces leg elevating and lowering strategies observed in humans. fig. 4.12 shows the Cartesian ankle trajectory in swing over 10 trials for the undisturbed (A) and disturbed conditions (B-D). In the undisturbed condition, the leg placement is repeatable with an interquartile range (IQR) of landing positions of 3.1 cm and a bias of 2.7 cm (median) from the target (dashed line). (Further tuning of the control parameters should improve the landing position accuracy.)

In the early disturbance condition (fig. 4.12B), the prosthesis generates large knee flexion roughly doubling the peak ground clearance. Nonetheless, the median landing position remains within 5.3 cm of the target (IQR: 10.2 cm), demonstrating the knee control's ability to compensate for early swing disturbances. This response is similar to the leg elevating strategy observed in humans when disturbed shortly after toe-off [Eng et al., 1994, Schillings et al., 2000]. The biological strategy, however, shows active knee flexor muscle contributions, while the prosthesis knee flexion is entirely passive, as the leg angular velocity does not become negative during the disturbance (Eq. 3.26, section 3.4.1).

In the late disturbance condition fig. 4.12D), the prosthesis leg behavior resembles the lowering strategy of humans [Schillings et al., 2000], in which knee extensor muscles quickly extend the leg. This

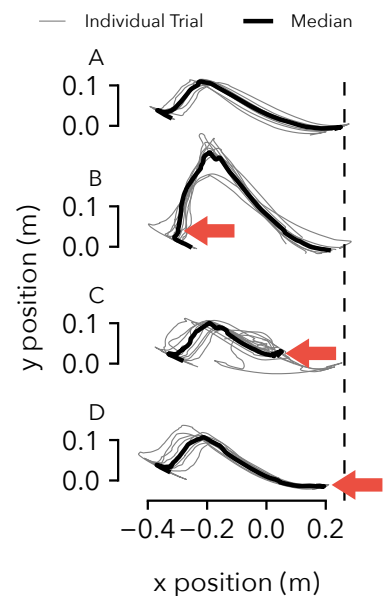


Figure 4.12: Response to simulated tripping disturbance. (A) Undisturbed ankle trajectory calculated from hip and knee angles assuming constant hip height. (B-D) Ankle trajectories with disturbance applied in early, mid and late swing (arrows). The vertical dashed line shows the target landing position of the foot, which corresponds to a 75 degree landing angle.

behavior is triggered on the prosthesis in the third phase of the swing control before the leg angle starts to retract (eq. (3.29)). The prosthesis achieves ground contact slightly earlier with a median landing point of 8.8 cm before the target (IQR: 3 cm).

Finally, fig. 4.12C shows the response of the prosthesis to a mid-swing disturbance. When humans are confronted with disturbances in mid swing, they may use either elevating or lowering strategies [Eng et al., 1994, Schillings et al., 2000]. However, the prosthesis response resembles neither strategy. During mid swing, the prosthesis control uses a holding policy, damping both knee flexion and extension (eq. (3.27)). Consequently, in most cases the knee angle neither flexes adequately to clear the obstacle nor extends quickly enough to make timely ground contact. In these trials, falling was only prevented via support from the treadmill handrails.

4.2 Comparison of Robustness Achieved by Reflex and Impedance Controls in Simulation

To evaluate the potential of neuromuscular prosthesis control to improve amputee gait robustness, we construct a simulation of an amputee walking on a powered prosthesis and perform optimizations to identify parameters that lead to robust locomotion over rough terrain. We then compare the performance of the proposed control to that of impedance control and find that the proposed control improves robustness to elevation changes and unexpected deviations from nominal walking, suggesting that it may help amputees prevent trips and falls (fig. 4.13).

4.2.1 Simulation Environment

We study the performance of the proposed transfemoral prosthesis controller in a simulation model of a unilateral amputee equipped with the proposed powered prosthesis. To more accurately model an amputee's anatomy, we sever the femur of the unimpaired human model 11 cm above the knee and attach the hamstring muscle to the distal end of the shortened bone as recommended in Brown et al. [2012]. This change converts the biarticular hamstring into a monoarticular muscle that only extends the hip. Next, we attach a model of the full prosthesis to the severed femur. The prosthesis modeled in this study is an earlier version of the prosthesis design presented in section 4.1, which uses the knee actuator design for both the knee and ankle joints. Our simulation of the prosthesis models the series elasticity, electrical dynamics, gear ratios, and resultant reflected inertias of the actuators, and assumes a low-level current-

based SEA control achieves desired torques [Pratt and Williamson, 1995].

To generate the reference torques for the SEAs, we use a hybrid neuromuscular control that blends the muscle based stance-control (section 3.3) with the idealized swing leg placement control section 3.4. We make two modifications to the prosthesis-side swing leg control. First, on the prosthesis-side hip we remove the feed-forward term that neutralizes the disturbance created by the knee's stop and extend phase (eq. (3.31)), requiring that feedback control deal with this torque. Second, we do not use the adaptive leg placement policy of the swing control (eq. (3.25)) as the prosthesis does not have access to information about the amputee's center of mass and stance leg ankle position. Instead the prosthesis swing leg control employs a constant target leg angle, $\alpha_{tgt} = const.$

To compare the performance of the proposed control, we also simulate the commonly-used impedance control method, described in detail in section 2.1.3, at the behavior level. Specifically, we implement the impedance control presented in Sup et al. [2008] as it tended to perform better than other versions in our simulations. This control partitions the gait cycle into four phases. In each phase i , the torque of an actuated joint is governed by an impedance function

$$\tau_i = -k_{1,i}(\theta - \theta_{1,i}) - k_{2,i}(\theta - \theta_{2,i})^3 - b_i\dot{\theta}, \quad (4.2)$$

where θ is the joint angle, $\theta_{1,i}$ and $\theta_{2,i}$ are angle offsets, and $k_{1,i}$, $k_{2,i}$ and b_i are the impedance parameters.

4.2.2 Controller Optimization for Natural and Robust Walking

For both the hybrid neuromuscular controller and the impedance controller, we use optimization to search for gaits that appear natural and are robust to disturbances. For the hybrid neuromuscular model, we optimize 53 parameters that include reflex feedback gains and swing leg control parameters for both the amputee and prosthesis as well as the SEA control gains. To reduce the number of parameters to optimize, we use fixed values for many parameters, such as the muscle properties and prestimulations. For the impedance controller, we optimize 59 parameters that include the reflex feedback gains and the swing leg control parameters for the amputee model, and the impedance parameters and SEA controller gains for the prosthesis. Again to reduce the number of parameters to optimize, the impedance parameters that are set to zero according to Sup et al. [2008] are fixed to zero during the optimization.

We rely on the covariance matrix adaptation evolution strategy (CMA-ES) [Hansen, 2006] and perform optimization in two steps. In

the first step, we search for control parameters that generate a gait with natural kinematics and kinetics. To this end, we take advantage of the observation that human gait seems to result from minimizing metabolic energy consumption [McNeill Alexander, 2002], and use the cost of transport

$$\text{Cost} = \frac{W}{mgx} + \frac{1}{mgx} \int (c_1 \tau_{\text{cmd}}^2 + c_2 \tau_{\text{limit}}^2) dt \quad (4.3)$$

as optimization criterion. In the cost, W accounts for the energy consumption of both the modeled amputee's muscles and the prosthesis' virtual muscles according to Umberger et al. [2003], τ_{cmd} is the sum of the torques commanded by the neuromuscular swing control or the impedance control, τ_{limit} is the sum of torques produced by the model's mechanical hardstops, which prevent knee and ankle hyperextension, m is the mass of the amputee, g is the gravitational acceleration, and x is the distance travelled in 20 seconds. The hand tuned constants, $c_1 = 0.1$ and $c_2 = 0.01$, ensure that the terms of the cost function have similar order-of-magnitude.

We run the above optimization for 300 iterations, and use the best resulting set of control parameters to seed an optimization for robustness to unexpected changes in ground height. For this second step, the cost function becomes

$$\text{Cost} = -x + c_3 \int \tau_{\text{limit}}^2 dt, \quad (4.4)$$

rewarding the distance travelled and penalizing joint hyperextension ($c_3 = 0.0005$). Instead of level ground, the simulations evaluating the cost are performed on terrain that is flat for the first 10 meters (to allow the model to reach steady walking) and then features steps, spaced one meter apart and drawn from a uniform random distribution. The width of the distribution grows at a rate of 2.5 cm per meter distance travelled, resulting in steps that grow progressively rougher the farther the model walks. To avoid overfitting, the evaluation is performed on five different terrains, resulting in an average cost. Like in the first step, the optimization is stopped after 300 iterations, resulting in the final, best set of control parameters.

4.2.3 Results

We evaluate the performance of the proposed control and of impedance control by subjecting the amputee model to terrains that are flat for 10 meters and then feature steps drawn from uniform distributions for another 90 meters. The widths of the distributions are constant but vary among the terrains to test the control performance on steps of increasing steepness (0 cm to ± 14 cm, 2 cm increments, total of 8 terrains).

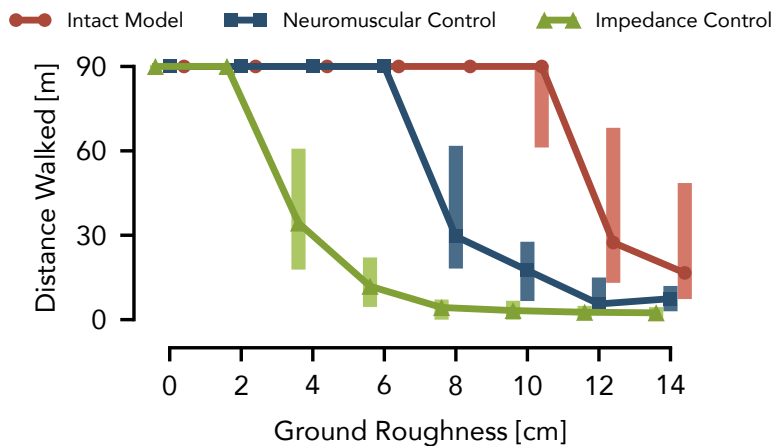
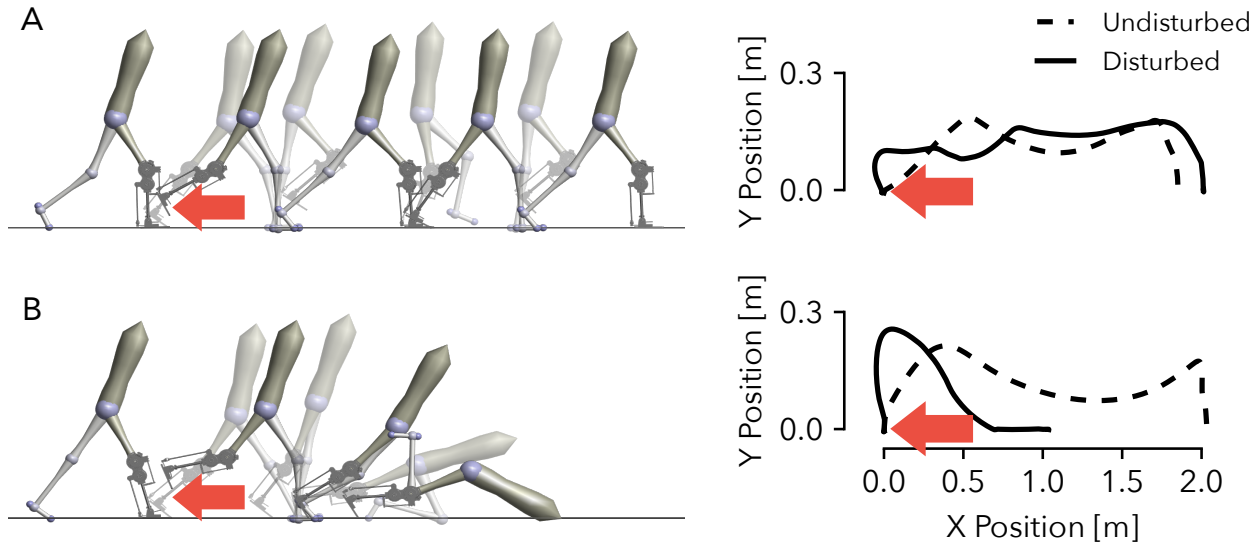


Figure 4.13 shows the distances the amputee model walks over 50 trials at each roughness level (proposed neuromuscular control in blue, impedance control in green). Most of the trials with the impedance-controlled prosthesis cover the full distance up to a roughness of 2 cm. At a roughness of 4 cm, however, the median distance drops to 34 m, which further declines as the roughness increases. In contrast, the prosthesis using the neuromuscular control, allows the amputee model to walk the full distance up to a roughness of 6 cm. Moreover, neuromuscular control has a similar distribution of distances walked at a roughness of 8 cm as impedance control has at a roughness of 4 cm.

Although the prosthesis using neuromuscular control significantly improves the robustness of the amputee model on rough terrain, the performance trails by a large margin that of an unimpaired model (fig. 4.13, red line), for which most of the trials covered the full distance up to a roughness of 10 cm. Limiting the swing leg placement targets in the neuromuscular prosthesis control to constant angles may account for some of this performance gap. In future work, we may overcome this limitation by estimating the amputee's center of mass velocity and stance ankle position so that the prosthesis control can take advantage of the full leg placement policy (eq. (3.25)). Other sources for the performance gap could stem from differences in the inertial properties between the prosthesis and the healthy leg, delay and inaccuracy in the series elastic actuator torque tracking, and the increased number of parameters in the asymmetric amputee model, which can reduce the quality of the optimized solutions.

A possible explanation for why the neuromuscular control produces more robust behavior than impedance control is the former's

Figure 4.13: Control performance of simulated prosthesis on rough terrain. The distances walked over terrains with different ground roughness are compared between the amputee model using a powered knee-ankle prosthesis with impedance control (green) and hybrid neuromuscular control (blue) as well as with the unimpaired human model (red). Shown are the median and range (25th and 75th percentiles) of the covered distances for 50 terrains sampled at each roughness level.



attempt to mimic the underlying dynamics and goals of human motor control rather than to track impedance behavior about a predefined motion for each individual joint. To illustrate this difference, we subject the amputee model with both control strategies to a simulated trip in the form of a $15\text{ N}\cdot\text{s}$ impulse applied at 5% of the undisturbed swing duration.

Figure 4.14A shows the toe trajectory of the prosthesis using neuromuscular control both in the undisturbed and disturbed cases. While the impulse causes a large deviation from the nominal trajectory in early swing, the controller quickly recovers. From mid-swing onward, the foot follows a qualitatively similar path, maintains adequate ground clearance, and successfully reaches a similar foot placement as in the undisturbed case. In contrast, the prosthesis with impedance control does not respond adequately when subjected to the disturbance (fig. 4.14B). This is illustrated by the prosthesis behavior in mid swing, during which it does not react appropriately to maintain ground clearance of the toe. Rather, the joint-based impedance functions drive the knee into extension prematurely, and the prosthetic foot scuffs the ground resulting in a trip and subsequent fall.

4.2.4 Discussion

Our simulation results suggest that the hybrid neuromuscular control policy can improve amputee gait stability over existing impedance control methods. An amputee model walking with a powered pros-

Figure 4.14: Tripping response of the amputee model with neuromuscular (A) and impedance control (B) of the prosthesis. Shown are the prosthetic toe trajectories during undisturbed gait (dashed line) and when disturbed by a $15\text{ N}\cdot\text{s}$ impulse (solid line). The neuromuscular controller effectively responds to the disturbance and maintains a qualitatively similar toe trajectory. The impedance controller leads to foot scuffing and an eventual fall.

thesis showed substantial improvements in balance recovery on rough ground and after swing leg trips when using the hybrid neuromuscular control policy as opposed to impedance control. One possible reason for the improvement is that the proposed controller considers global leg information such as the target leg angle (eqs. (3.26) to (3.28)), and it is well known that without placing the feet into proper target points on the ground, legged systems fail to balance [Townsend, 1985, Raibert, 1986, Kajita et al., 2001, Seyfarth et al., 2002, Pratt et al., 2006, Wu and Geyer, 2013]. A second reason could be that the design of the swing leg control policy explicitly accounts for large disturbances to the lower limb dynamics in order to achieve desired leg placements [Desai and Geyer, 2012]. Neither is the case for current impedance control policies; however, future research may show that impedance or other control policies can equally make use of this global information and design criterion.

Whether the simulation results transfer to amputee gait remains to be determined. In an initial test with a non-amputee experimenter wearing the prosthesis via a knee adaptor, we found the hybrid neuromuscular control reproduces normal walking patterns qualitatively and effectively responds to disturbances in early and late swing. To understand if these initial results generalize to amputee locomotion requires further research. First, we only simulated disturbances in the hardware tests by commanding disturbance torques to the prosthesis knee. This approach allowed us to apply reproducible disturbances, but it does not capture real tripping or obstacle encounters, which will, for instance, exert torques about the hip joint as well. Second, the use of the knee adaptor creates abnormal kinematics and inertias and provides only a loose fit between user and prosthesis. In consequence, we only tested slow walking at 0.5 m/s holding onto hand rails.

Finally, the simulation and hardware tests captured only a small portion of the balance disturbances that humans typically encounter [Robinovitch et al., 2013]. Other disturbances may evoke amputee responses that the simulation model does not capture; especially since it is driven solely by a reflexive walking controller that ignores conscious interventions. Already, the hardware experiments revealed that the control's response to mid-swing disturbances does not match observed human responses and risks allowing the user to fall. This result suggests the model and corresponding hardware implementation require additional reflexes or structural changes in the control to better capture human locomotion and balance recovery. Foot placement into target points, while beneficial in particular for responding to early swing disturbances and for rough ground walking, may not be a goal that the human system prioritizes in

response to other disturbances. Identifying human objectives in these situations could lead to improved leg prosthesis behaviors independent of the proposed approach, impedance-like approaches, or other control design approaches.

4.3 Optimization of Systems Using Preferences

4.3.1 Introduction

Optimizing control policies for human-in-the-loop robotic systems, such as lower-limb prostheses and exoskeletons, is a challenging task due to two key issues. First, to optimize these systems it is currently necessary to define an objective function that includes and correctly assigns importance to all characteristics that determine system performance. For instance, consider an amputee trying to optimize the control parameters of her robotic leg prosthesis. The amputee could evaluate the prosthesis performance via an objective function that trades off important gait characteristics in order to guide the optimization. However, gait features, such as metabolic energy consumption, speed, and gait symmetry, require a high level of technical expertise and equipment to measure. Moreover, other aspects of gait may also be important but difficult to quantify, such as the amputee's comfort and sense of stability. Even if the amputee could measure all these characteristics, the objective function would still need to assign weights to each feature that reflect the amputee's individual needs.

To solve the problem of defining objective functions for robotic systems that human operators can directly control, researchers have proposed *learning from demonstration* (LfD) [Argall et al., 2009]. In this paradigm, we can either circumvent learning the objective function by directly learning a policy that matches the distribution of state-action pairs recorded during human demonstrations of the desired behavior [Pomerleau, 1991, Schaal, 1999], or we can learn a reward function consistent with the demonstrator's actions and visited states and use it to derive an optimal control [Ng et al., 2000, Ratliff et al., 2006, Ziebart et al., 2009]. LfD methods are attractive because they allow non-experts to specify both the quantifiable and qualitative aspects of the desired robot behavior via the non-technical language of demonstration.

For robot behavior that people cannot demonstrate, such as the optimal behavior of an amputee's prosthesis, or the desired behavior of complex, dynamic robots, we can alternatively query human users for qualitative feedback in order to shape the robot policy. For example, the TAMER framework [Knox and Stone, 2009, Knox et al.,

2013] utilizes good/bad assessments of a robot's recent actions to optimize its policy. Pilarski et al. use this method to allow subjects to optimize the policy of an EMG-controlled prosthesis arm via their positive and negative feedback signals [Pilarski et al., 2011]. Another paradigm in qualitative feedback is to obtain *preference feedback* between two or more policies or sequences of actions, which may provide more nuanced feedback than absolute ratings. For example, Jain et al. and Akrou et al. propose methods that learn a user's trajectory scoring function based on his rankings of possible policies [Jain et al., 2013, Akrou et al., 2014]. Similarly, Wilson et al. provide a method to directly identify a user's preferred policy based on her preferences between pairs of demonstrated trajectories [Wilson et al., 2012]. These prior works demonstrate that we can successfully use qualitative feedback, such as preferences, from non-expert users to program robot behavior, without prescribing an objective function.

A drawback of the aforementioned methods that learn from preference feedback is their reliance on simulators to predict system behavior. Human-in-the-loop systems, such as lower-limb prostheses and exoskeletons, are challenging to simulate accurately, making these methods difficult to apply. If the control is governed by a fixed set of parameters, as is often the case for these kinds of systems, we can instead employ model-free *black-box* optimization methods. These methods have gained traction in the related field of control optimization for dynamic locomotion, where it can be difficult to model the nonlinear, discontinuous dynamics of these systems. Specifically, many have applied stochastic or "evolutionary" optimization methods, which repeatedly sample and mix control parameters that perform well, to locomotion control problems [Gong et al., 2010].

The second issue an operator tasked with optimizing control policies for human-in-the-loop systems faces is the expense, in terms of time and effort, of repeatedly executing policies. Consequently, stochastic sampling approaches may be less applicable in this domain. To minimize the number of trials needed, researchers have proposed black-box *Bayesian Optimization* (BO) methods that model both the objective function and its uncertainty. In these methods, the uncertainty informs an acquisition function that speeds up the optimization by exploiting regions of the parameter space with believed high objective value while still exploring regions where the objective function is uncertain. For example, researchers have successfully employed BO methods to efficiently optimize the gait parameters of a robotic snake [Tesch et al., 2011] and a dynamic bipedal robot [Calandra et al., 2014].

This work is motivated by the observation that prior research has not thoroughly explored solutions that address both the difficulty

of defining objective functions and the expense of running repeated experiments for systems that are difficult to model and for which qualitative characteristics are important. We present a new optimization algorithm, Predictive Entropy Search with Preferences (PES-P), that addresses these issues. The algorithm uses preference queries between pairs of control parameters to avoid the a priori definition of features and to consider unquantifiable qualities of the desired behavior. The algorithm further incorporates black-box Bayesian optimization to ensure its preference queries gather information efficiently without relying on a system model.

In developing the algorithm, we make three main contributions. First, we adapt an acquisition function previously proposed for interval scale feedback to the preference feedback case. This acquisition function seeks a pair of parameters for which a preference will maximally reduce the entropy of the distribution of objective function optima. Second, we compare in simulation the performance of the proposed optimization method against the expected improvement method (EI) and uniform random sampling via Latin hypercubes (LH) for two classes of examples: optimizing randomly generated objective functions and tuning the control parameters of simulated dynamical systems. Finally, we compare the performance of the three methods for the task of optimizing the control parameters of a robotic prosthesis given real user feedback.

4.3.2 Preliminaries

Learning from Preferences

To learn latent objective functions from preferences, we rely on the method developed by Chu and Ghahramani [Chu and Ghahramani, 2005], briefly reviewed here. The method considers a training dataset D_n of n preferences between pairs of points, $\{x_1^a \succ x_1^b, \dots, x_k^a \succ x_k^b, \dots, x_n^a \succ x_n^b\}$. These points can, for instance, represent control policy parameters. From the dataset, the method finds a posterior distribution of latent objective functions f ,

$$P(f|D_n) = \frac{P(D_n|f) P(f)}{P(D_n)}. \quad (4.5)$$

The method assumes that the prior distribution of objective functions is a zero-mean *Gaussian process* (GP), $P(f) = \mathcal{N}(0, \Sigma)$. (See [Williams and Rasmussen, 2006] for a full description of GPs.) In eq. (4.5), $P(D_n|f)$ is the overall likelihood of preferences in the dataset given specific objective function values and is modeled as the product of the likelihood of each independent preference in the dataset. The likelihood model for preferences proposed by Chu and Ghahramani

increases the certainty of a preference between x_k^a and x_k^b as the difference between $f(x_k^a)$ and $f(x_k^b)$ widens. This model stems from the assumption that Gaussian noise with variance σ^2 corrupts the user's latent objective function f .

To obtain the posterior distribution $P(f|D_n)$ the method approximates eq. (4.5) with a Gaussian distribution. As a result, the predictive distribution (subscript p) of the objective function at test points, f_t , is also Gaussian, $P(f_t|D_n) = \mathcal{N}(\mu_p, \Sigma_p)$. Finally, the predictive distribution of a preference between two points x^a and x^b is

$$P(x^a \succ x^b | D_n) = \int P(x^a \succ x^b | f_t, D_n) P(f_t|D_n) df_t \quad (4.6)$$

$$= \Phi\left(\frac{\mu^a - \mu^b}{\sigma_p}\right), \quad (4.7)$$

$$\sigma_p^2 = 2\sigma^2 + \Sigma_p^{aa} + \Sigma_p^{bb} - \Sigma_p^{ab} - \Sigma_p^{ba}, \quad (4.8)$$

where $\Phi(\cdot)$ is the cumulative density function of the standard normal distribution.

Figure 4.15a provides an example of how the method estimates a ground-truth objective function shown in purple. The blue line and shaded area show the mean and standard deviation of the posterior distribution of objective functions, $P(f_t|D_n)$, after two preference queries between pairs of parameters (orange, higher is preferred over lower value). The queries have the effect of lifting the estimated objective function close to preferred points and pushing it down close to unpreferred points, approximating the true objective function over time.

Active Learning for Optimization

Learning from preferences describes how to find a distribution of objective functions given a dataset of comparisons. The question now becomes how to efficiently solicit preferences from the user. As our main goal is to find the optimal parameters x^* , we should forgo modeling the objective function accurately in all parameter regions and instead focus on regions where the objective might be high. Bayesian optimization addresses this problem with an acquisition function that helps to efficiently sample training data.

One such acquisition function is the expected improvement, which has been used both in the context of preference feedback [Brochu et al., 2008] and interval scale feedback [Jones et al., 1998],

$$EI(x) = (\mu^* - \mu(x))\Phi(d) + s(x)\phi(d), \quad (4.9)$$

where $d = (\mu^* - \mu(x))/s(x)$, μ^* is the mean of the current estimate of the optimum, and $\mu(x)$ and $s(x)$ are the mean and standard deviation of the objective of a new point x , respectively. As

an alternative, for interval scale feedback, [Hennig and Schuler, 2012] and [Hernández-Lobato et al., 2014] proposed acquisition functions that seek to reduce the uncertainty in the distribution of objective function optima, measured in terms of the differential entropy. For example, the Predictive Entropy Search acquisition function [Hernández-Lobato et al., 2014] seeks a point x that is expected to reduce the entropy of the distribution of optima x^* after observing its value y ,

$$\alpha_n(x) = H[P(x^*|D_n)] - E_{P(y|x,D_n)}[H[P(x^*|y,x,D_n)]], \quad (4.10)$$

where $H[P(x)] = - \int P(x) \log P(x) dx$ is the differential entropy. The authors of these methods have shown they can outperform EI.

4.3.3 Methods

Our goal is to simultaneously address both the difficulty of defining objective functions when an expert cannot demonstrate the desired robot behavior and the expense of running experiments on hardware. To this end, we adapt the Predictive Entropy Search acquisition function (eq. (4.10)) to the preference learning case.

Acquisition Function

To obtain the optimal parameters x^* with the smallest number of preference queries, we solicit preferences that maximize the expected information gain about the distribution of objective function optima $P(x^*|D_n)$. Adapting eq. (4.10) to preference feedback yields

$$\alpha_n(x^a, x^b) = H[P(x^*|D_n)] - E_{P(y|x^a, x^b, D_n)}[H[P(x^*|y, x^a, x^b, D_n)]], \quad (4.11)$$

where y is a binary random variable that represents the preference between x^a and x^b . The first term in this function is the current entropy of objective function optima and the second term is the entropy of optima after observing the preference y . As we have not yet observed the preference, we take the second term in expectation over the two possible preference outcomes.

As discussed in [Hernández-Lobato et al., 2014], this acquisition function is intractable to compute. However, following the approach used for the original PES algorithm, we can rewrite eq. (4.11) in terms of the entropies of the predictive distribution of the preference between x^a and x^b ,

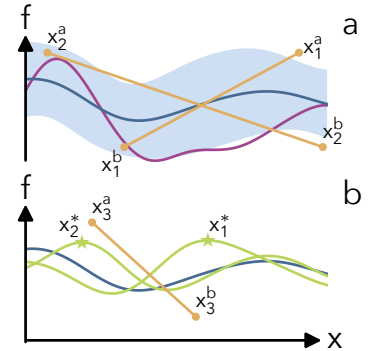


Figure 4.15: Learning from preferences. (a) Mean and standard deviation of $P(f_t|D_n)$ (blue) after two preferences queries (orange) from the true objective function (purple). (b) Mean of $P(f_t|D_n)$ (blue) and means of $P(f_t|D_n, x_m^*)$ (green) for two samples of x_m^* . PES-P queries a new comparison (orange) for which the preference is currently uncertain, but on average is certain after conditioning on all x_m^* .

$$\alpha_n(x^a, x^b) = H \left[P(y|x^a, x^b, D_n) \right] - E_{P(x^*|D_n)} \left[H \left[P(y|x^*, x^a, x^b, D_n) \right] \right] \quad (4.12)$$

$$\approx H \left[P(y|x^a, x^b, D_n) \right] - \frac{1}{M} \sum_{x_m^* \sim P(x_m^*|D_n)}^M H \left[P(y|x_m^*, x^a, x^b, D_n) \right]. \quad (4.13)$$

This reformulation significantly improves computability. First, the new acquisition function uses the entropies of probabilities of preferences, given by eq. (4.7). Second, we now take the expectation over $P(x^*|D_n)$, which we can perform by sampling M functions from $P(f_t|D_n)$ and optimizing each one to get M samples of x^* (see Appendix for details). Finally, the second term no longer requires conditioning the GP on every pair of x^a and x^b considered during optimization of the acquisition function. Instead, we only have to condition the Gaussian process M times on (x_m^*, D_n) .

For the experiments in section 4.3.4 we choose $M = 12$, which allows us to construct and optimize $\alpha_n(x^a, x^b)$ in about five seconds, which is fast enough for our prosthesis application. Although 12 samples of x^* is not enough to compute an accurate expectation over $P(x^*|D_n)$, interpreting the algorithm as an example of active learning by disagreement may explain why it still works well. As shown in fig. 4.15b, optimizing the acquisition function chooses a pair x^a and x^b for which the preference is currently uncertain, but certain on average after conditioning on all x_m^* . The sampled x_m^* do not necessarily agree on which point is preferred; hence, after observing the preference, the algorithm can rule out x_m^* that made the model certain but wrong about the preference. This intuition is similar to that provided by [Houlsby et al., 2012] for Bayesian active learning by disagreement for GP classifiers.

*Conditioning the Gaussian Process on x^**

The second term on the right side of eq. (4.13) requires us to compute the distribution of the preference given the location of the optimum,

$$P(y|x_m^*, x^a, x^b, D_n) = \int P(x^a \succ x^b | f_t, x_m^*, D_n) P(f_t|x_m^*, D_n) df_t. \quad (4.14)$$

It is not directly feasible to condition the predictive distribution on x^* , so instead we turn to approximating this condition with three constraints (see appendix for details):

C1: First we impose that x^* is a local maximum by ensuring that the gradient of $f(x^*)$ is zero and its Hessian is negative definite. We further simplify the Hessian constraint to only require that the Hessian's off-diagonal elements are zero and its diagonal elements

Algorithm 1: Predictive Entropy Search with Preferences

```

1: procedure PES-P
2:    $D_n = \emptyset$ 
3:   for  $n \leftarrow 0$  to  $N - 1$  do  $\triangleright N$  iterations
4:      $F \leftarrow \{f_m \sim P(f_t|D_n) | m \in [1, M]\}$ 
5:      $X^* \leftarrow \{\arg \max_x (f_m) | f_m \in F\}$ 
6:      $(x_{n+1}^a, x_{n+1}^b) \leftarrow \arg \max_{(x^a, x^b)} ff_n(x^a, x^b; X^*)$ 
7:      $y_{n+1} \leftarrow \text{QUERYUSERPREF}(x_{n+1}^a, x_{n+1}^b)$ 
8:      $D_{n+1} \leftarrow D_n \cup (x_{n+1}^a, x_{n+1}^b, y_{n+1})$ 
9:   end for
10:  return  $x^* \leftarrow \arg \max_x \text{mode}(P(f_t(x)|D_N))$ 
11: end procedure

12: function  $\alpha_n(x^a, x^b; X^*)$   $\triangleright$  acquisition function
13:    $h \leftarrow \left\{ H \left[ P(y|x^a, x^b, D_n, C1, C2, C3) \right] | x_m^* \in X^* \right\}$ 
14:   return  $H \left[ P(y|x^a, x^b, D_n) \right] - \text{mean}(h)$ 
15: end function
```

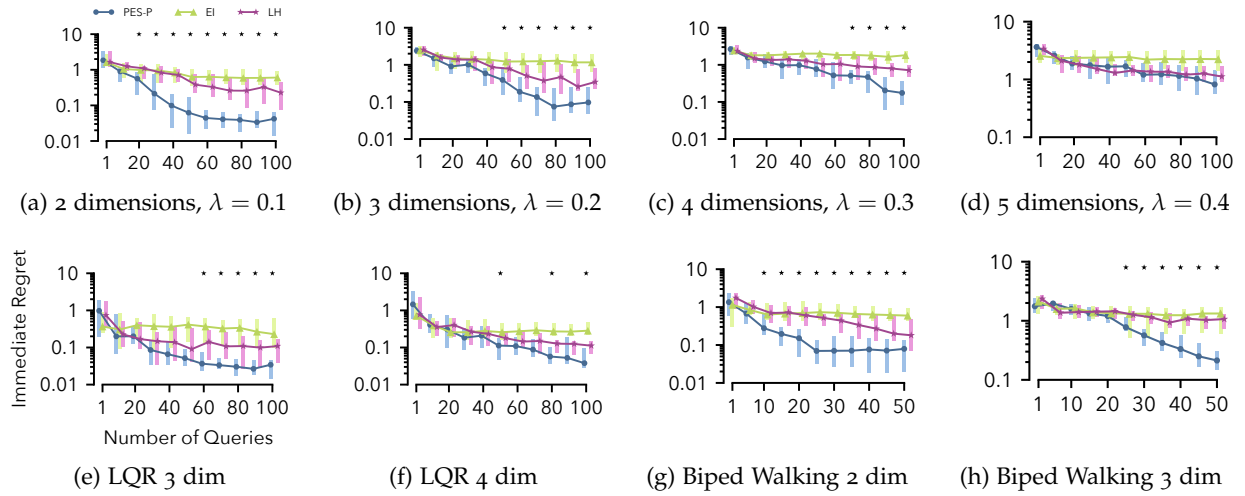
are less than zero. We implement the gradient and off-diagonal constraints by conditioning the prior, $P(f)$, on derivative observations as outlined in [Solak et al., 2003]. To constrain the diagonal elements of the Hessian, we amend the likelihood term in eq. (4.5) by adding terms that penalize Hessians with positive diagonal elements.

C₂: Second, we try to ensure that x^* is also a global maximum by enforcing that $f(x^*)$ is greater than the function values of all training points sampled so far. We impose this constraint by adding more preference relations into the likelihood term in eq. (4.5) between x^* and all training points.

C₃: Finally, to further ensure that $f(x^*)$ is a global maximum, we require that it is also larger than the function values of the two new test points, $f(x^a)$ and $f(x^b)$. Whereas C₂ ensures $f(x^*)$ exceeds function values in areas explored so far, C₃ ensures that $f(x^*)$ also exceeds function values in unexplored regions. We approximate this constraint analytically by conditioning on the single constraint $f(x^*) > (f(x^a) + f(x^b))/2$ using the method detailed in [Xu and Li, 2010].

Algorithm Summary

With constraints C₁ to C₃, at each iteration we can efficiently compute the acquisition function, eq. (4.13). We summarize the resulting Predictive Entropy Search with Preferences (PES-P) algorithm as follows (algorithm 1): At each iteration n , first, the algorithm sam-



ples M objective functions from the current distribution, $P(f_t|D_n)$, and optimizes each one to generate M samples of x^* (lines 4 and 5). Next, using the set of sampled optima X^* , we maximize the acquisition function to obtain the next two points to present to the user x_{n+1}^a and x_{n+1}^b (lines 6 and 12–15). Note: we can precompute the effect of C_1 and C_2 before evaluating $ff_n(x^a, x^b)$ as these two constraints do not depend on x_{n+1}^a and x_{n+1}^b . On the other hand, C_3 depends directly on x_{n+1}^a and x_{n+1}^b and therefore is computed within the acquisition function for every pair of points considered during the optimization of $ff_n(x^a, x^b)$. We then query the user to obtain their preference y_{n+1} between these two points and add it to the dataset of preferences (lines 7 and 8). Finally, at the end of the N iterations of the algorithm, we return the optimum x^* of the most likely function, mode($P(f_t(x)|D_N)$), which is equal to the posterior mean function in the Gaussian process case (line 10). While it may be more correct to return mode($P(x^*|D_N)$), we do not do this as the PES algorithm seeks to avoid approximating this distribution.

4.3.4 Results

We test the ability of PES-P to solve optimization problems in four cases with increasing realism from the optimization of randomly generated objective functions drawn from a GP, to the tuning of feedback gains of random linear systems and a neuromuscular walking model, to the optimization of control parameters for a powered transfemoral prosthesis given real user feedback. In all four cases, we compare the performance of the proposed algorithm to the expected improvement criterion (EI) (eq. (4.9)) and random sampling via Latin hypercubes

Figure 4.16: Performance of predictive entropy search with preferences (PES-P), expected improvement (EI), and Latin hypercube random sampling (LH) for optimizing random objective functions sampled from a GP (a-d), and tuning feedback control parameters of random linear systems (e-f) and a biped walking model (g-h). Shown are the median and interquartile range over 20 trials of the immediate regret (IR) against the number of preference queries. Black stars indicate iterations for which PES-P achieves statistically significant stochastic reductions in IR compared to both EI and LH according to one-sided Mann-Whitney U tests ($p < 0.05$).

(LH)¹ [McKay et al., 2000]. For the three simulated cases, we show results over 20 trials and measure performance in terms of the immediate regret, defined as $IR = |f(\tilde{x}_n^*) - f(x^*)|$, versus the number of iterations. Here, $f(\tilde{x}_n^*)$ is the objective value of the current estimate of the optimum at this iteration, $f(x^*)$ is the value of the true optimum, and an iteration consists of a single preference query between two points. Additionally, we also check the statistical significance of the reduction in IR obtained by PES-P compared to both EI and LH via one-sided Mann-Whitney U tests ($p < 0.05$).

Optimizing Randomly Generated Objective Functions

To avoid inducing bias by hand-engineering test functions, we first evaluate the algorithm on random synthetic objective functions. We generate objective functions on the domain $x \in [-1, 1]^D$ by sampling a vector of 500 function values from a GP prior with a quadratic mean, $\mu(x) = -x^T x$, and isometric squared exponential covariance $k(x_i, x_j) = \exp\left(\frac{-1}{2\lambda} x_i^T x_j\right)$. We use a quadratic mean function to bias the function distribution away from those that have their optimum on a boundary of the domain, as these functions are easier to optimize. We continue to generate the rest of the function as it is optimized by conditioning the GP on the 500 seed values and all function values sampled during the optimization. We assume the mean of the final function distribution is the true objective function. To simulate more realistic situations, we provide the algorithms with noisy preferences from the sampled function values ($\sigma^2 = 0.1$).

Figures 4.16a-d show the immediate regret for two to five dimensional problems with λ , the length scale of the kernel, scaling from 0.1 to 0.4 as the dimensionality of the problem increases. On two to four dimensional problems, PES-P outperforms EI and LH by achieving statistically significant reductions in IR. However, as the dimensionality increases, it takes more iterations for this advantage to become apparent. In the five dimensional case, there is no significant difference between PES-P and LH, likely due to $M = 12$ samples of x_m^* being insufficient and the difficulty of accurately sampling x_m^* in higher dimensions.

Tuning Controllers for Random Linear Systems

Next, we test the ability of PES-P to optimize simple control systems by optimizing the feedback gains K for D -dimensional single-input linear systems $\dot{\xi} = A\xi + Bu$ with feedback $u = K\xi$. We sample the elements of the A matrix from the standard normal distribution while $B = [0_{1 \times (D-1)}, 1]^T$. We assume a quadratic instantaneous cost

¹ LH sampling divides the parameter space into $(2N)^D$ hypercubes, where D is the dimensionality of the space. $2N$ samples are placed such that each hypercube has at most one sample and there is at most one filled hypercube along any row of hypercubes when viewed along any direction. This method ensures that the samples are roughly uniformly distributed in the entire space. At each iteration we choose two of these samples to query users.

resulting in the objective function

$$f(K) = - \int_0^{t_f} \xi_K^T(t)(Q + K^T R K)\xi_K(t)dt, \quad (4.15)$$

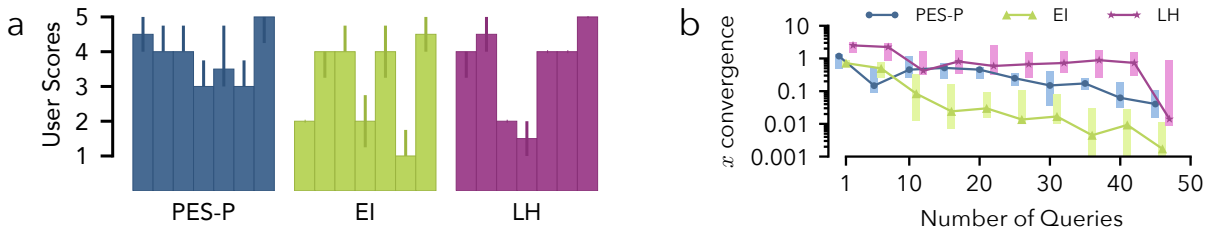
where $\xi_K(t)$ is the evolution of the state under the control policy K and a fixed initial condition ξ_0 , $Q = I_{D \times D}$ and $R = 1$. To obtain a finite search domain, we find the stable range of parameters by varying the elements of the true optimal control parameters K^* one at a time while keeping other elements constant. We scale and shift this region to map to the domain $[-1, 1]^D$. Finally, we use the Automatic Relevance Determination Gaussian Kernel and optimize the hyperparameters at each iteration by maximizing the posterior probability of the hyperparameters under a gamma hyperprior [Chu and Ghahramani, 2005, Williams and Rasmussen, 2006]. In order to apply a consistent noisy preference model ($\sigma^2 = 0.1$) across all sampled systems, we transform all objective values by first mapping them through $-\log(-f(K))$ and then shifting and scaling the values by the mean and range of the values of 10^D randomly sampled controllers.

Figures 4.16e and 4.16f show the resulting optimization performance on three and four dimensional systems. In the 3 dimensional case, PES-P achieves a lower median IR than LH after 30 iterations. This difference becomes significant after 60 iterations. In the 4 dimensional case, PES-P significantly outperforms LH after 50 iterations, but the significance of this improvement is sporadic as the iterations continue. A possible reason for the reduced performance difference between PES-P and LH in the LQR problem as compared to the random objective function problems is the existence of hard-to-optimize flat regions in the LQR objective functions. This suggests that PES-P may be more well suited for problems that have clear optimum.

Tuning Control Parameters of a Walking Model

In the third case, we test the ability of PES-P to optimize the feedback gains for a neuromuscular model of walking [Thatte and Geyer, 2016], a system with a complex non-linear controller addressing the specific application domain of human locomotion. We perform two and three dimensional optimizations, in which we tune the feedback gains for a subset of the model's muscle actuators. We use the negative cost of transport plus the distance walked over a 20 second time span as the objective function. As in the previous linear systems example, we obtain noisy preferences between parameters and optimize the hyperparameters at every iteration.

Figures 4.16g and 4.16h show the performance of PES-P, EI, and LH. In this example, PES-P achieves a significant reduction in IR in



just 10 iterations in the 2-dimensional case and in 25 iterations in the 3 dimensional case. Furthermore, in the 3D case the PES-P's median solution is approximately 10 times better than those found by EI or LH.

Tuning a Transfemoral Prosthesis from User Preferences

In the last test case, we applied the three algorithms to optimize the control parameters for a powered transfemoral prosthesis given real user preferences. Specifically, a neuromuscular model similar to the one used in section 4.3.4 controls the prosthesis and we optimize the strengths of three virtual knee muscles of this control [Thatte and Geyer, 2016].

We performed this test in a pilot study with seven healthy users. They walked on a treadmill and wore the powered prosthesis with a modified knee brace (compare [Thatte and Geyer, 2016]). We allowed all users an hour-long session to acclimate to the device, during which they experienced a variety of controller conditions. On a second day, we optimized the prosthesis parameters using the three algorithms (PES-P, EI, and LH) in a random order, for 50 iterations each. During an iteration, the users walked with two parameter settings chosen by the algorithm (each for 10 seconds) and then indicated which setting they preferred. After completing the three optimizations, the users walked with the optimum parameters identified by each algorithm (in a random order) for fifteen seconds and then rated each optimum on a 1 (bad) to 5 (good) scale. We repeated the scoring procedure six times to cover all possible orderings of the three optima.

Figure 4.17 summarizes the results from the optimizations with user preferences. PES-P and LH achieved median user scores of 4 while EI achieved a median score of 3 (Fig. 4.17a). In addition, PES-P, LH, and EI achieved mean scores of 4.0, 3.5, and 3.1, respectively (not shown). The gap between the mean and median scores for LH implies that LH does not achieve high scores as consistently as PES-P.

Figure 4.17: Optimization of prosthesis control with user preferences. (a) Median and interquartile range of user scores achieved by PES-P, EI and LH after 50 iterations (total of 42 scores per algorithm: seven users times six scorings). (b) Median and interquartile range of convergence achieved by the three algorithms as measured by the Euclidean distance between the current and final estimates of the optimum. PES-P and LH achieve the same median score of 4 across all users but PES-P converges faster and more consistently. EI converges fastest but to a lower median score of 3.

A second observation is that PES-P converged faster than LH to the optimum as measured by the distance between its current and final estimates, $\|\tilde{x}_n^* - \tilde{x}_N^*\|$ (Fig. 4.17b). Meanwhile, EI tended to converge fastest, but to lower scoring parameters on average (Fig. 4.17a).

4.3.5 Discussion and Conclusion

We presented a new optimization algorithm (PES-P) that extends Predictive Entropy Search to preference feedback. The algorithm addresses two key problems frequently encountered in system optimization. First, it circumvents the often difficult process of parameterizing and learning an objective function by directly querying users for preferences between pairs of parameters. Second, the algorithm minimizes the required number of hardware experiments by employing Bayesian optimization techniques that ensure the queries maximize the information gained about the location of the optimum. Moreover, unlike previous approaches for preference learning on robotic systems [Wilson et al., 2012, Jain et al., 2013], PES-P does not require a model of the system.

Our experiments show that the proposed algorithm outperforms baseline algorithms. In most of the simulation experiments PES-P found optima that achieved higher objective values than those found by the expected improvement method (EI) or by random comparisons via Latin hypercubes (LH) (fig. 4.16). In the prosthesis experiment, PES-P outperformed EI and achieved final scores similar to LH with faster convergence (fig. 4.17). These results suggest the proposed algorithm can help engineers optimize some types of human-in-the-loop robotic systems more accurately, efficiently, and consistently.

The reason why PES-P outperformed EI is likely due to the former's explicit consideration of how the limited, noisy information obtained from a preference query will affect the knowledge about potential objective function optima. The acquisition function (eq. (4.11)) recognizes that preferences become more uncertain the closer two sample points are to each other. EI, on the other hand, does not reason about noisy preferences and, instead, still assumes it can sample values (eq. (4.9)). Consequently, EI ignores the distance between sample points, which often leads to a greedy strategy that solicits preferences between adjacent points. While this strategy can resemble gradient ascent with convergence to local optima in a noise-free optimization, it often failed in our simulated and real experiments characterized by noisy observations. Note, however, that such limitations were not observed by Brochu and colleagues [Brochu et al., 2008], who successfully used EI with preferences to optimize parameters for a graphics application, possibly because the associated

visual task produced less noisy responses than did our simulations or prosthesis walking task.

Several modifications could improve the PES-P algorithm. First, using a non-zero prior mean function governed by a set of hyperparameters could embed specific knowledge about the problem to speed up optimization. To improve efficiency in this way, [Brochu et al., 2010] details an approach for learning hyperpriors that could be integrated with PES-P. Second, integrating more varied user feedback may also help improve the algorithm. For example, “I don’t know” responses could imply that the function values at two points are similar, absolute good and bad ratings could encourage the algorithm to more quickly explore promising control policies and avoid bad ones, and derivative observations could indicate the user prefers more or less of a parameter. With these two changes, the algorithm may be able to tackle higher dimensional problems. Finally, including time as a dimension in the GP could account for user adaptation to the robotic system.

Appendix

To obtain X^* (line 5, algorithm 1), we sample M functions from the posterior by approximating $P(f_t|D_n)$ using Bayesian linear regression with Fourier features (as outlined in [Hernández-Lobato et al., 2014]) and sampling M feature weight vectors. As the Fourier features have analytic derivatives, we can optimize each linear function using a second order method with multiple restarts.

We approximate conditioning the predictive distribution on x^* via three constraints:

C1 x^* is a local maximum. $\nabla f|_{x^*} = 0$ and the Hessian of the objective function is negative definite by imposing $\text{diag}(\nabla \nabla f|_{x^*}) < 0$ and $\text{upper}(\nabla \nabla f|_{x^*}) = 0$. We group $\nabla f|_{x^*} = 0$ and $\text{upper}(\nabla \nabla f|_{x^*}) = 0$ into constraint C1.1 and $\text{diag}(\nabla \nabla f|_{x^*}) < 0$ into constraint C1.2.

C2 x^* is preferred to current training points, $f(x^*) > f(x_k^a)$ and $f(x^*) > f(x_k^b)$, $\forall k \in [1, n]$.

C3 x^* is preferred to new training points, $f(x^*) > f(x_{n+1}^a)$ and $f(x^*) > f(x_{n+1}^b)$.

We precompute the effects of constraints C1 and C2 before evaluation of $\text{ff}_n(x^a, x^b)$. To impose C1 and C2, we first divide their components into two groups: $c = [\nabla f|_{x^*}^\top, \text{upper}(\nabla \nabla f|_{x^*})^\top]^\top$ and $f' = [f^\top, \text{diag}(\nabla \nabla f|_{x^*})^\top, f(x^*)]^\top$. Note C1.1 $\implies c = 0$. We write the predictive distribution of the objective function at test points f_t

given constraints C1 and C2 as

$$P(f_t|D_n, C1, C2) = \int P(f_t|f', C1.1) P(f'|D_n, C1, C2) df'. \quad (4.16)$$

We use Bayes rule to evaluate the second term in the integral,

$P(f'|D_n, C1, C2) = \frac{P(D_n, C1.2, C2|f') P(f'|C1.1)}{P(D_n, C1.2, C2|C1.1)}$. We form the prior term $P(f'|C1.1)$ by conditioning the joint distribution, $P(c, f')$ on C1.1 given by $c = 0$. $P(f'|c) = \mathcal{N}(f'|\Sigma_{cf'}^T \Sigma_{cc}^{-1} c, \Sigma_{ff'} - \Sigma_{cf'}^T \Sigma_{cc}^{-1} \Sigma_{cf'})$ implies $P(f'|c = 0) = \mathcal{N}(f'|0, \Sigma_{f'|c})$.

We implement the likelihood term by adding extra factors to the likelihood in eq. (4.5) that impose soft constraints representing C1.2 and C2. For C1.2 we use the penalty term $P([\nabla \nabla f|_{x^*}]_{dd} < 0 | [\nabla \nabla f|_{x^*}]_{dd}) = \Phi(-[\nabla \nabla f|_{x^*}]_{dd}/\sigma_h)$ and for C2 we add more preference relations between x^* and all training points.

$$\begin{aligned} P(D_n, C1.2, C2, |f') &= \left[\prod_{k=1}^n P(x_k^a \succ x_k^b | f(x_k^a), f(x_k^b)) P(x^* \succ x_k^a | f(x^*), f(x_k^a)) P(x^* \succ x_k^b | f(x^*), f(x_k^b)) \right] \\ &\times \prod_{d=1}^D P([\nabla \nabla f|_{x^*}]_{dd} < 0 | [\nabla \nabla f|_{x^*}]_{dd}) \\ &= \left[\prod_{k=1}^n \Phi(q_k) \Phi(q_k^{a*}) \Phi(q_k^{b*}) \right] \prod_{d=1}^D \Phi(q_d^h) \end{aligned} \quad (4.17)$$

Where $q_k^{a*} = \frac{f(x^*) - f(x_k^a)}{\sqrt{2}\sigma}$ and $q_k^{b*} = \frac{f(x^*) - f(x_k^b)}{\sqrt{2}\sigma}$ and $q_d^h = \frac{-[\nabla \nabla f|_{x^*}]_{dd}}{\sigma_h}$. We use Laplace's approximation to approximate $P(f'|D_n, C1, C2)$ as Gaussian,

$$P(f'|D_n, C1, C2) \approx \mathcal{N}\left(f' | f'_{MAP}, \left(\Sigma_{f'|c}^{-1} + \Lambda_{f'_{MAP}}\right)^{-1}\right), \quad (4.18)$$

where $f'_{MAP} = \arg \min_{f'} -\log P(f'|D_n, C1, C2)$ and $\Lambda_{f'_{MAP}}$ is the Hessian of $-\log P(D_n, C1.2, C2|f')$ evaluated at f'_{MAP} .

We compute the first term in eq. (4.16), $P(f_t|f', C1.1)$ by conditioning the joint distribution $P(c, f', f_t)$ on f' and $c = 0$,

$$P(f_t|f', c = 0) = \mathcal{N}\left(f_t | \left(\Sigma_{ct}^T B + \Sigma_{f't}^T D\right) f' + \Sigma_{tt} - \begin{bmatrix} \Sigma_{ct}^T & \Sigma_{f't}^T \end{bmatrix} \begin{bmatrix} A & B \\ C & D \end{bmatrix} \begin{bmatrix} \Sigma_{ct} \\ \Sigma_{f't} \end{bmatrix}\right), \quad (4.19)$$

where, $\begin{bmatrix} A & B \\ C & D \end{bmatrix} = \begin{bmatrix} \Sigma_{cc} & \Sigma_{cf'} \\ \Sigma_{cf'}^T & \Sigma_{ff'} \end{bmatrix}^{-1}$. We can substitute eq. (4.19) and eq. (4.18) into eq. (4.16) to yield the predictive distribution subject to constraints C1 and C2.

$$\begin{aligned} P(f_t|D_n, C1, C2) = & \mathcal{N} \left(f_t | (\Sigma_{ct}^T B + \Sigma_{f't}^T D) f'_{MAP}, \Sigma_{tt} - \begin{bmatrix} \Sigma_{ct}^T & \Sigma_{f't}^T \end{bmatrix} \begin{bmatrix} A & B \\ C & D \end{bmatrix} \begin{bmatrix} \Sigma_{ct} \\ \Sigma_{f't} \end{bmatrix} \right. \\ & \left. + (\Sigma_{ct}^T B + \Sigma_{f't}^T D) (\Sigma_{f'|c}^{-1} + \Lambda_{f'_{MAP}})^{-1} (\Sigma_{ct}^T B + \Sigma_{f't}^T D)^T \right). \end{aligned} \quad (4.20)$$

We obtain $P(f_t|D_n, C1, C2, C3)$ by analytically conditioning eq. (4.20) on the single inequality $f(x_m^*) > (f(x^a) + f(x^b))/2$ using the method detailed in [Xu and Li, 2010]. Finally, using eq. (4.14) we can compute the predictive distributions of preferences given the locations of x_m^* .

To optimize $ff_n(x^a, x^b)$ (line 7, algorithm 1) we construct its gradient by evaluating $P(f_t|D_n)$ and $P(f_t|D_n, C1, C2, C3)$ at test points x^a and x^b as well as points offset by $\delta_x = \pm 0.001$ along each dimension. We then optimize $\alpha_n(x^a, x^b)$ via gradient ascent.

5

Proposed Work

- 5.1 *Evaluation of Neuromuscular Transfemoral Prosthesis Control*
- 5.2 *Optimizing Prosthesis Control using Preferences*
- 5.3 *Learning Trip Recovery Policies*
- 5.4 *Proposed Work Summary and Timeline*

Bibliography

Mostafa Ajallooeian, Soha Pouya, Alexander Sproewitz, and Auke J Ijspeert. Central pattern generators augmented with virtual model control for quadruped rough terrain locomotion. In *Robotics and Automation (ICRA), 2013 IEEE International Conference on*, pages 3321–3328. IEEE, 2013.

Riad Akrou, Marc Schoenauer, Michèle Sebag, and Jean-Christophe Souplet. Programming by feedback. In *International Conference on Machine Learning*, number 32, pages 1503–1511. JMLR.org, 2014.

Brenna D Argall, Sonia Chernova, Manuela Veloso, and Brett Browning. A survey of robot learning from demonstration. *Robotics and autonomous systems*, 57(5):469–483, 2009.

Samuel K Au and Hugh M Herr. Powered ankle-foot prosthesis. *IEEE Robotics & Automation Magazine*, 15(3):52–59, 2008.

Samuel K Au, Jeff Weber, and Hugh Herr. Biomechanical design of a powered ankle-foot prosthesis. In *2007 IEEE 10th International conference on rehabilitation robotics*, pages 298–303. IEEE, 2007.

Ryan D Bellman, Matthew A Holgate, and Thomas G Sugar. Sparky 3: Design of an active robotic ankle prosthesis with two actuated degrees of freedom using regenerative kinetics. In *2008 2nd IEEE RAS & EMBS International Conference on Biomedical Robotics and Biomechatronics*, pages 511–516. IEEE, 2008.

Malte Bellmann, Thomas Schmalz, and Siegmar Blumentritt. Comparative biomechanical analysis of current microprocessor-controlled prosthetic knee joints. *Archives of physical medicine and rehabilitation*, 91(4):644–652, 2010.

Eric Brochu, Nando D Freitas, and Abhijeet Ghosh. Active preference learning with discrete choice data. In *Advances in neural information processing systems*, pages 409–416, 2008.

Eric Brochu, Tyson Brochu, and Nando de Freitas. A bayesian interactive optimization approach to procedural animation design.

In *Proceedings of the 2010 ACM SIGGRAPH/Eurographics Symposium on Computer Animation*, pages 103–112. Eurographics Association, 2010.

Benjamin J Brown, Charlie G Crone, and Christopher E Attinger. Amputation in the diabetic to maximize function. In *Seminars in Vascular Surgery*, volume 25, pages 115–121. Elsevier, 2012.

T Graham Brown. The intrinsic factors in the act of progression in the mammal. *Proceedings of the Royal Society of London. Series B, containing papers of a biological character*, 84(572):308–319, 1911.

Frank L Buczek and PETER R Cavanagh. Stance phase knee and ankle kinematics and kinetics during level and downhill running. *Med Sci Sports Exerc*, 22(5):669–677, 1990.

Etienne Burdet, Rieko Osu, David W Franklin, Theodore E Milner, and Mitsuo Kawato. The central nervous system stabilizes unstable dynamics by learning optimal impedance. *Nature*, 414(6862):446–449, 2001.

Jean-Marie Cabelguen, Céline Bourcier-Lucas, and Réjean Dubuc. Bimodal locomotion elicited by electrical stimulation of the mid-brain in the salamander *notophthalmus viridescens*. *The Journal of Neuroscience*, 23(6):2434–2439, 2003.

Roberto Calandra, Nakul Gopalan, André Seyfarth, Jan Peters, and Marc Peter Deisenroth. Bayesian gait optimization for bipedal locomotion. In *International Conference on Learning and Intelligent Optimization*, pages 274–290. Springer, 2014.

Charles Capaday. The special nature of human walking and its neural control. *Trends in neurosciences*, 25(7):370–376, 2002.

Joshua M Caputo and Steven H Collins. An experimental robotic testbed for accelerated development of ankle prostheses. In *Robotics and automation (ICRA), 2013 IEEE international conference on*, pages 2645–2650. IEEE, 2013.

Joshua M Caputo, Peter G Adamczyk, and Steven H Collins. Informing ankle-foot prosthesis prescription through haptic emulation of candidate devices. In *2015 IEEE International Conference on Robotics and Automation (ICRA)*, pages 6445–6450. IEEE, 2015.

Wei Chu and Zoubin Ghahramani. Preference learning with gaussian processes. In *Proceedings of the 22nd international conference on Machine learning*, pages 137–144. ACM, 2005.

- Avis H Cohen and P Wallén. The neuronal correlate of locomotion in fish. *Experimental brain research*, 41(1):11–18, 1980.
- Steve Collins, Andy Ruina, Russ Tedrake, and Martijn Wisse. Efficient bipedal robots based on passive-dynamic walkers. *Science*, 307(5712):1082–1085, 2005.
- A Forner Cordero, HJFM Koopman, and Frans CT van der Helm. Energy analysis of human stumbling: the limitations of recovery. *Gait & posture*, 21(3):243–254, 2005.
- DT Davy and ML Audu. A dynamic optimization technique for predicting muscle forces in the swing phase of gait. *Journal of biomechanics*, 20(2):187–201, 1987.
- Isabelle Delvolv  , Pascal Branchereau, R  jean Dubuc, and Jean-Marie Cabelguen. Fictive rhythmic motor patterns induced by nmda in an in vitro brain stem–spinal cord preparation from an adult urodele. *Journal of Neurophysiology*, 82(2):1074–1077, 1999.
- Ruta Desai and Hartmut Geyer. Robust swing leg placement under large disturbances. In *Robotics and Biomimetics (ROBIO), 2012 IEEE International Conference on*, pages 265–270. IEEE, 2012.
- Ruta Desai and Hartmut Geyer. Muscle-reflex control of robust swing leg placement. In *Robotics and Automation (ICRA), 2013 IEEE International Conference on*, pages 2169–2174. IEEE, 2013.
- Max Donath. *Proportional EMG control for above knee prostheses*. PhD thesis, Massachusetts Institute of Technology, 1974.
- Michael F Eilenberg, Hartmut Geyer, and Hugh Herr. Control of a powered ankle–foot prosthesis based on a neuromuscular model. *Neural Systems and Rehabilitation Engineering, IEEE Transactions on*, 18(2):164–173, 2010.
- Gen Endo, Jun Nakanishi, Jun Morimoto, and Gordon Cheng. Experimental studies of a neural oscillator for biped locomotion with qrio. In *Proceedings of the 2005 IEEE international conference on robotics and automation*, pages 596–602. IEEE, 2005.
- Janice J Eng, David A Winter, and Aftab E Patla. Strategies for recovery from a trip in early and late swing during human walking. *Experimental Brain Research*, 102(2):339–349, 1994.
- Johannes Englsberger, Twan Koolen, Sylvain Bertrand, Jerry Pratt, Christian Ott, and Alin Albu-Sch  ffer. Trajectory generation for continuous leg forces during double support and heel-to-toe shift based on divergent component of motion. In *2014 IEEE/RSJ*

International Conference on Intelligent Robots and Systems, pages 4022–4029. IEEE, 2014.

Siyuan Feng, Eric Whitman, X Xinjilefu, and Christopher G Atkeson. Optimization-based full body control for the darpa robotics challenge. *Journal of Field Robotics*, 32(2):293–312, 2015.

Woodie C Flowers. Use of an amputee-computer interactive facility in above-knee prosthesis research. In *Proceedings of the 1974 annual conference-Volume 1*, pages 335–339. ACM, 1974.

M Garrett and RG Luckwill. Role of reflex responses of knee musculature during the swing phase of walking in man. *European journal of applied physiology and occupational physiology*, 52(1):36–41, 1983.

Christiane Gauthier-Gagnon, Marie-Claude Grisé, and Diane Potvin. Enabling factors related to prosthetic use by people with transtibial and transfemoral amputation. *Archives of physical medicine and rehabilitation*, 80(6):706–713, 1999.

Yanli Geng, Peng Yang, Xiaoyun Xu, and Lingling Chen. Design and simulation of active transfemoral prosthesis. In *2012 24th Chinese Control and Decision Conference (CCDC)*, pages 3724–3728. IEEE, 2012.

Hartmut Geyer and Hugh Herr. A muscle-reflex model that encodes principles of legged mechanics produces human walking dynamics and muscle activities. *IEEE Transactions on neural systems and rehabilitation engineering*, 18(3):263–273, 2010.

Hartmut Geyer, Andre Seyfarth, and Reinhard Blickhan. Compliant leg behaviour explains basic dynamics of walking and running. *Proceedings of the Royal Society of London B: Biological Sciences*, 273(1603):2861–2867, 2006.

Daoxiong Gong, Jie Yan, and Guoyu Zuo. A review of gait optimization based on evolutionary computation. *Applied Computational Intelligence and Soft Computing*, 2010, 2010.

Claire C Gordon, RA Walker, I Tebbetts, JT McConville, B Bradtmiller, CE Clauser, and T Churchill. *1988 Anthropometric Survey of US Army Personnel-Methods and Summary Statistics. Final Report*. 1989.

Mark D Grabiner, Timothy J Koh, Thomas M Lundin, and Dennis W Jahnigen. Kinematics of recovery from a stumble. *Journal of gerontology*, 48(3):M97–M102, 1993.

Robert D Gregg, Tommaso Lenzi, Levi J Hargrove, and Jonathon W Sensinger. Virtual constraint control of a powered prosthetic leg:

- From simulation to experiments with transfemoral amputees. *IEEE Transactions on Robotics*, 30(6):1455–1471, 2014.
- Michael J Grey, Jens Bo Nielsen, Nazarena Mazzaro, and Thomas Sinkjær. Positive force feedback in human walking. *The Journal of physiology*, 581(1):99–105, 2007.
- DL Grimes, WC Flowers, and M Donath. Feasibility of an active control scheme for above knee prostheses. *Journal of Biomechanical Engineering*, 99(4):215–221, 1977.
- Donald Lee Grimes. *An active multi-mode above knee prosthesis controller*. PhD thesis, Massachusetts Institute of Technology, 1979.
- Jesse A Grimes. *ATRIAS 1.0 & 2.1: enabling agile biped locomotion with a template-driven approach to robot design*. PhD thesis, Oregon State University, 2013.
- Michael Günther and Hanns Ruder. Synthesis of two-dimensional human walking: a test of the λ -model. *Biological cybernetics*, 89(2):89–106, 2003.
- Xin Guo, Lingling Chen, Yang Zhang, Peng Yang, and Liqun Zhang. A study on control mechanism of above knee robotic prosthesis based on cpg model. In *Robotics and Biomimetics (ROBIO), 2010 IEEE International Conference on*, pages 283–287. IEEE, 2010.
- Kevin H Ha, Huseyin Atakan Varol, and Michael Goldfarb. Volitional control of a prosthetic knee using surface electromyography. *IEEE Transactions on Biomedical Engineering*, 58(1):144–151, 2011.
- Nikolaus Hansen. The cma evolution strategy: a comparing review. In *Towards a new evolutionary computation*, pages 75–102. Springer, 2006.
- Levi J Hargrove, Aaron J Young, Ann M Simon, Nicholas P Fey, Robert D Lipschutz, Suzanne B Finucane, Elizabeth G Halsne, Kimberly A Ingraham, and Todd A Kuiken. Intuitive control of a powered prosthetic leg during ambulation: a randomized clinical trial. *JAMA*, 313(22):2244–2252, 2015.
- Philipp Hennig and Christian J Schuler. Entropy search for information-efficient global optimization. *The Journal of Machine Learning Research*, 13(1):1809–1837, 2012.
- José Miguel Hernández-Lobato, Matthew W Hoffman, and Zoubin Ghahramani. Predictive entropy search for efficient global optimization of black-box functions. In *Advances in Neural Information Processing Systems*, pages 918–926, 2014.

Hugh M. Herr and Alena M. Grabowski. Bionic ankle-foot prosthesis normalizes walking gait for persons with leg amputation. *Proceedings of the Royal Society of London B: Biological Sciences*, 279(1728):457–464, 2011. ISSN 0962-8452. DOI: 10.1098/rspb.2011.1194. URL <http://rspb.royalsocietypublishing.org/content/279/1728/457>.

Alexander Herzog, Ludovic Righetti, Felix Grimminger, Peter Pastor, and Stefan Schaal. Balancing experiments on a torque-controlled humanoid with hierarchical inverse dynamics. In *2014 IEEE/RSJ International Conference on Intelligent Robots and Systems*, pages 981–988. IEEE, 2014.

Kazuo Hirai, Masato Hirose, Yuji Haikawa, and Toru Takenaka. The development of honda humanoid robot. In *Robotics and Automation, 1998. Proceedings. 1998 IEEE International Conference on*, volume 2, pages 1321–1326. IEEE, 1998.

Joseph K Hitt, Ryan Bellman, Matthew Holgate, Thomas G Sugar, and Kevin W Hollander. The sparky (spring ankle with regenerative kinetics) project: Design and analysis of a robotic transtibial prosthesis with regenerative kinetics. In *ASME 2007 International Design Engineering Technical Conferences and Computers and Information in Engineering Conference*, pages 1587–1596. American Society of Mechanical Engineers, 2007.

Cheriel J Hofstad, Vivian Weerdesteyn, Harmen van der Linde, Bart Nienhuis, Alexander C Geurts, and Jacques Duysens. Evidence for bilaterally delayed and decreased obstacle avoidance responses while walking with a lower limb prosthesis. *Clinical Neurophysiology*, 120(5):1009–1015, 2009.

Neville Hogan. Impedance control: An approach to manipulation: Part ii—implementation. *Journal of dynamic systems, measurement, and control*, 107(1):8–16, 1985.

Matthew A Holgate, Joseph K Hitt, Ryan D Bellman, Thomas G Sugar, and Kevin W Hollander. The sparky (spring ankle with regenerative kinetics) project: Choosing a dc motor based actuation method. In *2008 2nd IEEE RAS & EMBS International Conference on Biomedical Robotics and Biomechatronics*, pages 163–168. IEEE, 2008.

Neil Houlsby, Ferenc Huszar, Zoubin Ghahramani, and Jose M Hernández-lobato. Collaborative gaussian processes for preference learning. In *Advances in Neural Information Processing Systems*, pages 2096–2104, 2012.

- He Huang, Todd A Kuiken, Robert D Lipschutz, et al. A strategy for identifying locomotion modes using surface electromyography. *IEEE Transactions on Biomedical Engineering*, 56(1):65–73, 2009.
- He Huang, Fan Zhang, Levi J Hargrove, Zhi Dou, Daniel R Rogers, and Kevin B Englehart. Continuous locomotion-mode identification for prosthetic legs based on neuromuscular-mechanical fusion. *IEEE Transactions on Biomedical Engineering*, 58(10):2867–2875, 2011.
- CL Hubley and RP Wells. A work-energy approach to determine individual joint contributions to vertical jump performance. *European Journal of Applied Physiology and Occupational Physiology*, 50(2):247–254, 1983.
- Amanda M Huff, Brian E Lawson, and Michael Goldfarb. A running controller for a powered transfemoral prosthesis. In *2012 Annual International Conference of the IEEE Engineering in Medicine and Biology Society*, pages 4168–4171. IEEE, 2012.
- Marco Hutter, Mark A Hoepflinger, Christian Gehring, Michael Bloesch, C David Remy, and Roland Siegwart. Hybrid operational space control for compliant legged systems. *Robotics: Science and systems VIII*, page 129, 2013.
- Auke Jan Ijspeert. Central pattern generators for locomotion control in animals and robots: a review. *Neural Networks*, 21(4):642–653, 2008.
- Sonja MHJ Jaegers, J Hans Arendzen, and Henry J de Jongh. Prosthetic gait of unilateral transfemoral amputees: a kinematic study. *Archives of physical medicine and rehabilitation*, 76(8):736–743, 1995.
- Ashesh Jain, Brian Wojcik, Thorsten Joachims, and Ashutosh Saxena. Learning trajectory preferences for manipulators via iterative improvement. In *Advances in neural information processing systems*, pages 575–583, 2013.
- Jennifer L Johansson, Delsey M Sherrill, Patrick O Riley, Paolo Bonato, and Hugh Herr. A clinical comparison of variable-damping and mechanically passive prosthetic knee devices. *American journal of physical medicine & rehabilitation*, 84(8):563–575, 2005.
- Donald R Jones, Matthias Schonlau, and William J Welch. Efficient global optimization of expensive black-box functions. *Journal of Global optimization*, 13(4):455–492, 1998.
- Shuuji Kajita and Kazuo Tani. Study of dynamic biped locomotion on rugged terrain-derivation and application of the linear inverted pendulum mode. In *Robotics and Automation, 1991. Proceedings., 1991 IEEE International Conference on*, pages 1405–1411. IEEE, 1991.

Shuuji Kajita, Fumio Kanehiro, Kenji Kaneko, Kazuhito Yokoi, and Hirohisa Hirukawa. The 3d linear inverted pendulum mode: A simple modeling for a biped walking pattern generation. In *Intelligent Robots and Systems, 2001. Proceedings. 2001 IEEE/RSJ International Conference on*, volume 1, pages 239–246. IEEE, 2001.

Shuuji Kajita, Fumio Kanehiro, Kenji Kaneko, Kiyoshi Fujiwara, Kensuke Harada, Kazuhito Yokoi, and Hirohisa Hirukawa. Biped walking pattern generation by using preview control of zero-moment point. In *Robotics and Automation, 2003. Proceedings. ICRA'03. IEEE International Conference on*, volume 2, pages 1620–1626. IEEE, 2003.

Shuuji Kajita, Takashi Nagasaki, Kenji Kaneko, and Hirohisa Hirukawa. Zmp-based biped running control. *IEEE robotics & automation magazine*, 2(14):63–72, 2007.

Robert E Kearney and Ian W Hunter. System identification of human joint dynamics. *Critical reviews in biomedical engineering*, 18(1):55–87, 1989.

W Bradley Knox and Peter Stone. Interactively shaping agents via human reinforcement: The tamer framework. In *Proceedings of the fifth international conference on Knowledge capture*, pages 9–16. ACM, 2009.

W Bradley Knox, Peter Stone, and Cynthia Breazeal. Training a robot via human feedback: A case study. In *Social Robotics*, pages 460–470. Springer, 2013.

Scott Kuindersma, Frank Permenter, and Russ Tedrake. An efficiently solvable quadratic program for stabilizing dynamic locomotion. In *2014 IEEE International Conference on Robotics and Automation (ICRA)*, pages 2589–2594. IEEE, 2014.

Brian E Lawson, H Atakan Varol, Frank Sup, and Michael Goldfarb. Stumble detection and classification for an intelligent transfemoral prosthesis. In *2010 Annual International Conference of the IEEE Engineering in Medicine and Biology*, pages 511–514. IEEE, 2010.

Brian E Lawson, Jason Mitchell, Don Truex, Amanda Shultz, Elissa Ledoux, and Michael Goldfarb. A robotic leg prosthesis: Design, control, and implementation. *IEEE Robotics & Automation Magazine*, 21(4):70–81, 2014.

Brian Edward Lawson, Huseyin Atakan Varol, Amanda Huff, Erdem Erdemir, and Michael Goldfarb. Control of stair ascent and descent with a powered transfemoral prosthesis. *IEEE Transactions on Neural Systems and Rehabilitation Engineering*, 21(3):466–473, 2013.

T Lenzi, LJ Hargrove, and JW Sensinger. Minimum jerk swing control allows variable cadence in powered transfemoral prostheses. In *Conference Proceedings IEEE Engineering in Medicine and Biology Society*, pages 2492–2495, 2014a.

Tommaso Lenzi, Levi Hargrove, and Jonathon Sensinger. Speed-adaptation mechanism: Robotic prostheses can actively regulate joint torque. *IEEE Robotics & Automation Magazine*, 21(4):94–107, 2014b.

David R Lide. *CRC handbook of chemistry and physics*, volume 85. CRC press, 2004.

Yiping Liu, Patrick M Wensing, James P Schmiedeler, and David E Orin. Terrain-blind humanoid walking based on a 3-d actuated dual-slip model. *IEEE Robotics and Automation Letters*, 1(2):1073–1080, 2016.

Marilyn MacKay-Lyons. Central pattern generation of locomotion: a review of the evidence. *Physical therapy*, 82(1):69–83, 2002.

Jared Markowitz, Pavitra Krishnaswamy, Michael F Eilenberg, Ken Endo, Chris Barnhart, and Hugh Herr. Speed adaptation in a powered transtibial prosthesis controlled with a neuromuscular model. *Philosophical Transactions of the Royal Society of London B: Biological Sciences*, 366(1570):1621–1631, 2011.

William C Martin, Albert Wu, and Hartmut Geyer. Robust spring mass model running for a physical bipedal robot. In *2015 IEEE International Conference on Robotics and Automation (ICRA)*, pages 6307–6312. IEEE, 2015.

Ernesto C Martinez-Villalpando, Jeff Weber, Grant Elliott, and Hugh Herr. Design of an agonist-antagonist active knee prosthesis. In *2008 2nd IEEE RAS & EMBS International Conference on Biomedical Robotics and Biomechatronics*, pages 529–534. IEEE, 2008.

Ernesto C Martinez-Villalpando, Luke Mooney, Grant Elliott, and Hugh Herr. Antagonistic active knee prosthesis. a metabolic cost of walking comparison with a variable-damping prosthetic knee. In *2011 Annual International Conference of the IEEE Engineering in Medicine and Biology Society*, pages 8519–8522. IEEE, 2011.

Kiyotoshi Matsuoka. Mechanisms of frequency and pattern control in the neural rhythm generators. *Biological cybernetics*, 56(5-6):345–353, 1987.

ANDREW D McClellan and WOCHAN Jang. Mechanosensory inputs to the central pattern generators for locomotion in the lamprey

- spinal cord: resetting, entrainment, and computer modeling. *Journal of Neurophysiology*, 70(6):2442–2454, 1993.
- Tad McGeer. Passive dynamic walking. *The international journal of robotics research*, 9(2):62–82, 1990.
- Michael D McKay, Richard J Beckman, and William J Conover. A comparison of three methods for selecting values of input variables in the analysis of output from a computer code. *Technometrics*, 42(1):55–61, 2000.
- R McNeill Alexander. Energetics and optimization of human walking and running: the 2000 raymond pearl memorial lecture. *American journal of human biology*, 14(5):641–648, 2002.
- William C Miller, Mark Speechley, and Barry Deathe. The prevalence and risk factors of falling and fear of falling among lower extremity amputees. *Archives of physical medicine and rehabilitation*, 82(8):1031–1037, 2001.
- Simon Mochon and Thomas A McMahon. Ballistic walking. *Journal of biomechanics*, 13(1):49–57, 1980.
- Gaspar Mora, Rafael R Torrealba, José Cappelletto, Leonardo Fermín, G Fernández-López, and Juan C Grieco. Cybernetic knee prosthesis: application of an adaptive central pattern generator. *Kybernetes*, 41(1/2):192–205, 2012.
- Maxon Motor. Mason ec-4pole, Apr 2016a. URL http://www.maxonmotorusa.com/medias/sys_master/root/8821066268702/16-274-en.pdf.
- Maxon Motor. Maxon flat motor, Apr 2016b. URL http://www.maxonmotorusa.com/medias/sys_master/root/8821068005406/16-304-en.pdf.
- Akihiko Murai and Katsu Yamane. A neuromuscular locomotion controller that realizes human-like responses to unexpected disturbances. In *Robotics and Automation (ICRA), 2011 IEEE International Conference on*, pages 1997–2002. IEEE, 2011.
- Sylvie Nadeau, Bradford J McFadyen, and Francine Malouin. Frontal and sagittal plane analyses of the stair climbing task in healthy adults aged over 40 years: what are the challenges compared to level walking? *Clinical Biomechanics*, 18(10):950–959, 2003.
- Gora Chand Nandi, Auke Jan Ijspeert, Pavan Chakraborty, and Anirban Nandi. Development of adaptive modular active leg (amal) using bipedal robotics technology. *Robotics and Autonomous Systems*, 57(6):603–616, 2009.

- Andrew Y Ng, Stuart J Russell, et al. Algorithms for inverse reinforcement learning. In *ICML*, pages 663–670, 2000.
- Jens Bo Nielsen. How we walk: central control of muscle activity during human walking. *The Neuroscientist*, 9(3):195–204, 2003.
- Tom F Novacheck. The biomechanics of running. *Gait & posture*, 7(1):77–95, 1998.
- Naomichi Oghara and Nobutoshi Yamazaki. Generation of human bipedal locomotion by a bio-mimetic neuro-musculo-skeletal model. *Biological cybernetics*, 84(1):1–11, 2001.
- Jacquelin Perry and Judith M Burnfield. *Gait analysis: normal and pathological function*. Slack Thorofare, NJ, 2 edition, 2010.
- Michael Raymond Pierrynowski and James Barbour Morrison. A physiological model for the evaluation of muscular forces in human locomotion: theoretical aspects. *Mathematical Biosciences*, 75(1):69–101, 1985.
- Mirjam Pijnappels, Maarten F Bobbert, and Jaap H van Dieën. Contribution of the support limb in control of angular momentum after tripping. *Journal of biomechanics*, 37(12):1811–1818, 2004.
- Mirjam Pijnappels, Maarten F Bobbert, and Jaap H van Dieën. How early reactions in the support limb contribute to balance recovery after tripping. *Journal of biomechanics*, 38(3):627–634, 2005.
- Patrick M Pilarski, Michael R Dawson, Thomas Degris, Farbod Fahimi, Jason P Carey, and Richard S Sutton. Online human training of a myoelectric prosthesis controller via actor-critic reinforcement learning. In *2011 IEEE International Conference on Rehabilitation Robotics*, pages 1–7. IEEE, 2011.
- Dean A Pomerleau. Efficient training of artificial neural networks for autonomous navigation. *Neural Computation*, 3(1):88–97, 1991.
- Gill A Pratt and Matthew M Williamson. Series elastic actuators. In *Intelligent Robots and Systems 95.'Human Robot Interaction and Cooperative Robots', Proceedings. 1995 IEEE/RSJ International Conference on*, volume 1, pages 399–406. IEEE, 1995.
- Jerry Pratt and Ben Krupp. Design of a bipedal walking robot. In *SPIE defense and security symposium*, pages 69621F–69621F. International Society for Optics and Photonics, 2008.
- Jerry Pratt, Chee-Meng Chew, Ann Torres, Peter Dilworth, and Gill Pratt. Virtual model control: An intuitive approach for bipedal

- locomotion. *The International Journal of Robotics Research*, 20(2):129–143, 2001.
- Jerry Pratt, John Carff, Sergey Drakunov, and Ambarish Goswami. Capture point: A step toward humanoid push recovery. In *2006 6th IEEE-RAS international conference on humanoid robots*, pages 200–207. IEEE, 2006.
- Marc H Raibert. *Legged robots that balance*. MIT press, 1986.
- Marc Harold Raibert, H Benjamin Brown, Michael Chepponis, and Eugene Hastings. Dynamically stable legged locomotion: second report to darpa, october 1, 1981-december 31, 1982. Technical report, Carnegie Mellon University, 1983.
- Jack Alan Rall. Energetic aspects of skeletal muscle contraction: implications of fiber types. *Exercise and sport sciences reviews*, 13:33–74, 1984.
- Nathan D Ratliff, J Andrew Bagnell, and Martin A Zinkevich. Maximum margin planning. In *Proceedings of the 23rd international conference on Machine learning*, pages 729–736. ACM, 2006.
- Ludovic Righetti and Auke Jan Ijspeert. Programmable central pattern generators: an application to biped locomotion control. In *Proceedings 2006 IEEE International Conference on Robotics and Automation, 2006. ICRA 2006.*, pages 1585–1590. IEEE, 2006.
- Ludovic Righetti, Jonas Buchli, and Auke Jan Ijspeert. Dynamic hebbian learning in adaptive frequency oscillators. *Physica D: Nonlinear Phenomena*, 216(2):269–281, 2006.
- Stephen N Robinovitch, Fabio Feldman, Yijian Yang, Rebecca Schonnop, Pet Ming Leung, Thiago Sarraf, Joanie Sims-Gould, and Marie Loughin. Video capture of the circumstances of falls in elderly people residing in long-term care: an observational study. *The Lancet*, 381(9860):47–54, 2013.
- David William Robinson. *Design and analysis of series elasticity in closed-loop actuator force control*. PhD thesis, Massachusetts Institute of Technology, 2000.
- Stéphane Ross, Geoffrey J Gordon, and Drew Bagnell. A reduction of imitation learning and structured prediction to no-regret online learning. In *AISTATS*, page 6, 2011.
- Serge Rossignol. Locomotion and its recovery after spinal injury. *Current opinion in neurobiology*, 10(6):708–716, 2000.

- Elliott J Rouse, Robert D Gregg, Levi J Hargrove, and Jonathon W Sensinger. The difference between stiffness and quasi-stiffness in the context of biomechanical modeling. *IEEE Transactions on Biomedical Engineering*, 60(2):562–568, 2013.
- Elliott J Rouse, Luke M Mooney, and Hugh M Herr. Clutchable series-elastic actuator: Implications for prosthetic knee design. *The International Journal of Robotics Research*, page 0278364914545673, 2014.
- Elliott J Rouse, Nathan C Villagaray-Carski, Robert W Emerson, and Hugh M Herr. Design and testing of a bionic dancing prosthesis. *PloS one*, 10(8):e0135148, 2015.
- Layale Saab, Oscar E Ramos, François Keith, Nicolas Mansard, Philippe Soueres, and Jean-Yves Fourquet. Dynamic whole-body motion generation under rigid contacts and other unilateral constraints. *IEEE Transactions on Robotics*, 29(2):346–362, 2013.
- Gregory S Sawicki, Cara L Lewis, and Daniel P Ferris. It pays to have a spring in your step. *Exercise and sport sciences reviews*, 37(3):130, 2009.
- Stefan Schaal. Is imitation learning the route to humanoid robots? *Trends in cognitive sciences*, 3(6):233–242, 1999.
- Alexander Schepelmann. *Evaluation of Decentralized Reactive Swing-Leg Controllers on Powered Robotic Legs*. PhD thesis, Carnegie Mellon University, 2016.
- Alexander Schepelmann, Michael D Taylor, and Hartmut Geyer. Development of a testbed for robotic neuromuscular controllers. *Robotics: Science and Systems VIII*, 2012.
- AM Schillings, BMH Van Wezel, TH Mulder, and Jaak Duysens. Muscular responses and movement strategies during stumbling over obstacles. *Journal of Neurophysiology*, 83(4):2093–2102, 2000.
- Stephen H Scott and David A Winter. Biomechanical model of the human foot: kinematics and kinetics during the stance phase of walking. *Journal of biomechanics*, 26(9):1091–1104, 1993.
- Andre Seyfarth, Hartmut Geyer, Michael Günther, and Reinhard Blickhan. A movement criterion for running. *Journal of biomechanics*, 35(5):649–655, 2002.
- Jiang Shan and Fumio Nagashima. Neural locomotion controller design and implementation for humanoid robot hoap-1. In *20th annual conference of the robotics society of Japan*, 2002.

Charles Sherrington. *The integrative action of the nervous system*. CUP Archive, 1910a.

Charles Scott Sherrington. Flexion-reflex of the limb, crossed extension-reflex, and reflex stepping and standing. *The Journal of physiology*, 40(1-2):28–121, 1910b.

ML Shik, FV Severin, and ORLOVSKI. GN. Control of walking and running by means of electrical stimulation of mid-brain. *BIOPHYSICS-USSR*, 11(4):756, 1966.

Shuhei Shimmyo, Tomoya Sato, and Kouhei Ohnishi. Biped walking pattern generation by using preview control with virtual plane method. In *2010 11th IEEE International Workshop on Advanced Motion Control (AMC)*, pages 414–419. IEEE, 2010.

Camila Shiota, Ann M Simon, and Todd A Kuiken. Recovery strategy identification throughout swing phase using kinematic data from the tripped leg. In *2014 36th Annual International Conference of the IEEE Engineering in Medicine and Biology Society*, pages 6199–6202. IEEE, 2014.

Camila Shiota, Ann M Simon, and Todd A Kuiken. Transfemoral amputee recovery strategies following trips to their sound and prosthesis sides throughout swing phase. *Journal of neuroengineering and rehabilitation*, 12(1):1, 2015.

Amanda H Shultz, Jason E Mitchell, Don Truex, Brian E Lawson, Elissa Ledoux, and Michael Goldfarb. A walking controller for a powered ankle prosthesis. In *2014 36th Annual International Conference of the IEEE Engineering in Medicine and Biology Society*, pages 6203–6206. IEEE, 2014.

Amanda H Shultz, Brian E Lawson, and Michael Goldfarb. Running with a powered knee and ankle prosthesis. *IEEE Transactions on Neural Systems and Rehabilitation Engineering*, 23(3):403–412, 2015.

SR Soffe and Alan Roberts. Tonic and phasic synaptic input to spinal cord motoneurons during fictive locomotion in frog embryos. *Journal of Neurophysiology*, 48(6):1279–1288, 1982.

E Solak, R Murray Smith, WE Leithead, D Leith, and CE Rasmussen. Derivative observations in gaussian process models of dynamic systems. *Advances in Neural Information Processing Systems*, pages 1057–1064, 2003.

Seungmoon Song and Hartmut Geyer. Generalization of a muscle-reflex control model to 3d walking. In *2013 35th Annual International*

- Conference of the IEEE Engineering in Medicine and Biology Society (EMBC)*, pages 7463–7466. IEEE, 2013.
- Seungmoon Song and Hartmut Geyer. A neural circuitry that emphasizes spinal feedback generates diverse behaviours of human locomotion. *The Journal of physiology*, 593(16):3493–3511, 2015.
- Seungmoon Song, Ruta Desai, and Hartmut Geyer. Integration of an adaptive swing control into a neuromuscular human walking model. In *2013 35th Annual International Conference of the IEEE Engineering in Medicine and Biology Society (EMBC)*, pages 4915–4918. IEEE, 2013.
- Koushil Sreenath, Hae-Won Park, Ioannis Poulakakis, and Jessy W Grizzle. A compliant hybrid zero dynamics controller for stable, efficient and fast bipedal walking on mabel. *The International Journal of Robotics Research*, 30(9):1170–1193, 2011.
- JE Stewart, H Barbeau, and S Gauthier. Modulation of locomotor patterns and spasticity with clonidine in spinal cord injured patients. *Canadian Journal of Neurological Sciences/Journal Canadien des Sciences Neurologiques*, 18(03):321–332, 1991.
- Frank Sup, Amit Bohara, and Michael Goldfarb. Design and control of a powered knee and ankle prosthesis. In *Proceedings 2007 IEEE International Conference on Robotics and Automation*, pages 4134–4139. IEEE, 2007.
- Frank Sup, Amit Bohara, and Michael Goldfarb. Design and control of a powered transfemoral prosthesis. *The International journal of robotics research*, 27(2):263–273, 2008.
- Frank Sup, Huseyin Atakan Varol, Jason Mitchell, Thomas J Withrow, and Michael Goldfarb. Preliminary evaluations of a self-contained anthropomorphic transfemoral prosthesis. *IEEE/ASME Transactions on mechatronics*, 14(6):667–676, 2009.
- Frank Sup, Huseyin Atakan Varol, and Michael Goldfarb. Upslope walking with a powered knee and ankle prosthesis: initial results with an amputee subject. *IEEE Transactions on Neural Systems and Rehabilitation Engineering*, 19(1):71–78, 2011.
- Gentaro Taga, Yoko Yamaguchi, and Hiroshi Shimizu. Self-organized control of bipedal locomotion by neural oscillators in unpredictable environment. *Biological cybernetics*, 65(3):147–159, 1991.
- Matthew Tesch, Jeff Schneider, and Howie Choset. Using response surfaces and expected improvement to optimize snake robot gait

parameters. In *2011 IEEE/RSJ International Conference on Intelligent Robots and Systems*, pages 1069–1074. IEEE, 2011.

Nitish Thatte and Hartmut Geyer. Toward balance recovery with leg prostheses using neuromuscular model control. *IEEE Transactions on Biomedical Engineering*, 63(5):904–913, 2016.

Rafael R Torrealba, Claudia Pérez-D'Arpino, José Cappelletto, Leonardo Fermin-Leon, Gerardo Fernández-López, and Juan C Grieco. Through the development of a biomechatronic knee prosthesis for transfemoral amputees: mechanical design and manufacture, human gait characterization, intelligent control strategies and tests. In *Robotics and Automation (ICRA), 2010 IEEE International Conference on*, pages 2934–2939. IEEE, 2010.

Miles A Townsend. Biped gait stabilization via foot placement. *Journal of biomechanics*, 18(1):21–38, 1985.

Brian R Umberger, Karin GM Gerritsen, and Philip E Martin. A model of human muscle energy expenditure. *Computer methods in biomechanics and biomedical engineering*, 6(2):99–111, 2003.

Huseyin Atakan Varol, Frank Sup, and Michael Goldfarb. Powered sit-to-stand and assistive stand-to-sit framework for a powered transfemoral prosthesis. In *2009 IEEE International Conference on Rehabilitation Robotics*, pages 645–651. IEEE, 2009.

Huseyin Atakan Varol, Frank Sup, and Michael Goldfarb. Multiclass real-time intent recognition of a powered lower limb prosthesis. *IEEE Transactions on Biomedical Engineering*, 57(3):542–551, 2010.

Christopher L Vaughan. Theories of bipedal walking: an odyssey. *Journal of biomechanics*, 36(4):513–523, 2003.

Jing Wang, Oliver A Kannape, and Hugh M Herr. Proportional emg control of ankle plantar flexion in a powered transtibial prosthesis. In *Rehabilitation Robotics (ICORR), 2013 IEEE International Conference on*, pages 1–5. IEEE, 2013.

RL Waters, Jacqueline Perry, DANIEL Antonelli, and Helen Hislop. Energy cost of walking of amputees: the influence of level of amputation. *J Bone Joint Surg Am*, 58(1):42–46, 1976.

Patrick M Wensing and David E Orin. Generation of dynamic humanoid behaviors through task-space control with conic optimization. In *Robotics and Automation (ICRA), 2013 IEEE International Conference on*, pages 3103–3109. IEEE, 2013.

- Michael James Whitley. *Maximum Absolute and Relative Joint Torques during Recovery from a Simulated Trip*. PhD thesis, Virginia Polytechnic Institute and State University, 2008.
- Christopher KI Williams and Carl Edward Rasmussen. *Gaussian processes for machine learning*, volume 2. 2006.
- Aaron Wilson, Alan Fern, and Prasad Tadepalli. A bayesian approach for policy learning from trajectory preference queries. In *Advances in neural information processing systems*, pages 1133–1141, 2012.
- David A Winter. *Biomechanics and motor control of human movement*. John Wiley & Sons, 2009.
- Justin Won and Neville Hogan. Stability properties of human reaching movements. *Experimental Brain Research*, 107(1):125–136, 1995.
- Albert Wu and Hartmut Geyer. The 3-d spring–mass model reveals a time-based deadbeat control for highly robust running and steering in uncertain environments. *IEEE Transactions on Robotics*, 29(5):1114–1124, 2013.
- Sai-Kit Wu, Garrett Waycaster, and Xiangrong Shen. Electromyography-based control of active above-knee prostheses. *Control Engineering Practice*, 19(8):875–882, 2011.
- Linfeng Xu and X Rong Li. Estimation and filtering of gaussian variables with linear inequality constraints. In *Information Fusion (FUSION), 2010 13th Conference on*, pages 1–6. IEEE, 2010.
- JAYNIE F Yang and RICHARD B Stein. Phase-dependent reflex reversal in human leg muscles during walking. *Journal of Neurophysiology*, 63(5):1109–1117, 1990.
- JF Yang, RB Stein, and KB James. Contribution of peripheral afferents to the activation of the soleus muscle during walking in humans. *Experimental Brain Research*, 87(3):679–687, 1991.
- KangKang Yin, Kevin Loken, and Michiel van de Panne. Simbicon: Simple biped locomotion control. In *ACM Transactions on Graphics (TOG)*, volume 26, page 105. ACM, 2007.
- Fan Zhang, Susan E D’Andrea, Michael J Nunnery, Steven M Kay, and He Huang. Towards design of a stumble detection system for artificial legs. *IEEE Transactions on Neural Systems and Rehabilitation Engineering*, 19(5):567–577, 2011.
- Huihua Zhao, Jonathan Horn, Jacob Reher, Victor Paredes, and Aaron D Ames. First steps toward translating robotic walking

to prostheses: a nonlinear optimization based control approach.
Autonomous Robots, pages 1–18, 2016.

Brian D Ziebart, Andrew L Maas, J Andrew Bagnell, and Anind K Dey. Human behavior modeling with maximum entropy inverse optimal control. In *AAAI Spring Symposium: Human Behavior Modeling*, page 92, 2009.

Kathryn Ziegler-Graham, Ellen J MacKenzie, Patti L Ephraim, Thomas G Travison, and Ron Brookmeyer. Estimating the prevalence of limb loss in the united states: 2005 to 2050. *Archives of physical medicine and rehabilitation*, 89(3):422–429, 2008.